ION SPUTTERING -INDUCED FORMATION OF SEMICONDUCTING AND METALLIC NANOSTRUCTURES

by

Jia-Hung Wu

A dissertation submitted in partial fulfillment
of the requirements for the degree of
Doctor of Philosophy
(Materials Science and Engineering)
in the University of Michigan
2013

Doctoral Committee:

Professor Rachel S. Goldman, Chair
Professor Roy Clarke
Associate Professor Kevin P. Pipe
Associate Professor Katsuyo S. Thornton

© Jia-Hung Wu 2013
All Rights Reserved

ACKNOWLEDGEMENTS

I would like to thank my advisor, Prof. Rachel S. Goldman for her guidance and support throughout my studies at the University of Michigan. I would also like to thank Prof. Katsuyo Thornton, Kevin Pipe, and Roy Clarke, for their valuable discussions and suggestions.

This dissertation would not have been possible without the help of my many collaborators: Dr. Matthew Reason in Materials Science & Engineering; Mr. Jacob R. Jokisaari in Materials Science & Engineering; and Ms. Jieun Lee in Physics.

I thank all my fellow students in Professor Goldman's research group for their help. In particular, I would like to thank Dr. Yu Jin, Weifeng Ye, Leon Webster, Simon Huang for working on the MBE system with me; Yuming Jiang, Emily Robb, Ali Al-Heji and Myungkoo for their help with various sample characterizations; Dr. Rachel Collino and Dr. Vaishno Dasika for their support and encouragement.

Finally, my greatest gratitude to my parents, my wife, Jo-Yu and my daughter, Flora.

TABLE OF CONTENTS

ACKNOWLEDGEMENTS……………………………………………………………ii

LIST OF FIGURES……………………………………………………………..v

LIST OF TABLES…………………………………………………..………xii

LIST OF APPENDICES…………………………………………………………xiii

ABSTRACT……………………………………………………………………xiv

CHAPTER

1. INTRODUCTION……………………………………………………………1
1.1 Overview…………..……………………………………..1
1.2 Ion-Solid Interactions..……………………………………...3
1.3 Nanodot Formation………………..…………...…………...6
1.4 Ripple formation……..……………………………………..8
1.5 Nanorod Formation…………...……………...……..……...9
1.6 Dissertation Objectives………………………………………10
1.7 Outline of the Dissertation…………………………..…….12
1.8 Figures and References….…………………………………...15

2. EXPERIMENTAL PROCEDURES……………………………………..31
2.1 Overview…………………………………………………..31
2.2 Focused Ion Beam……...……………………………………33
2.3 Scanning Electron Microscopy ……………………………35
2.4 Molecular Beam Epitaxy …..…………………………….36
2.5 Atomic Force Microscopy…………..………………………37
2.6 Transmission Electron Microscopy……………..…………...38
2.7 X-Ray Energy Dispersive Spectroscopy………..…………...39
2.8 Photoluminescence Spectroscopy……………….…………...40
2.9 STM-based I-V Measurements in TEM…….………………...40
2.10 Figures and References……………………..………………42

3. Formation, Coarsening, and Motion of Ga Droplets ……………………...49
3.1 Overview…………………………………………….………49
3.2 Background………………………………………………….50
3.3 Experimental Details……………..……………………….....51

3.4 Droplet Formation and Growth……......……………….…..……53
3.5 Droplet Motion…………………………………….............56
3.6 Crystalliniry and Composition of Droplets.....………………60
3.7 Summary and Conclusion.............…...……………………..61
3.8 References and Figures ……………………………………62

4. Formation and Evolution of Focused-Ion-Beam-Induced Ripples…..……75
4.1 Overview……………………………………………………75
4.2 Background…………………………………………………76
4.3 Experimental Details………………………………………78
4.4 Ripple formation: Ion fluence dependence..…………………...79
4.5 Ripple formation: θ_{eff} dependence.......………….……………...80
4.6 Beyond ripples: Ion fluence dependence……………………82
4.7 Summary and conclusions………………………………...83
4.8 Figures and References…………………………………..85

5. Formation Mechanism of Focused-Ion-Beam-Induced Nanorods..………98
5.1 Overview……………………………………………………98
5.2 Background…………………………………………………99
5.3 Experimental Details………………………………………101
5.4 Influence of ion fluence on NR formation……….………....102
5.5 Influence of ion energy on NR formation………..…………102
5.6 Influence of InSb source on NR formation…………………103
5.7 Mechanisms for NR growth………………..………………104
5.8 Summary and conclusions………………………………..…106
5.9 Figures and References……………………………………..107

6. SUMMARY AND SUGGESTIONS FOR FUTURE WORK……………116
6.1 Summary……………………….....………………………116
6.2 Suggestions for Future Work………………………………118
6.3 References and Figures……………………………………..124

APPENDICES……………………………………………………………………131

LIST OF FIGURES

Figure 1.1 Target production-level patterning resolution, for DRAM and Flash, as a function of year. Adopted from the International Technology Roadmap..15

Figure 1.2 The nuclear (dotted line), electronic (dashed line) and total (solid line) stopping power as a function of kinetic energy for Ga+ ion irradiation of (a) GaAs and (b) InSb target. The data are calculated using the SRIM 2010 Monte Carlo simulation code. For these simulations, it was assumed that the sublimation energy is equivalent to the surface binding energy. The input parameters for GaAs include and atomic density of 5.32 g/cm³ for GaAs, threshold displacement energies of 12.4 eV for Ga and 20.8 eV for As, and surface binding energies of 2.82 eV for Ga and 2.72 eV for As. The input parameters for InSb include atomic density of 5.78 g/cm³, threshold displacement energies of 12.2 eV for In and 16 eV for Sb, and surface binding energies of 2.49 eV for In and 2.72 eV for Sb…………………………………………………………………….......16

Figure 1.3 The illustration of ion-solid interaction, including sputtering, redeposition, and generation and migration of defects. θ_B is the ion beam angle of incidence…………………………………………………………………17

Figure 1.4 (a) The solid (dashed) line represents the normalized sputtering yield as a function of incident angle from Wei's (Sigmund's) model. (b) Angular dependence of sputtering yield of Si irradiated with 20 keV Ga+ focused-ion-beam. The data points (open circles) represent the sputtering yield at the corresponding beam incidence angle and the solid line (dashed line) represent the fit from the Chen's model (Sigmund's model)………………18

Figure 1.5 The illustration of surface profile for concave, flat and convex. $Y_{concave} > Y_{flat} > Y_{convex}$. The arrows indicate vector of the radii of curvature. For a flat plane, the radius of curvature is infinite…………………………………....19

Figure 1.6 (a) SEM image of the highly ordered nanodots on (100) GaSb surfaces; (b) Cross sectional transmission electron microscopy image of nanodots in Fig. 1.4 (a)……………………………………………….…………………….....20

Figure 1.7 AFM image of InP surface irradiated with 500 eV Ar+, 40° of beam incidence and 150 μA cm^{-2} current density………………….…………….....21

Figure 1.8 (a) Schematic diagram of the ion-beam sputtering system (b) SEM image of the Si-rich cone arrays fabricated by Ar+ irradiation (θ_B=20°) of a silicon substrate (650°C) surrounded by Ni seed materials……………………......22

Figure 1.9 AFM image of Si surface irradiated with 1.2 keV Kr+, 15° of beam incidence and 1.3×10^{19} cm^{-2} ion fluence. The arrow indicates the projected ion beam direction. The solid circle indicates a defect between ripples…………………………………………………………………....23

Figure 1.10 The phase diagrams of (a) GaAs and (b) InSb……………………..…....24

Figure 1.11 (a) the illustration of the preferential sputtering induced changes of surface composition; (b) the plot of the ratio of preferential sputtering flux and composition as a function of depth……………………………………........25

Figure 2.1 (a) Schematic of NOVA 200 dual beam workstation, and (b) schematic of relative orientations of the electron beam, the ion beam, and the sample surface normal (dashed line). The electron beam angle of incidence, θ_e is defined as the angle between the incident electron beam and the sample surface normal. The ion beam angle of incidence, θ_I, is defined as the angle between the incident ion beam and the sample surface normal. The angle between the ion and electron beam columns is fixed at 52°. Therefore, to achieve normal-incidence FIB irradiation, θ_I=0°, the sample must be tilted to 52° with respect to the electron beam. The angle between the electron beam column and secondary electron detector is 90°……………………………42

Figure 2.2 Schematic of FIB raster scanning, which consists of motion of the FIB beam in the positive X direction, followed by moving down one pitch in the positive Y direction. FIB irradiation was carried out with Pitch (p) ranging from 4 to17 nm, beam diameter (2r) ranging from 19 to 23 nm, and beam spot overlap ranging from 10 to 80 %...44

Figure 2.3 Schematic of the Modified Varian Gen II molecular-beam epitaxy system used in these studies. The rf N_2 plasma source is located on one of the effusion cell ports, along with a residual gas analyzer, and seven solid sources (Ga, In, Al, Be, Si, Bi, and As cracker)……………………………45

Figure 2.4 Schematic of the FIB substrate mounted on a TEM grid for nanostructure fabrication via FIB followed by TEM analysis. Ga+ FIB irradiation is in –Z direction. The electron beam for TEM is in +X direction…………………46

Figure 2.5 Schematic of the circuit diagram of the STM-based I-V measurement system……………………………………………………………………47

Figure 3.1 GaAs milled depth for both 10 and 30 kV Ga+ ions with doses are 1.6×10^{16} cm^{-2} and 3.4×10^{16} cm^{-2}. The “negative” milled depth for the ion dose of 1.6×10^{16} cm^{-2} is likely due to ion-induced swelling, similar to literature reports…………………………………………………………………....62

Figure 3.2 SRIM simulations of the implanted ion concentration vs. depth 30 and 10 kV Ga+ in GaAs. The depth of maximum likelihood ion concentration, the projected ion range, R_p, of 30 kV (10kV) Ga+ is ~15 nm (~8 nm)………...63

Figure 3.3 SEM images recorded immediately and ~5 min following the cessation of irradiation with energy and dose of (a), (c) 30 kV, 3.8×10^{16} cm^{-2} and (b), (d)

10 kV, 3.8×10^{16} cm^{-2}. Images (a)–(b) [(c) –(d)] were collected with 52° (normal) angle of incidence. The corresponding size distribution from images (a)–(d) are shown in (e)–(h). The frequency is the percentage of droplets with radii within a specified range. Fits to a lognormal distribution (Gaussian) are shown as dashed (solid) lines, with χ values (e) 0.82, (f) 0.99, (g) 0.90, and (h) 0.87……………………………………………………64

Figure 3.4 SEM images recorded immediately following [(a)–(b)] 30 kV, and [(c)–(d)] 10 kV FIB scanning of a GaAs substrate pre-patterned with an array of holes. The ion fluences are: (a), (c) 2.8×10^{16} cm^{-2} and (b), (d) 6.1×10^{16} cm^{-2}...65

Figure 3.5 Plots of the average droplet radius as a function of fabrication time, which includes both the time of irradiation plus the time-delays between successive scans. (a) includes all droplets in the images. Fits of the 30 kV (10 kV) data to $t^{0.46}$ ($t^{0.3}$) are shown as dotted (dashed) lines, with χ values 0.95 (0.97)...66

Figure 3.6 SEM images of the instantaneous 30 kV Ga^+ irradiated GaAs surfaces. The irradiation times are: (a) 5.8 s, (b) 6.2 s, (c) 6.6 s, (d) 12.4 s, and (e) 28.6 s. (f) shows the droplet size distribution as a function irradiation time. The irradiation times are: 6.4 seconds (black), 6.8 seconds (red), 7.8 seconds (green), and 37.8 seconds (blue)…………………………………………67

Figure 3.7 Droplet surface coverage as a function of irradiation time for 30 kV Ga^+ irradiated GaAs surfaces. The droplet surface coverage is determined as the ratio of total droplet surface areas to total irradiated area. We assumed that the shape of droplets is circular and used the radius of the droplet determined from the IDL code to calculate the total droplet surface. The details of the droplet radius analysis are included in Appendix D……………….………68

Figure 3.8 Droplet speed as a function of droplet radius for 30 kV Ga+ irradiated GaAs surfaces. The average droplet speed is 70±5 nm/s, essentially independent of droplet radius……………………………………………………………69

Figure 3.9 (a) 2D mapping of trajectories of all droplets with respect to their initial positions. The X+ (Y-) and X- (Y+) represent directions along and opposite to the FIB fast (slow) scan direction, as shown in (b). The total numbers of droplets with trajectories in each quadrant are indicated in the 2D map…...70

Figure 3.10 (a) SEM images of the side view of the instantaneous 30 kV Ga^+ irradiated GaAs surfaces. The imaging angle is 83º. (b) Schematic illustration of the contact angles of droplets in motion. θ_A and θ_R indicate the advancing and receding contact angles of a droplet. (c) Schematic illustration of the contact angles of droplets in motion……………………………………………..71

Figure 3.11 (a) Bright-field STEM image of a typical droplet (30 kV, 4.0×10^{16} cm^{-2}) and (b) corresponding XEDS map of Ga (red) and As (green). The plot of f_{Ga} as a function of position in (a) was collected from the area indicated in (b). (c) HRTEM image and corresponding SAD pattern, collected in the vicinity of a typical droplet………………………………………………72

Figure 4.1 Illustration of parallel-mode ripples (a) and perpendicular-mode ripples (b). The arrow indicates the projected ion beam direction; (c) Illustration of the angle of ion beam incidence……………………………………………..85

Figure 4.2 (a) ripple formed on GaAs surface irradiated with 5×10^{17} cm^{-2}; (b)RMS roughness as a function of ion fluence for GaAs surfaces irradiated with 60 keV Ar+ ion at 60° angle of ion beam incidence; (c) ripple formed on GaAs surface irradiated with 1×10^{18} cm^{-2}……………………………………86

Figure 4.3 (a) schematic of the relative orientation of the ion beam and the local surface normal along a FIB-induced trench; (b) the relative sputtering yield of Si irradiated with Ga FIB as a function of θ_{eff}……………………………...87

Figure 4.4 Influence of ion fluence and θeff on InSb surface morphology: (a) 2.3×10^{15} cm^{-2} and 11.6° (b) 3.5 × 1015 cm-2 and 19.7°, (c) 3.6×10^{15} cm^{-2} and 4.2°; (d) 1.0×10^{16} cm^{-2} and 45.4°; (e) 2×10^{16} cm^{-2} and 44.7°; (f) 2.1×10^{16} cm^{-2} and 54.3° (g) 4×10^{16} cm^{-2} and 58.8°, and (h) 4.5×10^{16} cm^{-2} and 72.6°; Pits and islands are observed in (a) and (b); ; perpendicular-mode ripples in (c) and (g); parallel-mode ripples in (d) and (e); hillocks in (f); and featureless surfaces for (h). For all images, the color-scale ranges displayed are 160 nm, and the slow scan direction runs from the top to the bottom of the page. FIB irradiations were carried out using a fixed dwell time of 20μs with pitches of (a) 17nm, (b) 13nm, (d) 8nm, (f) 6nm, and (h) 4nm; or with a fixed pitch of 8 nm and dwell times of (a) 5μs, (b) 25 μs, and (g) 55μs……………………88

Figure 4.5 Logarithm of the RMS roughness as a function of ion fluence. The ion fluence was controlled by varying the pitch (square symbols) or the dwell time (circle symbols). The rms roughness increases linearly with θ_{eff}, presumably due to a corresponding increase in sputtering yield with θ_{eff}….89

Figure 4.6 (a) AFM image of trench milled using the line-scan shown schematically in (b); (c) height profiles with respect to the slow (solid lines) and fast (dashed lines) scan directions, with arrows indicating the edges at which surface profiles were used to estimate θ_{eff}. The θ_{eff} is determined as the height derivative, tan-1(∂h/∂x), at the edge of each trench. We expect this 1D approximation for θ_{eff} to be suitable for 2D if the steady-state θ_{eff} has been reached……………………………………………………………………...90

Figure 4.7 (a) Plots of the measured θ_{eff} and the calculated θ_{eff}^{ss} as a function of scan speed. The open symbols represent the measured θ_{eff} and the solid symbols represent the calculated θ_{eff}^{ss}. The FIB scan speed was tuned via controlling dwell time (square symbols) and pitch (circular symbols)…………………91

Figure 4.8 θ_{eff} dependence of ion-induced surface evolution. +: hillocks/pits; ×: featureless surfaces; □: parallel-mode ripples; ○: perpendicular-mode ripples. (a) pits and islands for θ_{eff} = 8.6±1.7°; (b) parallel-mode ripples for θ_{eff} = 32±2.1°; (c) featureless surfaces for θ_{eff} = 51.8±6.7°; (e) perpendicular-mode ripples for θ_{eff} = 3.5±0.4°; (f) parallel-mode ripples for θ_{eff} = 32.4±2.8°; (g) hillocks for θ_{eff} = 34.6±9.3° (h) perpendicular-mode ripples for θ_{eff} =

49.3±3.9°. For all images, the color-scale ranges displayed are 160 nm, and the slow scan direction runs from the top to the bottom of the page. FIB irradiations were carried out using a fixed dwell time of 20μs with pitches of (a) 17nm, (b) 13nm, (c) 8nm, (d) 6nm, and (h) 4nm; or with a fixed pitch of 8 nm and dwell times of (e) 5μs, (f) 25 μs, (h) 30 μs and (h) 55μs…………………………………………………………………...92

Figure 4.9 Surface roughness as a function of θ_{eff} for both fixed dwell times and pitches. The surface roughness increases linearly with θ_{eff}, presumably due to a corresponding increase in sputter yield with θ_{eff}…………………………...93

Figure 4.10 SEM images of fluence dependence of ripple evolution (for a pitch of 8 nm and dwell time = 10 μs), including (a), (e) (ion fluence of 8×10^{15} cm^{-2}) ripples; (b), (f) (ion fluence of 1.6×10^{16} cm^{-2}) ripples and islands on crests of ripples; (c), (g) (ion fluence of 4×10^{16} cm^{-2}) lateral ordering of nanorods capped with islands; and (d), (h) (ion fluence of 5.6×10^{16} cm^{-2}) randomly distributed nanorods. For all images, the slow scan direction runs from the top to the bottom of the page. Images (a)-(d) ((e)-(h)) were collected with 52° (normal) angle of incidence. The insets in Fig. 3 (e)-(h) are FFT spectra of the SEM images in (a)-(d)………………………………………………94

Figure 4.11 (a) Dark-field STEM image of a single nanorod and (b) corresponding XEDS map of In (red) and Sb (green); HRTEM images and corresponding SAD pattern, collected in the (c) head and (d) body regions of a nanorod...95

Figure 5.1 Illustration of the surface evolution for increasing irradiation time, Ga is represented in red/dark gray and GaSb is light blue/light gray…………...107

Figure 5.2 SEM images of dose dependence of surface evolution, including hillocks/pits and nanodots at (a), (e) for dose of 1 $\times10^{16}$ cm^{-2}; coarse nanodots shown at (b), (f) for dose of 3.1 $\times10^{16}$ cm^{-2}; nanorods capped with nanodots at (c), (g) for dose of 6.9 $\times10^{16}$ cm^{-2}, and at (d), (h) for dose of 1.4 $\times10^{16}$ cm^{-2}. Images (a)-(d) ((e)-(h)) were collected with 52° (normal) angle of incidence…….108

Figure 5.3 (a) and (b) ((c) and (d)) show SEM images of NRs formed on the InSb wafer irradiated with 10 kV (30 kV) ions, respectively. Images (a) and (c) ((b) and (d)) were collected with 0° (75°) angle of incidence……………………...109

Figure 5.4 Illustrations of nanorod formation on (a)-(c) InSb/GaAs heterostructure and (d)-(f) InSb wafer samples…………………………………………….....110

Figure 5.5 SEM images of dose dependence of the InSb/GaAs heterostructure surface evolution, including hillocks and nanoclusters at (a), (e) for dose of 1 $\times10^{16}$ cm^{-2}; coarse nanoclusters shown at (b), (f) for dose of 3.1 $\times10^{16}$ cm^{-2}; NRs capped with nanoclusters at (c), (g) for dose of 6.9 $\times10^{16}$ cm^{-2}; capless truncated-cone NRs at (d), (h) for dose of 1.4 $\times10^{16}$ cm^{-2}. Images (a)-(d) ((e)-(h)) were collected with 0° (75°) angle of incidence……………………...111

Figure 5.6 The height h, and the ratio of top diameter (d) to base diameter (d0) of NRs on InSb wafer (InSb/GaAs heterostructures) for ion fluence of 3.1×10^{16} cm^{-2} and 7×10^{17} cm^{-2} (3.1×10^{16} cm^{-2} and 2.1×10^{17} cm^{-2}), and the corresponding

illustrations of NR evolution on both samples. Linear least-square fits to the t-dependence of h of NRs are shown……………………………………...112

Figure 5.7 Radially-averaged power spectral density (RPSD) vs. frequency obtained from SEM images of irradiated InSb wafer and InSb/GaAs with ion fluence from 3.1×10^{16} cm^{-2} and 1.7×10^{17} cm^{-2}, and the corresponding SEM images of irradiated surfaces of InSb wafer and InSb/GaAs……………………...113

Figure 6.1 Schematic illustrations and the corresponding AFM images of the GaAs surfaces for post-FIB irradiation ((a), (b)) and for post-GaAs overgrowth ((c), (d))……………………………………………………………………...124

Figure 6.2 (a) Illustration of GaAs/Ga/GaAs structure, (b) illustration of GaAs/GaAs structure (c) the PL spectra of the GaAs/Ga/GaAs structure (solid line) and the GaAs/GaAs structure (dashed line)…………………………………...125

Figure 6.3 SEM image of InSb NR arrays. The average NR height is 7.2 μm. This image is a zoom-in view of the NR array shown in Fig. 5.3 (b)…………126

Figure 6.4 (a) TEM images of a 1.4μm InSb NR; (b) SAD of the head and (c) the body as labeled by the circles in (a)……………………………………………..127

Figure 6.5 IV characteristics of an individual cone-shaped InSb NR and the corresponding post I-V measurement TEM images. (a) and (b) for the first I-V measurement; (c) and (d) for the second I-V measurement; (e) and (f) for the third I-V measurement; (g) and (h) for the fourth I-V measurement….128

Figure B.1 Application of non-equilibrium clustering process to Ga-irradiation induced Ga droplet formation GaAs surfaces. Three stages are distinguished: formation, early stage growth, and late stage growth……………………..138

Figure C.1 Ion energy dependent-depth distribution of implanted Ga in GaAs for ion fluence of 3.9×10^{16} cm^{-2}. The solid (dashed) lines are for 10 (30) kV irradiation. The parameters used in the profile code include 10 kV and 30 kV Ga, and 5.315 g/cm^{3} of GaAs density and 7.4 atoms/ion of GaAs sputtering yield…………………………………………………………141

Figure D.1 (a) an SEM image of Ga droplet arrays on GaAs opened in SPIP with the area of interest, selected with a white box; (b) the zoomed in view of the selected droplet with a line-cut across the droplet center; (c) the corresponding height profile for the line-cut through the droplet in (a)…..146

Figure D.2 (a) Height profile of the droplet selected from the image in Fig. D.2; (b) the first derivative of the height profile of the selected droplet. The diameter of the droplets, determined by the distance between the inflection points indicated by vertical dashed lines, in this case, 20.5 pixels……………….147

Figure E.1 Flow Chart for "PRO readimage", an IDL code to identify droplets in each image frame………………………………………………………………….160

Figure E.2 (a) Flow Chart for "PRO tracking", an IDL code to identify and track droplets between image frames. (b) Illustrations show case of droplet motion

and generation. (c) Illustrations show particle coalescence and generation……………………………………………………………161

Figure F.1 Geometry corresponding to the steady motion of a Ga droplet on irradiated GaAs surfaces. θ is the contact angle and γ is the surface interface energy. The subscripts A and R denote the advancing and receding edges of the droplet, respectively, and b is the Navier slip length……………………...165

LIST OF TABLES

Table 2.1 FIB ion energy, ion current, dwell time, ion fluence, ion dose rate, magnification, and irradiation time(s) used in this work…………………...33

Table 2.2 Values of θ_i and θ_e used for various experiments………………………….……….35

Table A.1 Table of ion energies, ion currents, pitches, and beam diameters used for fabrication of droplets, nanorods, and ripples. For ratios of p/d < 0.64, uniform fluxes are expected……………………………………………….133

Table A.2 Thermal properties of GaAs, InAs, InSb and Si…………………………..134

Table A.3 FIB-induced temperature rise on irradiated GaAs, InAs, InSb and Si……135

Table C.1 Sputtering yields of Ga, and As, and $C_{LB}(t)$ determined from SRIM simulations. The ion fluence used for calculation is 3.9×10^{16} cm^{-2}……...140

Table F.1 shows the values of θ_A, θ_R, R, V, γ_{Ga}, $d\gamma/dT$, and the calculated thermal gradient, $\Delta T v$. θ_A, θ_R, R, V are from experimental measurement, and γ_{Ga} and $d\gamma/dT$ are from literature……………………………………………..164

LIST OF APPENDICES

Appendix

A Ion-Solid Interaction: Calculations.…….……..……………………..…131

B Non-equilibrium Clustering Models……………………………………136

C Calculations of FIB Irradiation-Induced Surface Ga concentration, C(t)…………………………………………………………………...139

D Procedure for Determining Ga droplet size…………………………….142

E Ga Droplet Motion Tracking…………………………………………...148

F Droplet Motion: Thermal Gradients……………………………………162

ABSTRACT

Ion beam irradiation-induced pattern formation has the potential to become a cost-effective method for rapid fabrication of large-area nanostructures with dimensions below the limits of conventional photolithography. However, on elemental semiconductor surfaces, ion-induced formation of nanostructures such as nanodots and nanorods occurs only in the presence of impurities. Alternatively, the surface stoichiometry of III-V compounds is easily modified by ion irradiation, thereby enabling self-organization of nanostructures via a balance between preferential sputtering and ion-enhanced diffusion. In this thesis, several approaches to focused ion beam (FIB) -induced formation of nanostructures, including Ga droplets, InSb ripples, and InSb nanorods (NRs), were examined, and new insights into their formation were revealed.

To separately examine Ga droplet formation and coarsening, Ga droplets were fabricated by Ga^{+} FIB irradiation of GaAs substrates with and without pre-patterned holes. We determined the droplet growth rate and size distribution as a function of FIB energy following irradiation. The data suggest a droplet formation mechanism that involves Ga precipitation from a Ga-rich layer, followed by droplet coarsening via a combination of diffusion and Ostwald ripening or coalescence via droplet migration (dynamic coalescence). With further irradiation, droplet motion is apparent, with the net droplet motion in a direction opposite to that of the FIB scanning direction; for droplets in motion, the advancing contact angle is larger than the receding contact angle. Together, these observations suggest that Ga droplet motion is driven by FIB-induced

composition and/or thermal gradients.

To investigate the formation and evolution of ripples on FIB irradiated InSb surfaces, the influence of the local beam incidence angle (θ_{eff}) by varying the distance between beam spots (pitch) and/or the dwell time was examined. With increasing θ_{eff}, the surface morphology evolves from pits to ripples to featureless surfaces. Continued irradiation of the rippled surfaces leads to island formation on the ripple crests, followed by NR growth. This ripple-nanorod transition, triggered by preferential sputtering and island-induced-self-shielding, provides a new approach for producing dense arrays of nanorods.

The formation and evolution of irradiation-induced NRs were examined through a comparison of FIB irradiation of InSb wafers and InSb/GaAs heterostructures. Above a critical ion dose, cone-shaped NRs capped with In islands form on both InSb surfaces. For InSb wafers, the NR base diameter increases with ion energy. In the case of InSb/GaAs heterostructures, as the milled depth approaches the InSb/GaAs interface, the cone-shaped NRs transition to capless NRs with a truncated cone shape. These results suggest a growth mechanism in which both the NR cap and body are supplied by redeposition of atoms sputtered from InSb.

Finally, using FIB irradiation of GaAs surfaces followed by molecular beam epitaxy, Ga droplets were embedded in GaAs. The embedded Ga droplet structures were found to enhance the PL efficiency of GaAs, presumably due to the coupling between Ga plasmon resonance and free carriers in the GaAs.

CHAPTER 1

Introduction

1.1 Overview

Patterning plays a key role in the development of modern science and technology.[1-4] For example, to increase the computation speed and decrease the power consumption of devices, the semiconductor industry aims to continually decrease device size. One of the main challenges for continued device scale-down is the resolution limit of surface patterning techniques. Fig. 1.1 shows the target patterning resolution for production of dynamic random-access memory (DRAM) and Flash memory. During the next 10 years, the target resolution is predicted to decrease from ~35nm to 10 nm.[5] To date, conventional optical lithography has been utilized to control nanostructure sizes and spacings; however, its resolution limit is 22 nm, which does not meet the near-term goals of the IC Roadmap.[5] Therefore, alternative nanopatterning techniques are needed. Ion-sputtering-induced self-assembly, in which ion-irradiation of a flat surface induces spontaneous development of nanoscale morphologies, has emerged as a promising candidate.[6-9] Since ion implantation is currently used for doping, it would be straightforward to use the same equipment for another purpose. Furthermore, ion-

sputtering-induced self-assembly is a one step process; thus, it could be more competitive than several approaches such as e-beam lithography.[2-4,10-13] Both FIB and e-beam lithography are serial and maskless processes; however, the lower mass of electrons in comparison with that of ions limits their applicability to sputtering-induced patterning of semiconductor surfaces. In this thesis, several new approaches to ion-induced self-organization of nanostructures, including nanodots, nanorods, and ripples using a Ga+ focused ion beam (FIB), are discussed.

This chapter opens with a description of ion-solid interactions, followed by a review of factors contributing to preferential sputtering. Next, the influence of broad-beam irradiation-induced sputtering on the formation nanodots, nanorods (NR), and ripples is reviewed and the remaining issues are defined. In the literature, the formation of nanodots, nanorods, and ripples has been attributed to a balance between preferential sputtering and ion-enhanced diffusion. Prior to this thesis research, nanodot fabrication had been limited to continuous irradiation, thereby preventing separate examination of the formation and growth processes. In the case of ripple formation, the balance between sputtering and diffusion is tuned by the ion incidence angle during broad-beam irradiation; however, control of the local angle of ion beam incidence is needed to test this hypothesis in the context of FIB irradiation. For NRs, it has been hypothesized that preferential Group V sputtering leads to the formation of Group III-rich droplets/islands that serve as local sputter masks. However, the development of the NR shape and re-supply of the Group III cap need alternative explanations. Following discussion of each of these topics, the chapter concludes with an outline and the objective of the dissertation.

1.2 Ion-solid interactions

To understand ion-induced morphological evolution, we need to consider ion-solid interactions. The irradiation of solid targets with energetic ions leads to backscattering of incident ions, removal of target atoms (sputtering) at the target surface/sub-surface, and collisions between ions and the target atoms.[14-16] As an ion penetrates a target, it transfers its energy and momentum to the target atoms, causing extensive displacement cascades and point defect generation and migration. The incident ion loses energy due to both nuclear and electronic stopping, both of which depend on the mass and energy of the incident ions and the target atoms.[14,16-20] Nuclear stopping is due to Coulomb interactions between the ion and the nuclei of target atoms. During the nuclear stopping process, energy is dissipated by elastic collisions, leading to the displacement of atoms from their lattice sites and the formation and re-arrangement of point defects.[14] During electronic stopping, energy is lost inelastically by exciting the electrons of the target atoms.[14] Figure 1.2 shows plots of nuclear and electronic energy loss as a function of ion energy for Ga^+ ion irradiation into GaAs and InSb targets.[21] As shown in Fig. 1.2, for ion energies < 30 kV, the stopping energy for Ga^+ in both GaAs and InSb is dominated by nuclear energy loss. Thus, in this energy range, a series of nuclear collisions between moving atoms and other lattice atoms at rest likely leads to the sputtering of surface atoms, generation and migration of point defects, and amorphization. Figure 1.3 shows the illustration of ion-induced sputtering, redeposition, and generation and migration of defects. Among these effects, it is likely that sputtering is the main factor determining the erosion rate and morphological evolution of irradiated

surfaces.[16,22-44]

The sputtering yield, Y, is defined as the average number of atoms leaving the surface of a target per incident ion. It has been suggested that Y depends on the ion energy , E, and the ion beam angle of incidence, θ_B, and the properties of the target including the surface binding energy.[45-49] For both amorphous and polycrystalline elemental targets irradiated with intermediate energy ions, Y increases with E, and is given by[48,50]

$$Y = \Lambda F(E,\eta), \tag{1.1}$$

where $\eta = \cos\theta_B$ and Λ is the materials factor given by

$$\Lambda = \frac{3}{4\pi^2}\frac{1}{NU_0C_0}, \tag{1.2}$$

where N is the atomic density, U_0 is the surface binding energy, and C_0 (~1:808°A^2) is a constant coefficient, utilized in the Thomas-Fermi approximation to the scattering cross-section. The distribution of energy deposited on the surface is often approximated as a Gaussian distribution, as follows[50]

$$F(E,\eta) = \frac{E}{(2\pi)^{1/2}A}\exp(-\frac{\eta^2 a^2}{2A^2}), \tag{1.3}$$

where a is the projected energy range, $A^2 = \eta^2\alpha^2+\eta'^2\beta^2$, α and β are the longitudinal and lateral variation in the projected energy range, and $\eta' = \sqrt{1-\eta^2}$.

For normal incidence $\theta_B = 0$, $\eta = 1$, F(E, η) increases through exponential terms ($\exp(-\frac{\eta^2 a^2}{2A^2})$), while the corresponding depth of sputtered atoms decreases through cosine terms ($\cos\theta_B$) with an increasing θ_B.[45] A balance between these two terms leads to

a maximum in sputtering yield in the range of θ_B = 60° - 80°, as shown in Fig. 1.4 (a).[45] For example, Fig. 1.4 (b) shows the angular dependence of Y of Si irradiated with 20 keV Ga^+ FIB. The maximum Y appears at θ_B = ~80°. In addition, when θ_B is further increased to 90°, Y decreases and finally reaches zero, since the depth of sputtered atoms is zero at θ_B = 90°. In addition, Y is also a function of surface curvature and is given by[51]

$$Y(R) = (1 - d / R)Y_0, \tag{1.4}$$

where d is the ion penetration depth, R is the radius of curvature, and Y_0 is the sputtering yield of a flat surface. Therefore, the surfaces with negative radius of curvature have higher Y than these with positive curvature or flat surface. For example, Fig. 1.5 shows the surface profiles of concave ($R < 0$), flat ($R = \infty$), and convex ($R > 0$) surfaces. Therefore, $Y_{concave}$ is expected to be higher than Y_{flat} and $Y_{concave}$.

For multicomponent materials, the differences in masses and surface binding energies of components often lead to preferential sputtering of one of the elements, leading to sputtered particles with different composition than those of the target surface.[47,49,52-57] Consequently, the preferential removal of certain components from the surfaces often leads to the formation of surface layer with a composition different from the bulk stoichiometry.[58] At sufficiently low temperatures, the thickness of the altered layers is dependent on ion energy, and its composition remains in a steady state.[52] For example, for a steady-state sputtering of a binary compound AB, the ratio of the surface component can be approximated by [52,56]

$$\frac{C_A^S}{C_B^S} = \frac{C_A}{C_B}\left(\frac{M_A}{M_B}\right)^{2m}\left(\frac{U_A}{U_B}\right)^{1-2m}, \tag{1.5}$$

where C_i is the bulk concentration, C_i^S is the surface concentration, Y_i is the sputtering

yield , m_i is the atomic mass, U_i is the surface binding energy, m is an energy-dependent parameter. For example, m = 1 at high energies (>100keV), m = 0.5 for medium energies (10-100 keV), and $0 \leq m \leq 5$ for lower energies (<10keV).[52,56]

1.3 Nanodot formation

Broad-beam irradiation-induced nanodot formation has been observed by either normal incidence irradiation of a stationary substrate or off-normal incidence irradiation of a rotating substrate.[28,59,60] In all cases, the ion-induced nanostructures are reported have the same stoichiometry as the substrate. However, FIB-induced nanostructures typically have different compositions than their substrates, possibly due to enhanced redeposition at the side-walls of the implanted area, [61,62] and/or to differences in the collision cascade density. FIB irradiation typically involves much higher current densities than that of broad-area irradiation, and thus has higher collision cascade density.[63] The high collision cascade density leads to a local heat spike in which the irradiated region of the substrate is melted and solidified. Since III-V compounds are line compounds, the re-solidification process might lead to the change of composition. For example, during the re-solidification process, the GaAs compound might form Ga droplets and As crystals.[64] For example, Facsko et al. reported the formation of ~35 nanometer diameter nanodots using normal-incidence broad-areairradiation of GaSb surfaces, as shown in Figs. 1.6 (a) and (b).[28] The nanodots appeared following 40 seconds of irradiation (4×10^{17}cm^{-2}) and their height increased with continued irradiation. For irradiation duration > 200 seconds (2×10^{18}cm^{-2}), the nanodots formed a highly

ordered hexagonal array, as shown in Fig. 1.6(a). The cross-sectional TEM image of the nanodots, shown in Fig. 1.6(b), reveals single crystal GaSb nanodots, consistent with the stoichiometry of the substrate. On the other hand, as shown in Fig. 1.5, Frost et al. reported nanodot array formation on rotating InP targets irradiated at θ_B=40.[60] In this case, InP nanodots appear at the onset of irradiation and their lateral size and height increased with continued irradiation. For irradiation duration > 9600 seconds, the topography changes from an irregular to a highly regular hexagonal array of nanodots.

The formation of ion-induced nanodot arrays with the same stoichiometry as the substrate has been explained by the combined influences of curvature-dependent sputtering and diffusion. On the other hand, FIB irradiation of III-V compounds leads to the formation of surface nanodots with composition substantially different from that of the substrate. We note that both broad-beam and FIB irradiation use similar ranges of ion dose, 10^{15}-10^{18} cm^{-2}; however the dose rates are not typically reported in the literature. Recently, Bradley et al. proposed that coupling between curvature-driven diffusion, composition gradient-driven diffusion, and composition-dependent sputtering is key to the formation of hexagonal arrays of nanodots.[22,65] On the other hand, it was recently proposed that ion-induced formation of hexagonal arrays of Ga droplets on GaAs is due to anisotropic mass transport induced by shielding of the GaAs substrate by Ga droplet. With off-normal irradiation, droplets shield the GaAs surface along the projected ion beam direction, leading to reduced sputtering and therefore fewer Ga adatoms. Hence, to enable Ga adatom capture, the net motion of Ga droplets is opposite to that of the projected ion beam direction, resulting in the formation of hexagonal arrays of Ga droplets. Although these new models have been proposed to explain the formation of

metal droplets and their ordered arrays, the origins of random ensembles are unclear.

1.4 Ripple formation

Ripple formation was first reported in 1962 for glancing-incidence irradiation of uranium surfaces irradiated with 3 – 15 keV Ar^+ ions.[66] Subsequently, numerous systematic and quantitative investigations of ripple formation have been conducted using a variety of ions to irradiate various metals, semiconductors, and insulators.[27,29,31,34,38,39,44,67,68] The reported ripple wavelengths range from 10 to 1000 nm, with typical ratios of height to wavelength (aspect ratio) of 0.1 or less. In addition, the ripple wavevector is either parallel or perpendicular to the projected ion beam direction, often termed "parallel-mode" or "perpendicular-mode" ripples, respectively. For example, Fig. 1.8 shows the AFM image of the parallel-mode ripples on Si surfaces irradiated with 1.2 keV Kr^+ ions.[44]

The most widely discussed ripple-formation model is the Bradley-Harper (BH) model.[51] In this model, sputtering-induced roughening and diffusion-induced smoothening induce linear growth of surface perturbations. The BH model predicts several characteristics for ripples formed on elemental semiconductor surfaces, including (1) time-independent ripple wavelengths, (2) exponentially-growing ripple amplitude, and (3) ripple wave vectors oriented parallel to the projected beam direction (→) for normal incidence (θ_B =0) and perpendicular to the projected beam incidence direction for a grazing incidence. In particular, these phenomena have been observed on single element semiconductors such as Si and Ge with irradiation using 500 - 1.2 keV ions, with

ion fluences ranging from 10^{15} to 10^{18} cm^{-2}. However, the BH model is unable to predict other trends including ion-incidence angle dependent surface evolution, saturation of the ripple amplitude elemental semiconductor surfaces), and formation of hexagonal arrays of metallic nanodots (compound semiconductor surfaces). Therefore, in subsequent studies, the BH model has been further expanded to consider the effects of ion fluence, flux, energy, incidence angle, sample temperature, and surface crystallinity on the growth kinetics of ion irradiation-induced ripple patterns.[7,24,26,27,69-78]

1.5 Nanorod formation

Irradiation induced-microscopic cone formation was first observed on surfaces of polycrystalline materials used for glow discharge cathodes.[79] Gunterschule et al. proposed that surface impurity clusters, with a smaller sputtering yield than that of substrates, would cause the development of cones.[79] Later, various surface structures including cones, pyramids, nanorods (NRs), and whiskers were produced by ion irradiation with metal wires placed on the substrate surfaces.[32,35,41,80] However, due to the limited supply of metal sources, these approaches were only used to fabricate small areas of surface structures. Shang et al. proposed a new configuration for the formation of large-area arrays of Si cones, consisting of ion-irradiation of substrate surrounded by a metal sheet, as shown in the Fig. 1.7 (a).[40] For example, Fig. 1.7 (b) shows an SEM image of Si-rich cone arrays fabricated by Ar+ irradiation of a silicon substrate surrounded by Ni seed materials.[40]

Recently ion-induced NR formation on compound semiconductor surfaces has been

explored by a variety of authors.[32,35,40,81] For example, Roy et al. irradiated GaSb surfaces without metal seeds; the result NR formation was attributed to combined sputtering and irradiation-induced phase separation of GaSb.[33,82] Prior to my thesis work, the formation of NRs, nanopillars and nanospikes on various III-V compound semiconductor surfaces, was explained by the so-called "self-sustained etch masking" model, in which preferential sputtering and ion-enhanced diffusion lead to the formation of NRs with Group III NR caps.[81,83-85] In this model, preferential Group V sputtering leads to the formation of a Group III-rich droplets/islands that serve as local sputter masks. It has been proposed that the Group III droplets/islands are resupplied by ion-enhanced diffusion of group III elements precipitated from the NR body and the substrate. These Group III droplets/islands act as a sputter mask and induce the formation of truncated cones, which are inconsistent with the observed cone-shaped and spike-shaped NR.[36,81]

In addition, the growth rate is determined by the Group III flux multiplied by the difference in sputtering yields between the Group III element and the III-V substrate. As the NRs grow longer, the path length from the substrate to the NR cap increases, resulting in a decreasing NR growth rate. Since the sputtering yield of III-V compounds are typically smaller than those of Group III elements, an alternative mechanism for re-supply of the Group III caps needs to be identified. However, for most experimental observations, the width of NR cap is smaller than that of NR body; thus, this sputter masking model is not sufficient to explain the ion-induced NR formation.

1.6 Dissertation Objectives

As discussed in Section 1.3, 1.4 and 1.5, broad-beam and FIB irradiation have been used to fabricate nanostructures, including nanodots, NRs, and ripples. Generally, the formation of these nanostructures, on both elemental and compound semiconductor surfaces, is attributed to a competition between preferential sputtering and ion-enhanced diffusion. For nanodot formation, prior work was limited to continuous irradiation; thus, the processes of nucleation, growth, and motion occurred concurrently. Separate examination of the nanodot formation and growth was needed. In the case of ripple formation, the competition between curvature-dependent sputtering and diffusion is tuned by the ion incidence angle during broad-beam irradiation; however, for FIB irradiation, control of the local angle of ion beam incidence is needed to test this hypothesis. For NRs, in the "self-sustained etch masking model", preferential Group V sputtering is proposed to lead to the formation of Group III-rich droplets/islands that serve as local sputter masks. However, this model cannot explain the re-supply of the Group III cap. need alternative explanations. In addition, this model predicts the formation of NR with a truncated-cone shape. Since most ion-induced NR are either cone-shaped or spike shaped.[36,81] a revised model for ion-induced NR formation is needed.

In this thesis, we explore Ga^+ FIB irradiation of III-V compound semiconductors. Since FIB irradiation typically provides higher current densities than its broad-area counterparts, enhanced ion-solid interactions are expected. Furthermore, the side walls of the implanted area will block sputtered atoms, thereby increasing re-deposition.[61] Presumably the increased volatility of Group V elements in comparison to that of Group III elements would then lead to enhanced Group III re-deposition and nanostructures with

compositions which differ from that of the substrate. Furthermore, III-V compounds are line compounds; thus, an ion-induced modification to the surface stoichiometry is expected to push the system into a two phase regime, as shown in the GaAs and InSb phase diagrams in Figs. 1.10 (a) and 1.10 (b) respectively. Figure 1.11 (a) and (b) illustrate the preferential sputtering-induced modifications to the surface stoichiometry, and the corresponding plot of the ratio of preferential sputtering flux and composition as a function of depth, respectively. The preferential sputtering of III-V compounds is expected to induce phase decomposition, leading to anisotropic sputtering of the irradiated surfaces and evolution of the surface morphology.

1.7 Outline of the Dissertation

The thesis is organized as follows: Chapter 2 describes the experimental procedures used for this work, including focused ion beam (FIB), molecular beam epitaxy growth (MBE), scanning electron microscopy (SEM), atomic force microscopy (AFM), Rutherford backscattering (XEDS), transmission electron microscopy (TEM), x-ray energy dispersive spectrum (XEDS), and Photoluminescence (PL), and IV measurements in a TEM.

In Chapter 3, we describe our investigation of the formation, growth, and motion of droplets on FIB-irradiated GaAs surfaces. First, we study the ion-energy dependence of Ga droplet formation on irradiated GaAs. To separately examine formation and coarsening, Ga droplets were fabricated by FIB irradiation of GaAs substrates with and without pre-patterned holes. We determined the droplet growth rate and size distribution

as a function of FIB energy following irradiation. The data suggest a droplet formation mechanism that involves Ga precipitation from a Ga rich layer, followed by droplet coarsening via a combination of diffusion and ripening or coalescence via droplet migration (dynamic coalescence). With further irradiation, we observe net motion of droplet ensembles in a direction opposite to the ion beam scanning direction. Interestingly, for the droplets in motion, the advancing contact angle is larger than its receding contact angle. Together, these observations suggest that Ga droplet motion is driven by FIB-induced composition and/or thermal gradients.

In Chapter 4, we discuss the formation and evolution of ripples on FIB irradiated compound semiconductor surfaces. Using normal incidence Ga^+ irradiation of InSb, we tuned the local beam incidence angle (θ_{eff}) by varying the distance between beam spots (pitch) and/or the dwell time. With increasing θ_{eff}, the surface morphology evolves from pits to ripples to featureless surfaces. Continued irradiation of the rippled surfaces leads to the formation of islands on the ripple crests, followed by nanorod growth. This ripple-nanorod transition, triggered by preferential sputtering and island-induced-self-shielding, provides a new approach for achieving dense arrays of nanorods.

In Chapter 5, we present our studies on the relative roles of ion-enhanced diffusion and redeposition in the formation and growth of irradiation-induced NRs. We have examined the nanoscale mechanisms of NR evolution through a comparison of the normal incidence irradiation of InSb/GaAs heterostructures and InSb wafers. We show a transition from cone-shaped NRs capped with In islands to capless NRs with a truncated-cone shape, and propose an ion-induced NR growth mechanism in which both the NR cap and body are supplied by redeposition of atoms sputtered from InSb.

Conclusions and suggestions for future work are discussed in Chapter 6.

1.8 Figures and References

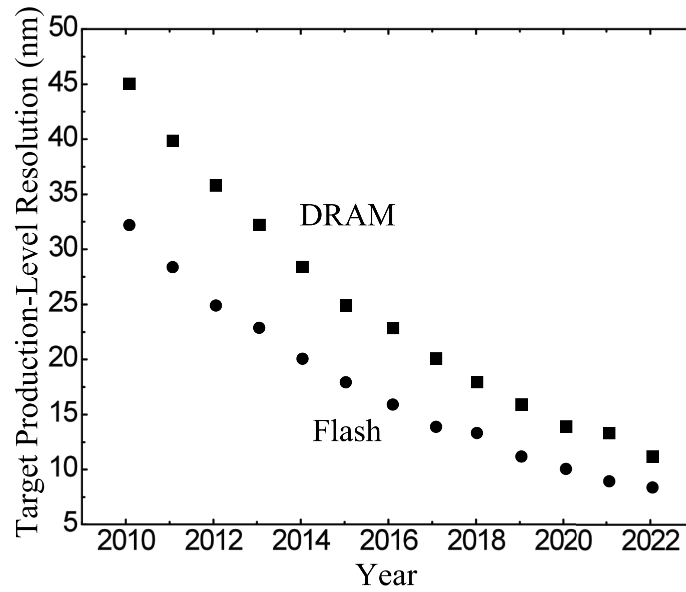

Figure 1.1 Target production-level patterning resolution ,for DRAM and Flash, as a function of year. Adopted from the International Technology Roadmap.[5]

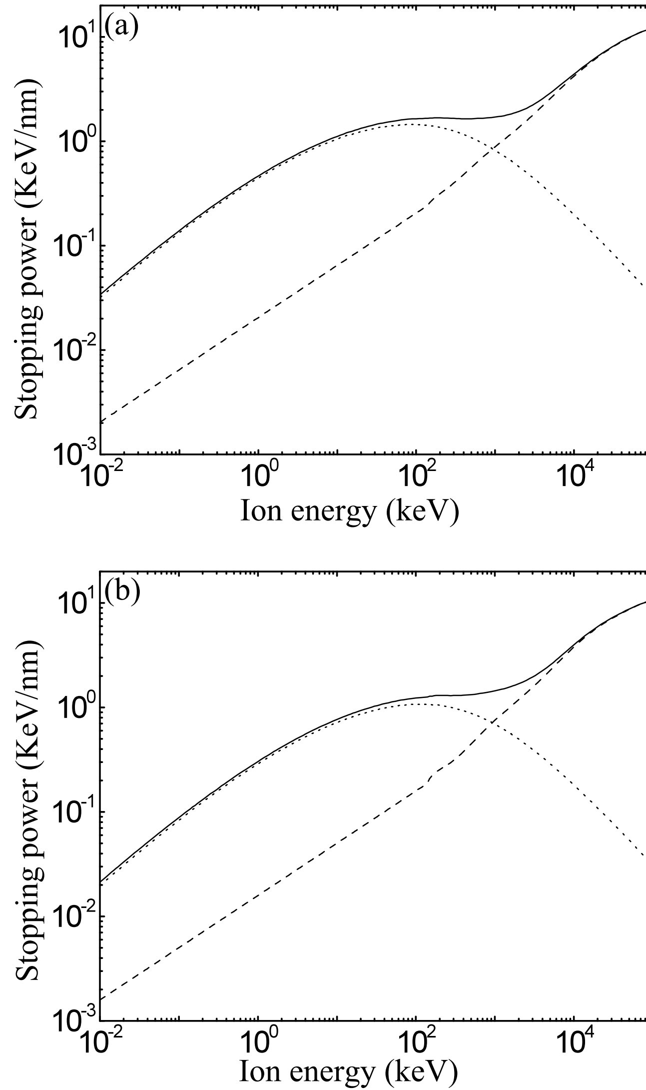

Figure 1.2 The nuclear (dotted line), electronic (dashed line) and total (solid line) stopping power as a function of kinetic energy for Ga+ ion irradiation of (a) GaAs and (b) InSb target. The data are calculated using the SRIM 2010 Monte Carlo simulation code.[21] For these simulations, it was assumed that the sublimation energy is equivalent to the surface binding energy [24]. The input parameters for GaAs [25] include and atomic density of 5.32 g/cm³ for GaAs, threshold displacement energies of 12.4 eV for Ga and 20.8 eV for As, and surface binding energies of 2.82 eV for Ga and 2.72 eV for As. The input parameters for InSb [26] include atomic density of 5.78 g/cm³, threshold displacement energies of 12.2 eV for In and 16 eV for Sb, and surface binding energies of 2.49 eV for In and 2.72 eV for Sb.

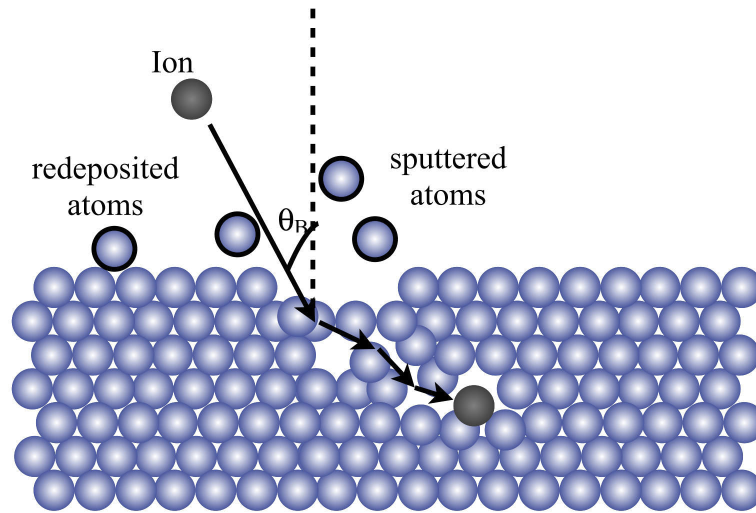

Figure 1.3 The illustration of ion-solid interaction, including sputtering, redeposition, and generation and migration of defects. θ_B is the ion beam angle of incidence.

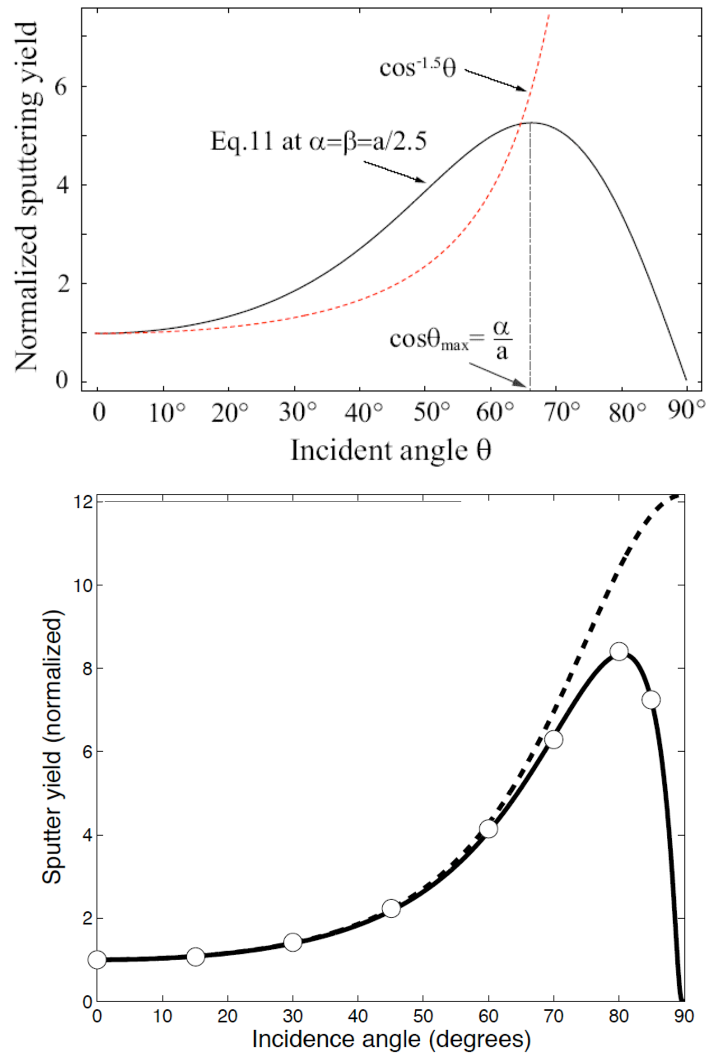

Figure 1.4 (a) The solid (dashed) line represents the normalized sputtering yield as a function of incident angle from Wei's (Sigmund's) model. (b) Angular dependence of sputtering yield of Si irradiated with 20 keV Ga^+ focused-ion-beam. The data points (open circles) represent the sputtering yield at the corresponding beam incidence angle and the solid line (dashed line) represent the fit from the Chen's model (Sigmund's model).[48,86] Reprinted figure with permission from H. H. Chen, O. A. Urquidez, S. Ichim, L. H. Rodriguez, M. P. Brenner, and M. J. Aziz, Science 310, 294 (2005). Copyright 2005 by American Association for the Advancement of Science.

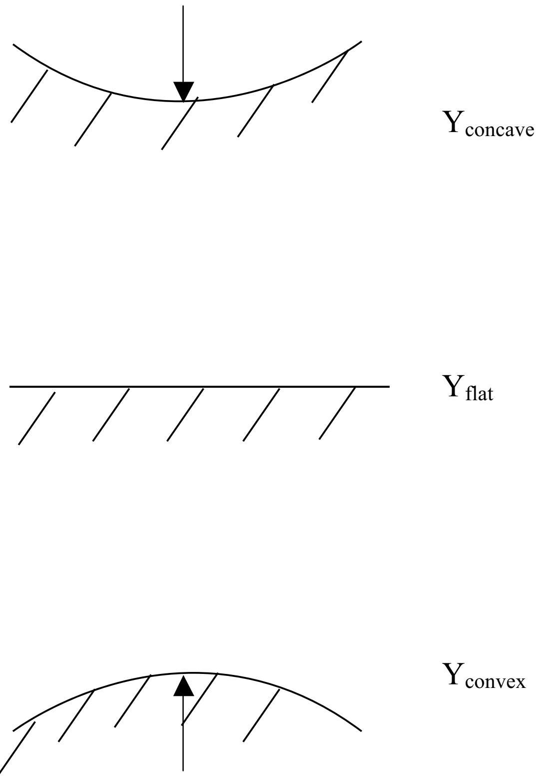

Figure 1.5 The illustration of surface profile for concave, flat and convex. $Y_{concave} > Y_{flat} > Y_{convex}$. The arrows indicate vector of the radii of curvature. For a flat plane, the radius of curvature is infinite.

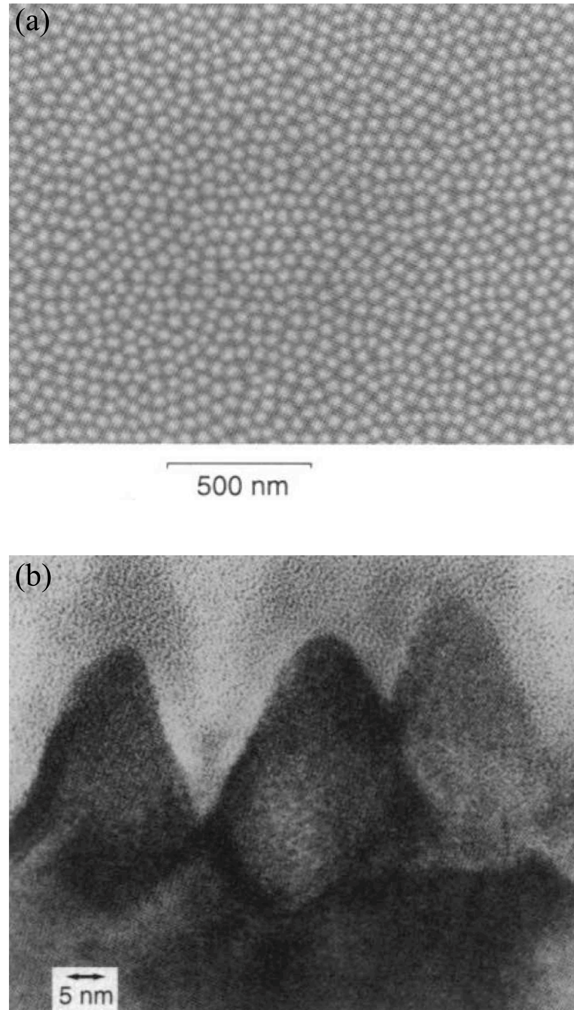

Figure 1.6 (a) SEM image of the highly ordered nanodots on (100) GaSb surfaces; (b) Cross sectional transmission electron microscopy image of nanodots in Fig. 1.4 (a). Reprinted figure with permission from S. Facsko, T. Dekorsy, C. Koerdt, C. Trappe, H. Kurz, A. Vogt, H. L. Hartnagel, Science 285, 1551 (1999). Copyright 1999 by American Association for the Advancement of Science.

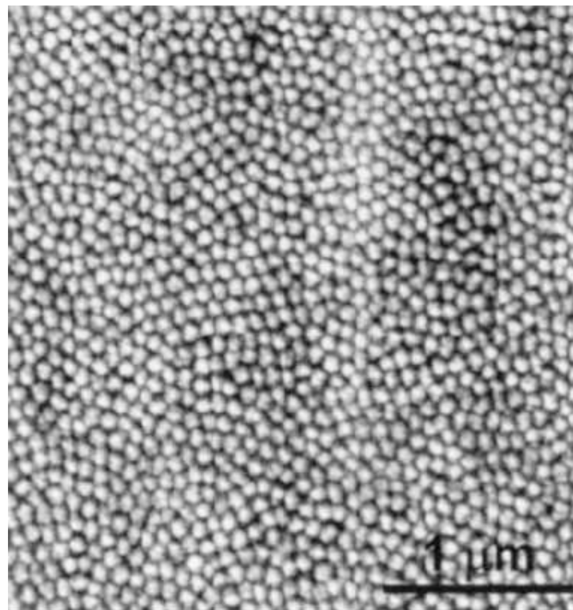

Figure 1.7 AFM image of InP surface irradiated with 500 eV Ar^+, 40° of beam incidence and 150 ∝A cm^{-2} current density. Reprinted figure with permission from F. Frost, A. Schindler and F. Bigl, Phys. Rev. Lett. Vol. 85, 4116 (2000). Copyright 2000 by the American Physical Society.

(a)

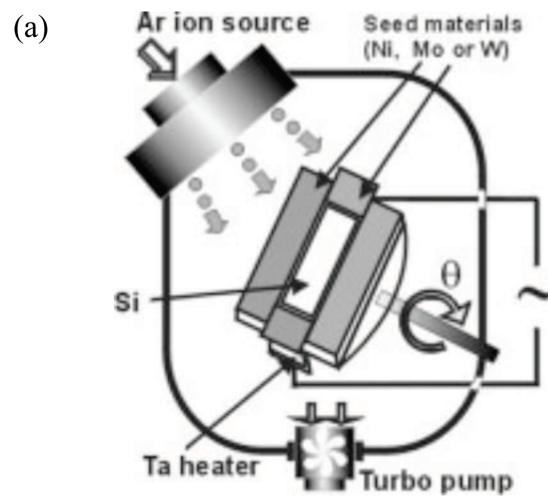

(b)

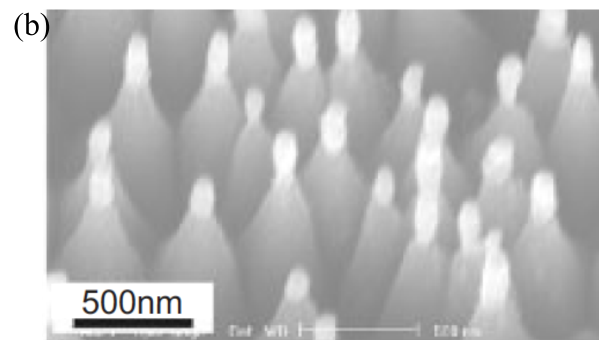

Figure 1.8 (a) Schematic diagram of the ion-beam sputtering system (b) SEM image of the Si-rich cone arrays fabricated by Ar+ irradiation (θ_B=20°) of a silicon substrate (650°C) surrounded by Ni seed materials. Reprinted figure with permission from N. G. Shang, F. Y. Meng, F. C. K. Au, Q. Li, C. S. Lee, I. Bello, and S. T. Lee, Adv. Mater. 14, 1308 (2002). Copyright 2002 by the WILEY-VCH Verlag GmbH & Co. KGaA, Weinheim.

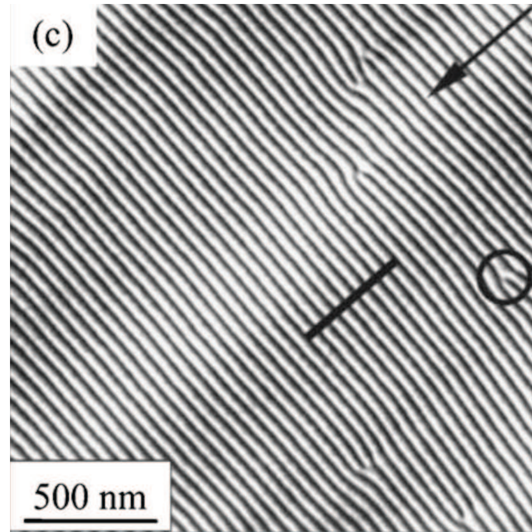

Figure 1.9 AFM image of Si surface irradiated with 1.2 keV Kr^+, 15° of beam incidence and 1.3×10^{19} cm^{-2} ion fluence. The arrow indicates the projected ion beam direction. The solid circle indicates a defect between ripples. Reprinted figure with permission from B. Ziberi, M. Cornejo, F. Frost, and B. Rauschenbach, J. Phys-Condens. Mat. 21, 224003 (2009). Copyright 2009 by IOP publishing Ltd.

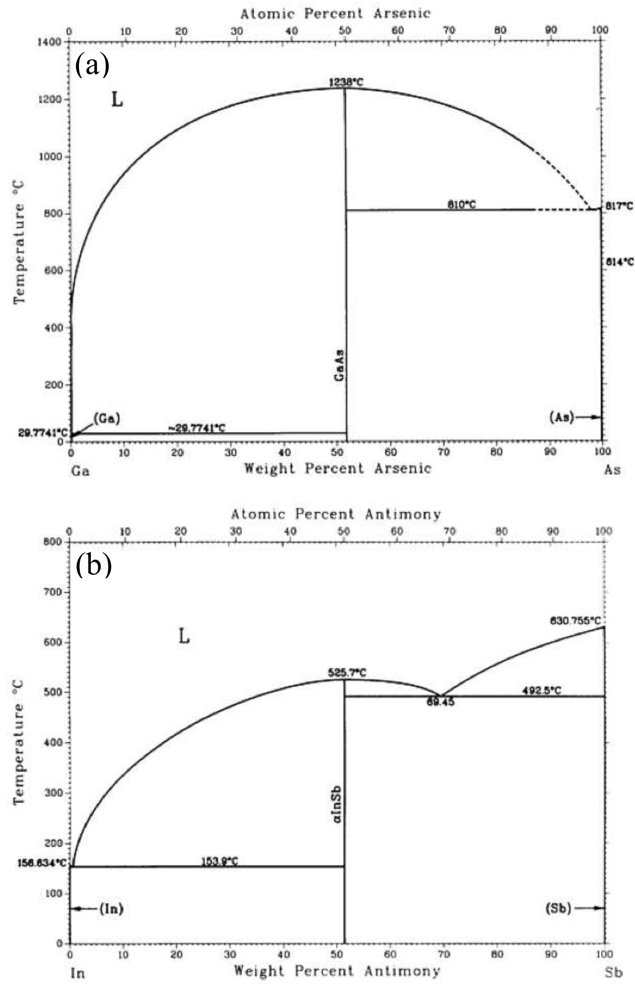

Figure 1.10 The phase diagrams of (a) GaAs and (b) InSb. Reprinted figure with permission from Larry Kaufman, Janine Nell, Keith Taylor, Fred Hayes, Calphad 5, 185 (1981). Copyright 1981 by Elsevier.

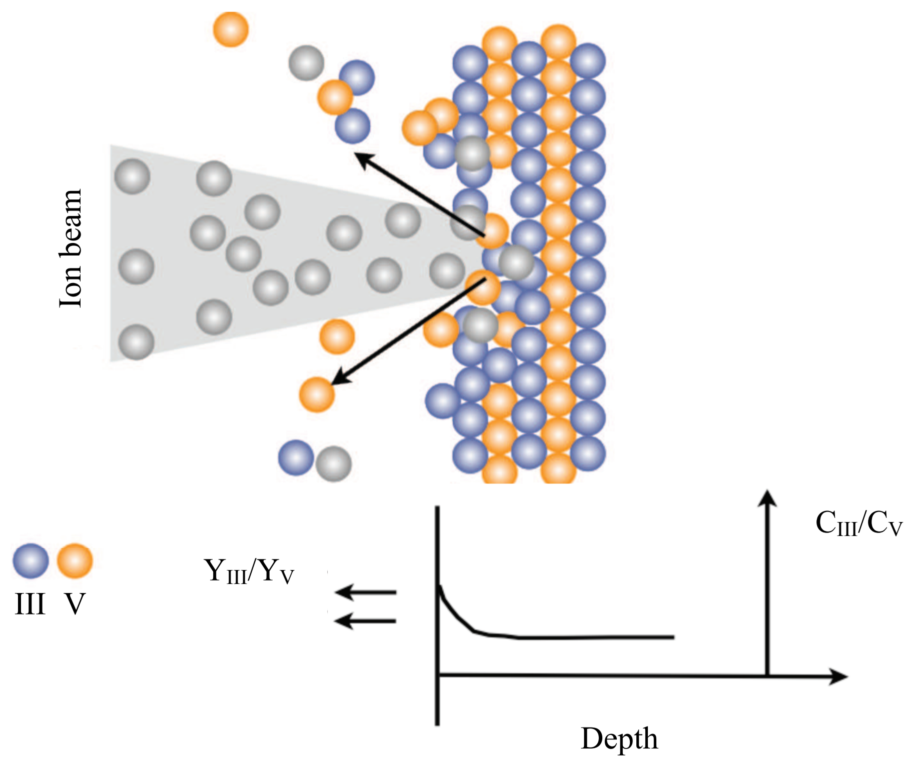

Figure 1.11 (a) the illustration of the preferential sputtering induced changes of surface composition; (b) the plot of the ratio of preferential sputtering flux and composition as a function of depth.[58]

[1]P. S. Cremer, J. Am. Chem. Soc. **133,** 167 (2011).

[2]M. Geissler and Y. N. Xia, Adv. Mater. **16,** 1249 (2004).

[3]R. D. Piner, J. Zhu, F. Xu, S. H. Hong, and C. A. Mirkin, Science **283,** 661 (1999).

[4]B. D. Gates, Q. B. Xu, M. Stewart, D. Ryan, C. G. Willson, and G. M. Whitesides, Chem. Rev. **105,** 1171 (2005).

[5]*The International Technology Roadmap for Semiconductors* (Semiconductor Industry Association 2012).

[6]R. Cuerno and M. Castro, *Toward Functional Nanomaterials*, Vol. 5 (Springer New York, New York, 2009).

[7]M. Castro, R. Cuerno, L. Vazquez, and R. Gago, Phys. Rev. Lett. **94,** 4 (2005).

[8]F. Frost, B. Ziberi, T. Hoche, and B. Rauschenbach, Nucl. Instrum. Meth. B **216,** 9 (2004).

[9]F. Frost, B. Ziberi, A. Schindler, and B. Rauschenbach, Appl. Phys. A-Mater. **91,** 551 (2008).

[10]S. Y. Chou, P. R. Krauss, W. Zhang, L. J. Guo, and L. Zhuang, J. Vac. Sci. Technol. B **15,** 2897 (1997).

[11]S. Y. Chou, P. R. Krauss, and P. J. Renstrom, Science **272,** 85 (1996).

[12]M. Park, C. Harrison, P. M. Chaikin, R. A. Register, and D. H. Adamson, Science **276,** 1401 (1997).

[13]Y. N. Xia and G. M. Whitesides, Annu. Rev. Mater. Sci. **28,** 153 (1998).

[14]Michael Nastasi, James W. Mayer, and J. K. Hirvonen, *Ion-Solid Interactions: Fundamentals and Applications* (Cambridge University Press, New York, 1996).

[15]R. A. Johnson and A. N. Orlov, *Physics of Radiation Effects in Crystals* (North-Holland, New York, 1986).

[16]R. Behrisch, P. Sigmund, M. T. Robinson, H. H. Andersen, H. L. Bay, and H. E. Roosendaal, *Sputtering by Particle Bombardment I*, Vol. 47 (Springer-Verlag, New York, 1981).

[17]J. F. Ziegler, J. P. Biersack, and U. Littmark, *The Stopping and Range of Ions in Matter.* (Pergamon Press, New York, 1985).

[18]P. Sigmund, Appl. Phys. Lett. **14,** 114 (1969).

[19]P. Sigmund, Phys. Rev. **17,** 969 (1972).

[20]P. Sigmund, Nucl. Instrum. Meth. B **27,** 1 (1987).

[21]SRIM, http://www.srim.org/.

[22]R. M. Bradley and P. D. Shipman, Phys. Rev. Lett. **105,** 145501 (2010).

[23]G. Carter and V. Vishnyakov, Phys. Rev. B **54,** 17647 (1996).

[24]W. L. Chan and E. Chason, J. Appl. Phys. **101,** 46 (2007).

[25]D. Datta, Bhattacharyya, Sr., T. K. Chini, and M. K. Sanyal, Nucl. Instrum. Meth. B **193,** 596 (2002).

[26]B. Davidovitch, M. J. Aziz, and M. P. Brenner, Phys. Rev. B **76,** 12 (2007).

[27]J. Erlebacher, M. J. Aziz, E. Chason, M. B. Sinclair, and J. A. Floro, J. Vac. Sci. Technol. A **18,** 115 (2000).

[28]S. Facsko, T. Dekorsy, C. Koerdt, C. Trappe, H. Kurz, A. Vogt, and H. L. Hartnagel, Science **285,** 1551 (1999).

[29]S. Habenicht, W. Bolse, K. P. Lieb, K. Reimann, and U. Geyer, Phys. Rev. B **60,** R2200 (1999).

[30]S. Habenicht, K. P. Lieb, J. Koch, and A. D. Wieck, Phys. Rev. B **65,** 6 (2002).

[31]R. L. Headrick and H. Zhou, J. Phys. Condens. Mat., **21,** 224005 (2009).

[32]J. Kato, M. Nozu, Y. Fujimoto, M. Tanemura, and F. Okuyama, J. Vac. Sci. Technol. A **13,** 207 (1995).

[33]S. Le Roy, E. Barthel, N. Brun, A. Lelarge, and E. Sondergard, J. Appl. Phys. **106,** 5 (2009).

[34]S. W. MacLaren, J. E. Baker, N. L. Finnegan, and C. M. Loxton, J. Vac. Sci. Technol. A **10,** 468 (1992).

[35]S. Morishita, Y. Fujimoto, and F. Okuyama, Surf. Sci. **202,** L587 (1988).

[36]S. Morishita and F. Okuyama, J. Vac. Sci. Technol. A **8,** 3295 (1990).

[37]S. Morishita and F. Okuyama, J. Vac. Sci. Technol. A **9,** 331 (1991).

[38]F. Rose, H. Fujita, and H. Kawakatsu, Nanotechnology **19,** 7 (2008).

[39]S. R. Saeed, O. P. Sinha, F. Krok, T. Zembok, R. Pedrys, and M. Szymonski, Nucl. Instrum. Meth. B **267,** 2752 (2009).

[40]N. G. Shang, F. Y. Meng, F. C. K. Au, Q. Li, C. S. Lee, I. Bello, and S. T. Lee, Adv. Mater. **14,** 1308 (2002).

[41]G. K. Wehner and D. J. Hajicek, J. Appl. Phys., **42,** 1145 (1971).

[42]Q. Wei, J. Lian, W. Lu, and L. M. Wang, Phys. Rev. Lett. **100,** 076103 (2008).

[43]J. H. Wu, W. Ye, B. L. Cardozo, D. Saltzman, K. Sun, H. Sun, J. F. Mansfield, and R. S. Goldman, Appl. Phys. Lett. **95,** 3 (2009).

[44]B. Ziberi, M. Cornejo, F. Frost, and B. Rauschenbach, J. Phys. Condens. Mat. **21,** 224003 (2009).

[45]Q. M. Wei, K. D. Li, J. Lian, and L. M. Wang, J. Phys. D **41,** 172002 (2008).

[46]T. Ishitani and T. Ohnishi, J. Vac. Sci. Technol. A **9,** 3084 (1991).

[47]J. B. Malherbe, Crit. Rev. Solid State Mater. Sci. **19,** 55 (1994).

[48]P. Sigmund, Phys. Rev. **184,** 383 (1969).

[49]H. H. Andersen, Nucl. Instrum. Meth. B **18,** 321 (1987).

[50]P. Sigmund, J. Mater. Sci. **8,** 1545 (1973).

[51]R. M. Bradley and J. M. E. Harper, J. Vac. Sci. Technol. A **6,** 2390 (1988).

[52]J. B. Malherbe, Crit. Rev. Solid State Mater. Sci. **19,** 129 (1994).

[53]R. Kelly, Nucl. Instrum. Methods **149,** 553 (1978).

[54]R. Kelly, Surf. Sci. **100,** 85 (1980).

[55]R. Kelly and D. E. Harrison, Mater. Sci. Eng., 69, 449 (1985).

[56]P. Sigmund, A. Oliva, and G. Falcone, Nucl. Instrum. Meth. **194,** 541 (1982).

[57]J. B. Malherbe, S. Hofmann, and J. M. Sanz, Appl. Surf. Sci. **27,** 355 (1986).

[58]J. S. Williams and J. M. Poate, *Ion Implantation and Beam Processing* (Academic Press, New York, 1984).

[59]F. Frost, B. Ziberi, T. Hoche, and B. Rauschenbach, Nucl. Instrum. Meth. B **216,** 9 (2004).

[60]F. Frost, A. Schindler, and F. Bigl, Phys. Rev. Lett. **85,** 4116 (2000).

[61]H. Yamaguchi, A. Shimase, S. Haraichi, and T. Miyauchi, Nucl. Instrum. Meth. B **3,** 71 (1985).

[62]W. Bolse, Mater. Sci. Eng. Rev-Rep. **12,** 53 (1994).

[63]J. B. Wang and Y. L. Wang, Appl. Phys. Lett. **69,** 2764 (1996).

[64]L. M. Foster and J. F. Woods, J. Electrochem. Soc. **118,** 1175 (1971).

[65]R. M. Bradley and P. D. Shipman, Appl. Surf. Sci. **258,** 4161 (2012).

[66]M. Navez, C. Sella, and D. Chaperot, Acad. Sci., Paris, C. R. **254,** 240 (1962).

[67]Z. X. Jiang and P. F. A. Alkemade, J. Vac. Sci. Technol. B **16,** 1971 (1998).

[68]T. E. Karakasidis, D. G. Papageorgiou, and G. A. Evangelakis, Appl. Surf. Sci. **162,** 233 (2000).

[69]M. A. Makeev, R. Cuerno, and A. L. Barabasi, Nucl. Instrum. Methods Phys. B **197,** 185 (2002).

[70]V. B. Shenoy, W. L. Chan, and E. Chason, Phys. Rev. Lett. **98,** 4 (2007).

[71]C. S. Madi, E. Anzenberg, K. F. Ludwig, and M. J. Aziz, Phys. Rev. Lett. **106,** 4 (2011).

[72]C. S. Madi, B. Davidovitch, H. B. George, S. A. Norris, M. P. Brenner, and M. J. Aziz, Phys. Rev. Lett. **101,** 4 (2008).

[73]A. D. Brown and J. Erlebacher, Phys. Rev., **72,** 10 (2005).

[74]A. D. Brown, J. Erlebacher, W. L. Chan, and E. Chason, Phys. Rev. Lett. **95,** 4 (2005).

[75]E. A. Eklund, R. Bruinsma, J. Rudnick, and R. S. Williams, Phys. Rev. Lett. **67,** 1759 (1991).

[76]J. Erlebacher, M. J. Aziz, E. Chason, M. B. Sinclair, and J. A. Floro, Phys. Rev. Lett. **82,** 2330 (1999).

[77]I. Koponen, M. Hautala, and O. P. Sievanen, Phys. Rev. Lett. **78,** 2612 (1997).

[78]C. C. Umbach, R. L. Headrick, and K. C. Chang, Phys. Rev. Lett. **87,** 4 (2001).

[79]A. Guntherschulze and W. Tollmien, Z. Phy. **119,** 685 (1942).

[80]G. K. Wehner, Appl. Phys. Lett. **43,** 366 (1983).

[81]K. A. Grossklaus and J. M. Millunchick, Nanotechnology **22,** 7 (2011).

[82]S. Le Roy, E. Sondergard, I. S. Nerbo, M. Kildemo, and M. Plapp, Phys. Rev. B **81,** 4 (2010).

[83]H. Gnaser, Pure Appl. Chem. **83,** 2003 (2011).

[84]I. S. Nerbo, S. Le Roy, M. Foldyna, E. Sondergard, and M. Kildemo, Opt. Express **19,** 12551 (2011).

[85]A. G. Perez-Bergquist, K. Li, Y. W. Zhang, and L. M. Wang, Nanotechnology **21,** 6 (2010).

[86]H. H. Chen, O. A. Urquidez, S. Ichim, L. H. Rodriguez, M. P. Brenner, and M. J. Aziz, Science **310,** 294 (2005).

CHAPTER 2

Experimental Procedures

2.1 Overview

This chapter describes the experimental procedures used for the synthesis and characterization of focused ion beam (FIB) irradiation-induced nanostructures, including droplets/islands, nanorods (NRs) and ripples, and the overgrowth of GaAs films on Ga droplet. For these experiments, undoped semi-insulating GaAs (001) substrates, InSb (001) substrates, 0.55um InSb films grown on GaAs (001) substrates, and p-type InSb (001) substrates were irradiated with Ga^+ FIB.[1,2] In addition, real-time imaging of FIB irradiation-induced Ga droplet formation and motion on GaAs surfaces was achieved via the collection of ion-induced secondary electrons using the secondary electron detector. All the post-irradiation overgrowths were carried out in the Goldman Group Varian modified GEN II molecular beam epitaxy (MBE) system. Following irradiation or post-irradiation overgrowth, surface morphologies were examined using Nomarski microscopy, scanning electron microscopy (SEM), and atomic force microscopy (AFM).

The structure and composition of droplets, islands, and nanorods were examined using transmission electron microscopy (TEM) and x-ray energy dispersive spectroscopy (XEDS). To examine the influence of droplets on the optical emission efficiency, photoluminescence spectra were collected from both irradiated and post-irradiation overgrown samples. Finally, the electrical properties of NRs were investigated using STM-based I-V measurements in the JEOL 2010F TEM.

2.2 Focused ion beam irradiation

All FIB irradiation described in this thesis was carried out in a FEI NOVA 200 dual beam workstation shown schematically in Fig. 2.1 (a),[3] which consists of an ion beam column, and electron beam column, an energy dispersive x-ray (EDX), and secondary electron detectors, enclosed in a high vacuum chamber with 10^{-5} torr base pressure. This system combines a high-resolution secondary electron microscope and a Ga^+ FIB for nanoscale irradiation, patterning, and characterization. For FIB, 5-30 keV ion energies with minimum beam diameters ranging from 7 nm to 78.8nm, were utilized. During FIB irradiation, surface imaging and x-ray microanalysis is achieved via the collection of ion-induced secondary electrons and characteristic x-rays, respectively.[4]

All samples were irradiated at room temperature with ion fluences ranging from 1×10^{15} to 5×10^{18} ions/cm^2. The FIB voltage, current, dwell time, dose rate, and ion fluence used in this work is listed in the Table 2.1.

Table 2.1: FIB ion energy, ion current, dwell time, ion fluence, ion dose rate, magnification, and irradiation time(s) used in this work.

Ion Energy (keV)	Ion current (pA)	dwell time (∝s)	Ion fluence (ions/cm^2)	Ion dose rate (dose/sec)	Magnification (×)	Irradiation time (s)
30	50	0.3-100	1×10^{15}-	5.1×10^{3}	20K	7-300

			5×10^{18}			
30	100	0.3-100	1×10^{15}-	2.1×10^{5}	20K	7-300
			5×10^{18}			
10	50	0.3-20	1×10^{15}-	3×10^{4}	8K-20K	7-300
			5×10^{18}			
5	70	0.3	1×10^{15}-		8K	7-300
			5×10^{18}			

FIB irradiation was carried out at several angles of ion-beam incidence (θ_i), as shown in the schematics of the orientation of electron beams (dashed line) and ion beams (dotted line) with respect to the sample surface, shown in Figs. 2.1 (b). Various values of θ_i were used for the fabrication of Ga droplets, InSb ripples and nanorods, droplet motion, hexagonal arrays of Ga droplets, and several angles of electron-beam incidence (θ_e) were used for top (side) view SEM images respectively. The values of θ_i and θ_e used in each experiment are listed in the Table 2.2. We note the angle between the ion and electron beam column is fixed at 52°.

All FIB irradiation was carried using the raster scan scheme shown in Fig. 2.2, with pitch, p, ranging from 4 to 17 nm, beam spot size ranging from 19 and 23 nm, and beam spot overlap, 0, ranging from 10 to 80 %. In this thesis work, single-side polished (001) undoped Si, GaAs, InAs, InSb substrates, 0.55 ∝m InSb films grown on (100) undoped GaAs substrates, and p-type InSb substrates were cleaved into approximately 5 x 8 mm rectangles and mounted on the FIB holder with the polished side up.

Table 2.2: Values of θ_i and θ_e used for various experiments.

θ_i (^{o})	θ_e (^{o})	**Experiment**
0	0*, 52	Fabrication of Ga droplets, InSb ripples, and InSb nanorods on substrates
52	0*	Fabrication of Hexagonal arrays of Ga droplets on substrates
0	0*, 52	Fabrication of Ga droplets on XTEM samples
20	32	Movies of Ga droplet motion
31	83	Movies of Ga droplet contact angles

*sample stage rotated prior to secondary electron imaging

2.3 Scanning Electron Microscopy

Both plan-view and side-view scanning electron microscopy (SEM) were used to image the surfaces following irradiation and post-irradiation overgrowth. Typical SEM imaging conditions involved 5 keV electrons with a beam current of 90 pA. For Ga droplets and InSb ripples formed on (001)-oriented substrates, SEM images were collected both in the FIB irradiation position ($\theta_i = 0^\circ$ and $\theta_e = 52^\circ$), and at $\theta_e = 0^\circ$, which requires a sample stage rotation following FIB irradiation. For XTEM sample fabrication, SEM images were collected both in the FIB irradiation position ($\theta_i = 0^\circ$ and $\theta_e = 52^\circ$), and at $\theta_e = 0^\circ$, which requires a sample stage rotation following FIB irradiation. In addition, ion-induced secondary electron imaging was used to simultaneously irradiate and image Ga droplet formation and motion. To examine Ga droplet motion, movies were collected with $\theta_i = 20^\circ$ and $\theta_e = 32^\circ$, although the electron-beam was switched off at the time. Furthermore, to image Ga droplet contact angles during motion, movies were collected with $\theta_i = 31^\circ$ and $\theta_e = 83^\circ$, again with the electron-beam switched off. Since

SEM has a limited lateral resolution (the resolution limit is about 10 nm), and does not provide quantitative height information, we also used AFM to quantify the surface morphology.

2.4 Molecular Beam Epitaxy

Molecular Beam Epitaxy was performed in the Modified Varian Gen II chamber in the Goldman Group, shown schematically in Fig. 2.3, which consists of a separately pumped growth chamber, buffer chamber, and load-lock, which are connected by magnetic transfer rods and trolleys. At the time of the growths performed in this thesis, the growth chamber source flange housed 7 solid sources (In, Ga, Al, Si, Be, GaTe and As cracker), as well as an rf plasma source for the production of active N from an ultrahigh purity N_2 gas. We note that GaTe was removed and replaced with Bi on June 17th 2010, and the growth chamber source flange currently housed 7 solid sources (In, Ga, Al, Si, Be, Bi and As cracker) and the rf N_2 plasma source.

For overgrowth, all films were grown on “epi-ready” GaAs substrates which had been irradiated with FIB to produce surface Ga droplet arrays. All samples were indium-mounted on heated molybdenum blocks ($T > 150$°C), and pre-baked at 150°C for 8 hours in the load-lock. In the growth chamber, the substrate temperature was continuously raised to the growth temperature without As overpressure.

Substrate temperatures (T_{sub}) were determined using a spring-loaded thermocouple in direct contact with the backside of the molybdenum block, and calibrated based on the difference between the T_{CAR} and T_{sub}. To calibrate the

temperature of each sample, the oxide desorption temperature was used as a reference point for 580 ºC and the thermocouple reading was linearly offset accordingly. The oxide desorption temperature was determined as the temperature at which the RHEED pattern transformed from a diffuse to a streaky 2x4 pattern. The oxide desorption temperature was used as a temperature reference since it depends primarily on the surface temperature and does not rely on the quality of contact between the thermocouple and the block.

2.5 Atomic Force Microscopy

Atomic force microscopy (AFM) was used to quantify the surface topography following irradiation and post-irradiation overgrowth. Tapping-mode AFM was performed using both a Digital Instruments Nanoscope III AFM and the Veeco Dimension Icon AFM. In tapping-mode, the cantilever is driven to oscillate at a constant frequency near its resonance frequency and brought into intermittent contact with a sample surface. We note that this constant frequency depends on the condition of scanning probe and is not the same for all AFM experiments. When the AFM probe interacts with a surface feature, its oscillation amplitude is decreased. The AFM senses this decrease, and the probe is moved away from the surface to enable the previous amplitude of oscillation. In this way, the tip can be rastered across the sample to generate topographical images. Depending on the size of the scanned areas, two types of AFM probes were used. Etched silicon Micromesh AFM probes with tip radius ~ 10 nm, tip length = 20 - 25 ∝m, resonance frequency = 160 kHz, and force constant ~6 N/m were used for large area (10×10 ∝m^2, 5×5 ∝m^2, 3×3 ∝m^2 and 1×1 ∝m^2) imaging.[5] On the other

hand, ultra-sharp Nanoworld AFM probes with tip radius < 10 nm, tip length = 14 ∝m, resonant frequency = 300 kHz, and force constant 40 N/m were used for small area (400×400 nm^2) imaging.[6] The piezoelectric scanner typically moves the probe in a curved motion over the surface, resulting in a "bowing" in the AFM image. Thus, all AFM topographic images were flattened by subtracting a quadratic background in the x and y directions using Scanning Probe Image Processor (SPIP) software.[7] A variety of other AFM image analysis functions were also performed using the SPIP software, including "profiling", "roughness", and the "Isotropic Area Power Spectral Density (APSD)" function. The APSD function was used to determine periodicities within the AFM images, such as the surface roughness wavelengths.[8] The SPIP software was also used to perform "Advance Fast Fourier Transform (FFT)" analyses of TEM images. Advanced FFT was used to analyze the lateral and vertical periodicity within TEM images, to determine periodicity and ordering of surface features.

2.6 Transmission Electron Microscopy

To investigate the microstructure and composition of the ion-sputtering induced-surface features, we used several TEM-based techniques. For this purpose, specially prepared FIB substrates that enable both FIB irradiation and TEM, as shown in Fig. 2.4, were prepared *prior* to FIB induced nanostructure formation. The substrates were cleaved and polished to 5 ∝m thickness using 600, 800 and 1200 grit SiC papers (corresponding to 16, 12, 8 ∝m particle sizes). The thinned FIB substrates were then mounted on a 3 mm diameter slotted Mo grid/half grid using M-bond 600 followed by

annealing at 100 □C for 30 min on a hot plate, and ion milled to-100 nm using a Gatan Model 691 Precision Ion Polishing System (PIPS) operating at 77K. Finally, the FIB substrate on its TEM grid was transferred to the FIB workstation. Normal-incidence FIB irradiation of the FIB substrates was carried out using 30 keV Ga^+ ions and 50-100 pA currents. TEM imaging and electron diffraction were carried out in a JEOL 2010F operating at 200 kV and a JEOL 3011UHR operating at 300 kV. Bright field and high-resolution TEM (HRTEM) imaging were used to study the crystallographic structure of the irradiated materials at the atomic scale. In addition, selective area electron diffraction (SAED) was used to determine the phase and crystallinity of irradiated materials.

2.7 X-Ray Energy Dispersive Spectroscopy

The surface chemical compositions of ion beam-induced nanostructures were examined by X-Ray Energy Dispersive Spectroscopy (EDS) in the FEI NOVA 200 workstation and/or the JEOL 2010F TEM.[9] For EDS in the JEOL 2010F TEM (FEI NOVA 200), FIB substrates (bulk samples) were used. Since the volume fraction of FIB-irradiation-induced features is higher in the FIB substrates than that in the bulk samples, the signal to noise ratio is lower in the EDS of JEOL 2010F TEM than that of FEI NOVA 200. Data analysis was performed as described in Page 40 of Dr. Wood's thesis.[10] To quantify the depth-dependence of the chemical composition, we assume a uniform sample thickness. For each element, the atomic percentages, C_A and C_B, are related to the measured intensities of characteristic x-rays, I_A and I_B, via the Cliff-Lorimer equation:

$$\frac{C_A}{C_B} = k_{AB}\frac{I_A}{I_B} \tag{2.5}$$

where k_{AB} is the Cliff-Lorimer factor. To determine, k_{AB}, we use XEDS data collected from a region of prisitine GaAs within the same specimen, for both TEM and SEM studies. The measured ratio, I_A/I_B, within the regions of interest, are then used to determine the relative atomic percentages of each element, C_A and C_B.

2.8 Photoluminescence spectroscopy

To determine the optical emission efficiency of GaAs cap layer/Ga droplets/GaAs and GaAs cap layer/GaAs structures, micro photoluminescence (PL) spectra were collected with a 633 nm (1.96 eV) HeNe laser equipped with liquid helium cooled stages. The PL measurements were performed at 10 K by Ms. Jieun Lee in Prof. V. Sih's group in the Physics Department at the University of Michigan. Typical excitation parameters were as follows: 9 ∝W, 0.1 mW and 0.125 mW excitation at a wavelength of 633 nm, focused to a 5 ∝m spot. The data collected to date need to be normalized with respect to the reflected PL power, as described in Section 6.2.

2.9 STM-based IV measurements in the TEM

The electrical transport properties of InSb nanorods (NRs) were determined using an STM-based I-V measurement carried out in the JEOL 2010F at the Michigan Electron Microbeam Analysis Laboratory (EMAL). The measurements were performed by Mr. Jacob R. Jokisaari in Prof. Pan's group in the Materials Science and Engineering Department at the University of Michigan.[11] The FIB-irradiation InSb samples, prepared

as described in Section 2.6, were attached to a Mo TEM grid with carbon paint and inserted into the TEM chamber. BF TEM imaging was used to locate the NR; subsequently, the tungsten STM probe tip was moved toward the NR until the NR appears bent, in the TEM image. The I-V measurement was performed in contact mode, using bias voltages ranging from -3V to 3V with 1000 data points, each acquired in 0.1 μs.

2.10 References and Figures

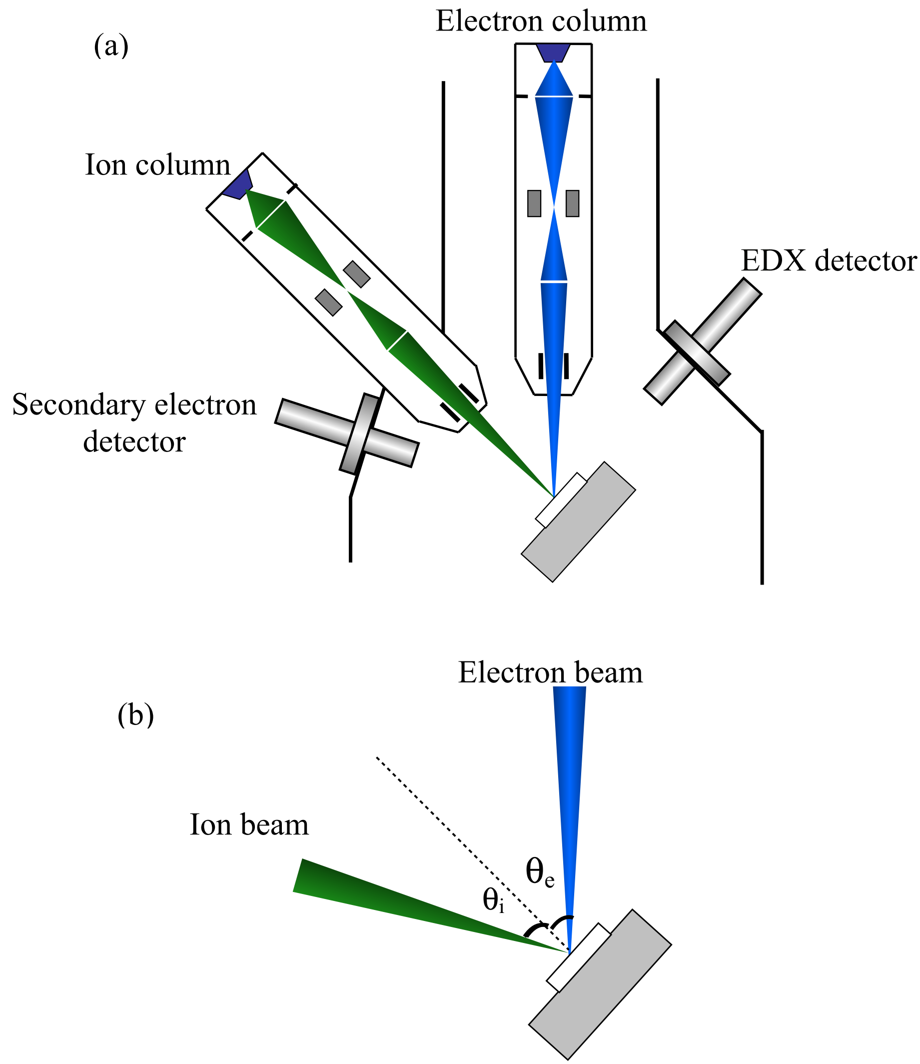

Figure 2.1 (a) Schematic of NOVA 200 dual beam workstation, and (b) schematic of relative orientations of the electron beam, the ion beam, and the sample surface normal (dashed line). The electron beam angle of incidence, θ_e is defined as the angle between the incident electron beam and the sample surface normal. The ion beam angle of incidence, θ_I, is defined as the angle between the incident ion beam and the sample surface normal. The angle between the ion and electron beam columns

is fixed at 52. Therefore, to achieve normal-incidence FIB irradiation, $\theta_I=0$, the sample must be tilted to 52 with respect to the electron beam. The angle between the electron beam column and secondary electron detector is 90.

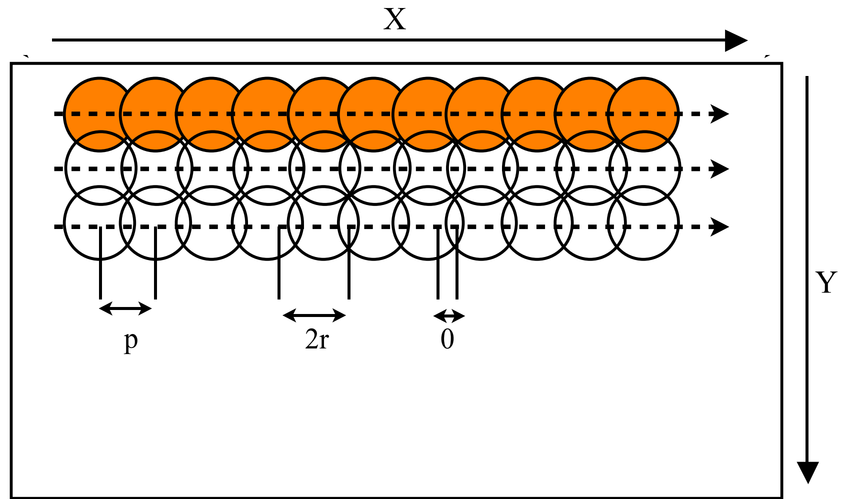

Figure 2.2 Schematic of FIB raster scanning, which consists of motion of the FIB beam in the positive X direction, followed by moving down one pitch in the positive Y direction. FIB irradiation was carried out with Pitch (p) ranging from 4 to17 nm, beam diameter (2r) ranging from 19 to 23 nm, and beam spot overlap ranging from 10 to 80 %.

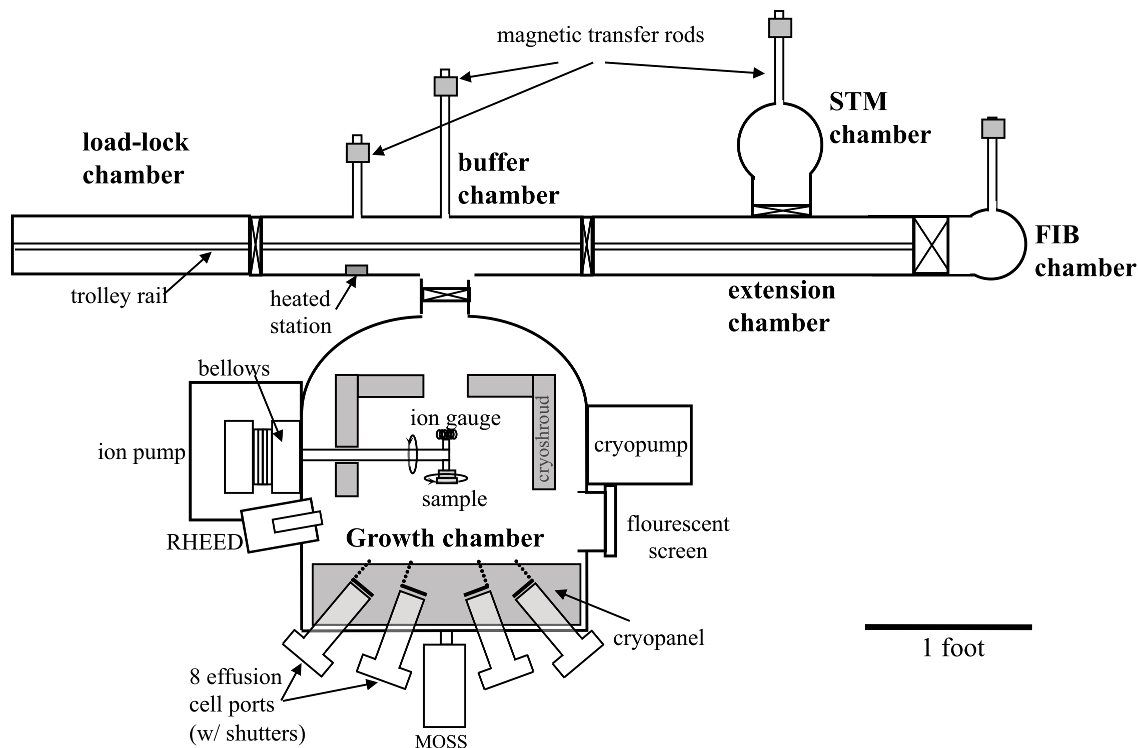

Figure 2.3 Schematic of the Modified Varian Gen II molecular-beam epitaxy system used in these studies. The rf N_2 plasma source is located on one of the effusion cell ports, along with a residual gas analyzer, and seven solid sources (Ga, In, Al, Be, Si, Bi, and As cracker). Reprinted figure with permission from YuJin, PhD thesis, University of Michigan, Ch.2, 2010.

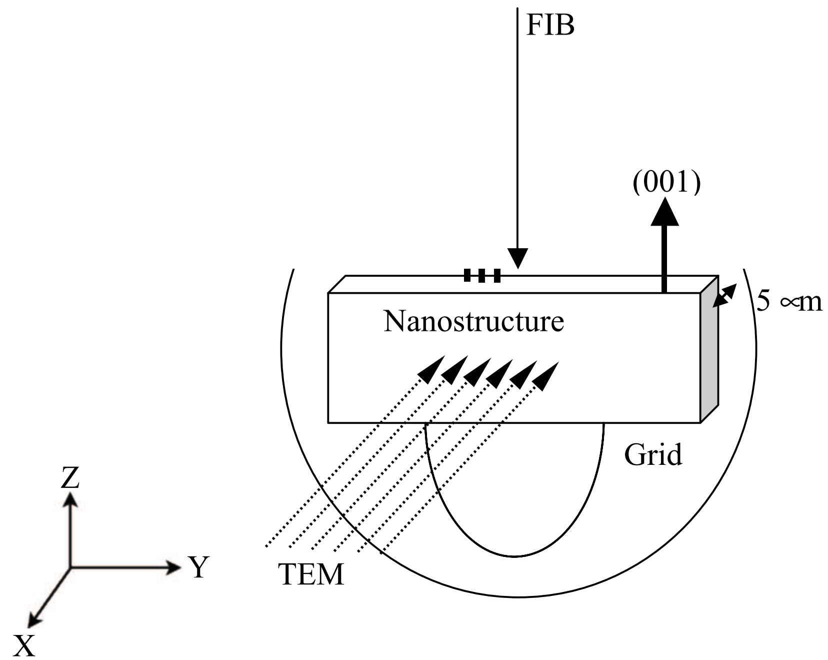

Figure 2.4 Schematic of the FIB substrate mounted on a TEM grid for nanostructure fabrication via FIB followed by TEM analysis. Ga+ FIB irradiation is in –Z direction. The electron beam for TEM is in +X direction.

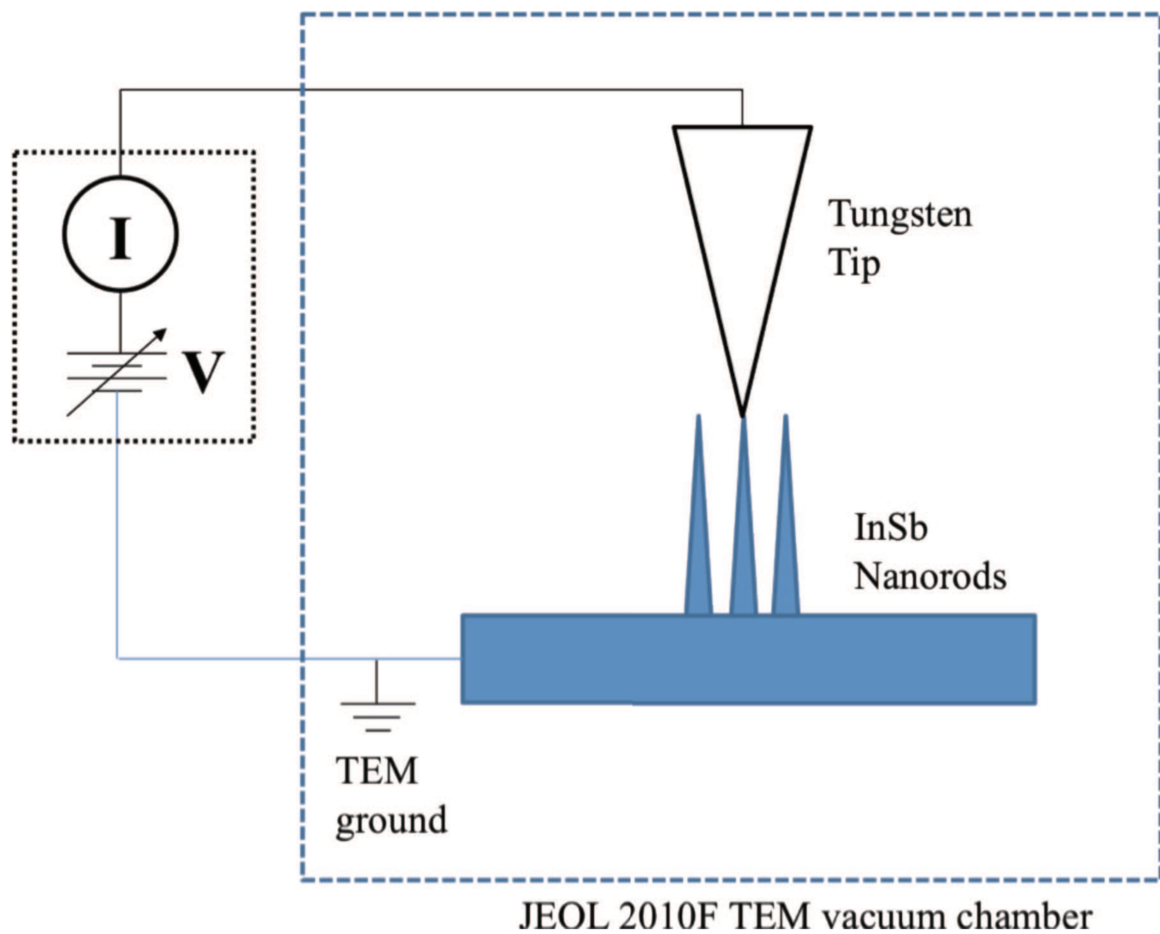

Figure 2.5 Schematic of the circuit diagram of the STM-based I-V measurement system.

[1]X. Weng, N. G. Rudawski, P. T. Wang, R. S. Goldman, D. L. Partin, and J. Heremans, J. Appl. Phys. **97** (2005).

[2]http://www.nanoworld.com.

[3]J. Gierak, Semicond. Sci. Tech. **24** (2009).

[4]T. Freeman, S. Kellogg, D. Laur, M. Maazouz, and N. Martin, *UHV Magnum Ion Column with BDS-200 User's Guide* (FEI Company, 2006).

[5]http://www.spmtips.com.

[6]CORE, Profile Code.

[7]*The Scanning Probe Image Processor,User's and Reference Guide* (1998).

[8]S. Karan and B. Mallik, Phys. Chem. Chem. Phys. **10,** 6751 (2008).

[9]S. J, *Optical Scattering: Measurement and Analysis 2nd edn* (Bellingham, WA: SPIE Optical Engineering Press, 1995).

[10]A. W. Wood, Thesis, University of Michigan, 2012.

[11]C. T. Nelson, Thesis, University of Michigan, 2011.

CHAPTER 3

Formation, Coarsening, and Motion of Ga Droplets

3.1 Overview

The chapter opens with background information, including a review of early studies of Ga droplet formation and motion on III-V surfaces. Next, the experiments used to fabricate, characterize, and track Ga droplets are described. The remainder of the chapter has 3 main foci. First, we present a comparison of droplet formation and growth on patterned and unpatterned surfaces. Next, we identify the steady-state regime for droplet motion and examine the relative roles of driving forces induced by FIB scanning and thermal gradients on droplet motion. Finally, we describe the analysis of the droplet composition and crystallinity. The chapter concludes with a summary.

3.2 Background

3.2.1 Droplet formation on III-V surfaces

The formation of submicron diameter metallic droplets on III-V compound semiconductor surfaces has been observed under a number of experimental conditions in which the surface is group III rich.[1-7] These metallic droplets are promising for a wide range of applications such as droplet epitaxy,[1,8] nanowire growth,[9,10] and negative index of refraction materials.[11,12] In the case of GaAs, Ga droplets have been observed following heating in a vacuum,[2] exposure to a Ga molecular beam in the absence of As,[3] and irradiation with either broad-area ions[4] or FIB.[5-7,13] In all cases, arsenic is preferentially desorbed or sputtered due to its lower binding or sublimation energy in comparison with that of Ga.[14] Surface morphologies similar to those of droplets have been observed following Cs^+ and Ar^+ irradiation of GaAs.[4,15,16] Similar features have been observed following FIB irradiation of GaAs,[5,6] and recently, attempts to fabricate ordered arrays of Ga droplets on GaAs surfaces have been reported using both normal[7] and off-normal incidence FIB.[13]

For both broad-area and FIB irradiation of GaAs, the composition and crystallinity in the vicinity of the droplet and surrounding region were unknown prior to this thesis work. Yet, a droplet formation mechanism based upon preferential As sputtering followed by ion-enhanced Ga surface diffusion has been proposed.[4,7] Since the Ga droplets in previous work were fabricated by continuous irradiation, the processes of droplet nucleation, growth, and motion occurred concurrently.[7,17]

3.2.2 Droplet motion on III-V surfaces

Self-propelled motion of Ga droplets has been reported for GaAs and GaP substrates heated in high vacuum.[18,19] Such observations provide opportunities to study the formation and motion of droplets, and more importantly to form ordered arrays of nanodots and nanowires.[20] To date, the driving force for the droplet motion on heated substrates has been attributed to the imbalance between droplet surface energies and droplet/substrate interfacial energies.[18,19] However, droplet motion during irradiation has not been reported, nor have its mechanisms been discussed.

3.3 Experimental Details

All samples were prepared on semi-insulating GaAs surfaces using an FEI Nova 200 Nanolab dual-beam FIB system, with the incident ion beam perpendicular to the sample surface. In each experiment, 10-30 kV Ga ions were delivered to the GaAs surface in a continuous raster scan mode. The threshold ion dose for droplet formation, determined by in-situ SEM and ex-situ AFM, was $2.3 \pm 0.6 \times 10^{16}$ cm^{-2} for 10 kV - 30 kV Ga ions, consistent with literature reports.[5,7] To separately examine the nucleation and growth of the droplets, we introduced heterogeneous nucleation sources via a 6×6 square surface array of nanoholes (over an area of 7.6×6.6 ∝m^2, with 10-80 nm depth, 300-1000 nm diameter, and 1500-4000 nm spacings) and tuned the effective diffusion lengths via time-delays between successive scans. Typically, to prevent the formation of droplets during the hole patterning process, ion fluences less than $\sim 5 \times 10^{15}$ cm^{-2} were utilized. Following patterning, FIB irradiation over an area of 12×10 ∝m^2 (symmetrically overlapping the nanohole array) was performed using 10 or 30 kV Ga ions, with 50 pA

ion beam currents. Post-patterning irradiation was performed continuously up to a moderate dose (~1×10^{16} cm^{-2}), followed by 2D scans with 2-minute interruption between each scan, up to the final dose.

The FIB-irradiated surfaces were imaged immediately following irradiation (52° angle of incidence) and ~5 minutes following irradiation (normal angle of incidence) using scanning electron microscopy (SEM). We refer to these images as "immediate" and "5 minute" SEM images, respectively. In addition, real-time imaging was used to record droplet formation and motion by collecting the secondary electrons generated by the ion beam. To quantify contact angles of droplets in motion, side-view SEM imaging was performed with electron beam incidence near 90° (~83°). Since the angle between the ion and electron beam columns is fixed at 52°, irradiation was performed using ~ 31° of ion beam incidence, as shown in Fig. 2.1 (e). To track droplet motion, we used a code developed in the interactive data language (IDL) to quantitatively analyze the instantaneous positions, sizes, and velocities of the droplets in each video frame, as discussed in Appendix E.

The structure and local Ga atomic fraction (f_{Ga}) in and within the vicinity of the droplets were determined using ex-situ transmission electron microscopy (TEM), and x-ray energy dispersive spectroscopy (XEDS) in the TEM. For cross-sectional TEM studies, droplets were synthesized directly by FIB irradiation of GaAs thin foils, which had been prepared by mechanical polishing and Ar ion milling at 77 K. TEM imaging and electron diffraction were carried out in a JEOL 2010F (3011) operating at 200 kV (300 kV). XEDS maps were collected using scanning TEM in the JEOL 2010F. For

these ion and electron energies, beam-induced sample heating is expected to be insignificant.[21]

3.4 Droplet formation and growth

3.4.1 Identifying the steady-state

To examine droplet formation and coarsening on FIB-irradiated GaAs surfaces, we first identify the ion fluence regime where the surface [Ga], C(t), has reached a steady-state. As described in Appendix C, C(t) consists of the sum of the implanted [Ga], $C_{impl}(t)$, plus [Ga] due to preferential sputtering of arsenic, the so-called "left behind" [Ga], $C_{LB}(t)$. Thus, we consider that C(t) has reached a steady-state when the milled depth of GaAs exceeds the projected ion range, R_p. To determine the ion fluence dependence of GaAs sputtering, we used atomic force microscopy to examine the milled depth vs. ion dose for both 10 and 30 kV Ga^+ ions, as shown in Fig. 3.

For comparison, Fig. 3.2 shows SRIM simulations of the concentration of implanted ions as a function of depth, with the depth of the maximum likelihood concentration identified as the projected ion range, R_p. The calculated R_p is ~8 nm (~15nm) for 10 kV (30 kV) Ga^+ ions. As shown in Fig. 3.1, for ion fluences of 3.4±0.1 $\times 10^{16}$ cm^{-2}, the sputtered depth is 9.0±3.2 nm (15.7±11.3 nm) for 10 kV (30 kV) ions, greater than R_p for both 10 and 30 kV ions, suggesting that the steady-state has been reached.[22] It is interesting to note that a constant droplet size was reported for irradiation of GaAs with Ga+dose >10^{16} cm^{-2}, consistent with attainment of steady-state for doses beyond 3.4±0.1 $\times 10^{16}$ cm^{-2}.[23]

3.4.2 Unpatterned surfaces: classical nucleation

To consider droplet formation in the context of nucleation theory described in Appendix B, we discuss the ion energy dependence of droplet growth rate and size distribution following irradiation. Figure 3.3 shows immediate (Figs. 3.3 (a) and 3.3 (b)) and 5 minute (Figs. 3.3 (c) and 3.3 (d)) SEM images of surfaces irradiated using 30 kV and 10 kV ions, with corresponding size distribution plots in Figs. 3.3 (e)-(h). Interestingly, for both ion energies, the average droplet radius, <r>, for 5 minute SEM images is larger than those for immediate SEM images, suggesting that droplet growth continues beyond the cessation of irradiation. For immediate SEM images, as shown in Figs. 3.3 (e)- 3.3 (f), a log-normal size distribution is apparent, suggesting droplet growth is dominated by dynamic coalescence, independent of ion energy.[24] For 5 minute SEM images, a log-normal (Gaussian) size distribution is observed for 30 kV (10 kV) ions. Apparently, for 10 kV ions, there has been a transition to ripening, typically a late-stage growth mechanism.[25] The transition is likely due to the expected lower supersaturation, S (t), for 10 kV in comparison with 30 kV ion irradiated surfaces. We note that the values of S(t) depend on time.

3.4.3 Patterned surfaces: heterogeneous nucleation

To consider heterogenerous nucleation of droplet in the context of nucleation theory as described in Appendix B, we discuss the ion energy dependence of the growth rate of droplets formed on nanohole arrays. Figures 3.4 (a)-(b), (c)-(d) show immediate SEM images of patterned surfaces irradiated using 30 kV (Figs. 3.4 (a) and (b)) and 10 kV (Figs. 3.4 (c) and (d)) ions. For both irradiation energies, droplets nucleate within the

pre-patterned holes and grow to similar sizes, as shown in Figs. 3.4 (a) and (c). The preferential nucleation within pre-patterned holes is presumably due to the higher C(t) within the holes. As the ion fluence is increased to ~6×10^{16} cm^{-2}, uniform droplet arrays with 1 droplet/hole are evident for both 10 kV and 30 kV ions, as shown in Figs. 3.4 (b) and (d). For 30 kV ion fluences beyond ~2.8×10^{16} cm^{-2}, the droplet sizes remain uniform with 1 droplet/hole, as shown in Fig. 3.4 (b). On the other hand, for similar fluence of 10 kV ions, shown in Fig. 3.4 (d), the droplet size is non-uniform and "interstitial" droplets are apparent. We note that the increased size of the edge droplets in comparison to the inner droplets is presumably due to a lower number of nearest neighbor droplets competing for the capture of diffusing Ga adatoms in that case.

We now consider the fabrication time dependence of the <r> using an analysis approach based upon SEM images, described in Appendix D. Since the edge and non-edge droplets have different numbers of nearest neighbors, we consider (a) all and (b) all but non-edge droplets fabricated on arrays of holes with 10 nm depth, 300nm diameter, and 1500 nm spacing. Figure 3.5 shows plots of <r> versus fabrication time. For 30 kV ions, the number of droplets remains constant with time, and <r> is proportional to $t^{0.5}$ for both cases, suggesting a diffusive growth mechanism, typically found in early-stage growth. For 10 kV ions, for both cases the number of droplets is nearly constant with time, but <r> is instead proportional to $t^{0.3}$, suggesting a transition to ripening, typically a late-stage growth mechanism as discussed in Appendix B.[26] The details of the predicted growth rate of droplets in the early-stage and late-stage growth can be found in Appendix B. This energy dependent transition from early- to late-stage growth is similar to that discussed above for the homogenously nucleated droplets.

3.5 Droplet motion

To examine droplet motion on irradiated GaAs surfaces, we consider droplet motion at steady-state, when both the total number of droplets and the average droplet size are constant. We note that the steady-state is defined by a time rather than a fluence. In this section, we identify the steady-state regime of droplet motion, and consider both FIB scanning and thermal gradients as possible origins of the motion.

3.5.1 Identifying the Steady-State Regime

To identify the steady-state regime, we examine the irradiated surfaces as a function of irradiation time, as shown in the SEM images in Fig. 3.6. For irradiation times < 6 seconds, featureless surfaces are observed as shown in Fig. 3.6 (a). Following 6.2 seconds of irradiation, randomly distributed Ga droplets are observed, as shown in Fig. 3.6 (b). With further irradiation, the droplets rapidly increase in size and number. For example, following 6.6 seconds of irradiation, as shown in Fig. 3.6 (c) the number and the average size of the droplets have increased from 105 and 50 nm to 126 and 73 nm, respectively, although the droplet remain static. As the irradiation time is further increased, the total number of droplets and the average droplet size remain constant, shown in Fig. 3.6 (d) (for 12.4 seconds of irradiation time) and (e) (for 28.6 seconds of irradiation time), but droplet motion has commenced. Figure 3.6 (f) shows the droplet size distribution as a function irradiation time. As the irradiation time is above 7.8 seconds, the size distribution of droplets remains similar.

Figure 3.7 shows the irradiation time dependence of the ratio of total droplet surface areas to the total irradiated area, termed the "droplet surface coverage". Above a critical irradiation time, Ga droplets appeared on the surfaces with < 5% of droplet surface coverage. For irradiation time ranging from 6 to 12 seconds, the droplet surface coverage increases rapidly to ~18 %. As irradiation time is further increased to above 12 seconds, the droplet surface coverage remains constant, consistent with the essentially constant number and size of droplets in Fig. 3.6 (d) and 3.6 (e). In addition, the average number of droplets on these surfaces is about 152±5, larger than the 126, the number of droplets on the surfaces irradiated with time < 6.6 seconds. The steady state droplet surface coverage suggests that the loss of Ga atoms from droplets due to sputtering is compensated by Ga adatoms from the Ga rich layer.

3.5.2 Relative displacements of droplets

For droplet motion in steady-state, we examine the speed and displacement of individual droplets. Figure 3.8 shows a plot of the droplet speed as a function of droplet radius. For droplet radii from 80 to 200 nm, the average speed is 70 ±5 nm/s. Figure 3.9 shows a 2D map of the trajectories of all droplets with respect to their initial positions. The X_+ (Y_-) and X_- (Y_+) represent directions along and opposite to FIB fast (slow) scan directions, as shown in Fig. 3.9 (b). The total number of droplets in each quadrant are indicated in the 2D map in Fig. 3.9 (a). As shown in Fig. 3.9 (b), the ratio of droplets moving opposite vs. along the FIB fast (slow) scan directions are 2.45 (1.22), indicating that droplets prefer to move in a direction opposing the FIB scan direction. These data

suggest that droplet motion is influenced by scanning of the ion beam, possibly due to FIB-induced thermal and/or composition gradients, which will be discussed next.

3.5.3 Origins of Droplet motion

To estimate the thermal and/or composition gradients needed for droplet motion at the measured speeds, we consider FIB-induced gradients within droplets. For this purpose, we measured the contact angles of droplets in motion, using an approach described in Section 3.3. For example, Fig. 3.10 shows a side-view SEM image of a droplet in motion. It is interesting to note that this droplet is asymmetric, with its advancing contact angle, θ_A'larger than its receding contact angle, θ_R'. Next, we calculate and compare the local temperature rise after a one-spot FIB scan, ΔT_{FIB}, with the temperature difference needed for droplet motion at a specific velocity, ΔTv, using the measured θ_A and θ_R for each droplet.

We consider droplet motion resulting from a competition between the frictional force preventing liquid Ga from sliding past the GaAs surface (the viscous force) and thermal gradient induced driving force (the mechanical force). The viscous force, F_V, is defined as[27]

$$F_v = \int_{-R}^{R} 3\square \frac{V}{\zeta} dx - \frac{1}{2}\left(\gamma_{Ga,R} - \gamma_{Ga,A}\right) \qquad 3.1$$

where R is the droplet radius, $\propto$ is the viscosity of Ga, V is the droplet speed, and γ_{Ga}, the surface energy of liquid Ga, is defined as 708-0.066 (T-29.8) where T is the temperature.[28] In this calculation, we assume there is ΔTv in between advancing point (A)

and receding point (R) of a droplet, leading to the difference of $\gamma_{Ga,}(T = T_R)$ and $\gamma_{Ga,}\ (T = T_A)$.[28]

The mechanical force, F_m, is defined as[29]

$$\gamma_{Ga}\cos\theta_R - \gamma_{Ga}\cos\theta_A \qquad 3.2$$

where θ_A and θ_R are the advancing contact and receding contact angles, respectively, as shown in the Fig. 3.10. When the droplet motion speed reaches steady-state, $F_m + F_v = 0$ Hence, ΔT_v is approximated as[27]

$$\Delta T_v = \frac{6R\square JU + \gamma_{Ga}(\cos\theta_r - \cos\theta_a)}{\left|\frac{d\gamma}{dT}\right|(\frac{1}{2} + \cos\theta_r)}, \qquad 3.3$$

where R is the droplet radius, and $\propto$ is the viscosity of Ga, and U is the droplet speed, and J is defined as[29]

$$J = \frac{1}{2R}\int_{-R}^{R}\frac{dx}{h(x) + 3b}, \qquad 3.4$$

where h(x) is the surface profile of the droplet, b is the distance between the real interface and the imaginary plane where the extrapolated tangential velocity component vanishes, the so-called Navier slip length. The detailed derivation of ΔT_v can be found in the Appendix F.

As shown in Appendix F, the calculate ΔT_{FIB} (0.295 ^oC) is slightly smaller than ΔT_v (0.30~ 1.7 ^oC), suggesting that FIB-induced thermal gradients are insufficient to drive droplet motion. Thus, further work is needed to examine the influence of FIB-induced composition gradients on droplet motion. For example, the influence of

composition gradients within and between droplets could be considered via simultaneous FIB irradiation and in-situ XEDS.

3.6 Crystallinity and composition of droplets

Figures 3.11 (a) and (b) present a bright-field STEM image and corresponding XEDS map [where red (green) denotes Ga (As)], respectively, for a typical droplet formed by 30 kV FIB. Fig. 3.11 (a) also contains an overlayed plot of f_{Ga} vs. position. The XEDS map and plot of f_{Ga} vs. position in Fig. 3.11 (a) reveal a nearly pure Ga droplet, with f_{Ga} increasing towards the droplet surface. Interestingly, the plot in Fig. 3.11 (a) shows a ~40 nm Ga-rich transition layer between the droplet and substrate, with f_{Ga} ranging from 50% (substrate side) to 80% (droplet side). The high-resolution TEM image in Fig. 3.11 (c) shows that the Ga-rich surface layer contains many lattice fringes with average spacing similar to the {111}[30] interplanar spacings of zincblende (ZB) GaAs. Using selected area diffraction (SAD) apertures to select 0.27 and 0.19 ∝m diameter regions, we probed regions consisting of the transition layer and the combined transition layer plus droplet. The SAD pattern from the combined transition layer plus droplet, shown as an inset to the HRTEM image of Fig. 3.11 (c), reveals three spotty rings associated with {111}, {220}, and {400} of ZB GaAs, and a diffuse ring due to amorphous Ga. The SAD pattern collected from the transition layer also reveals three spotty rings associated with ZB GaAs, but without a diffuse ring (not shown), suggesting the transition layer likely consists of polycrystalline GaAs, while the droplet contains amorphous Ga. Since GaAs is a line compound, a change in its composition, lead to the precipitation of the rich elements. Thus, these data suggest a droplet formation

mechanism that involves Ga precipitation from a Ga-rich surface layer. In addition, there is presumably a composition gradient in the G-rich surface layer, which acts as the driving force for droplet motion.

3.7 Summary and conclusions

In summary, we have separately examined droplet formation and growth mechanisms by introducing nucleation sources and effective diffusion lengths. The data suggest a droplet formation mechanism that involves Ga precipitation from an ion-induced Ga rich surface layer. Continued irradiation induces further nucleation and growth of droplets. Early stage droplet growth is dominated by diffusion and dynamic coarsening. As the C(t) decreases, there is a transition to late stage growth, dominated by ripening and dynamic coalescence.

We also investigated FIB-induced droplet motion on GaAs surfaces. The anisotropic motion and asymmetric droplet shape suggest that droplet motion is driven by FIB-induced composition gradients and/or thermal gradients. The calculated FIB-induced thermal gradients are smaller than the required thermal gradients for droplet motion, suggesting that FIB-induced thermal gradients are insufficient to drive droplet motion. The influence of FIB-induced composition gradients needs to be further considered. For example, the influence of composition gradients within droplets on droplet motion could be considered Using simultaneous FIB irradiation and EDAX mapping. Finally, we investigated the nanoscale crystallinity and composition of Ga droplets. The data showed that there is a polycrystalline GaAs transition layer underneath an amorphous Ga droplet.

3.8 Figures and References

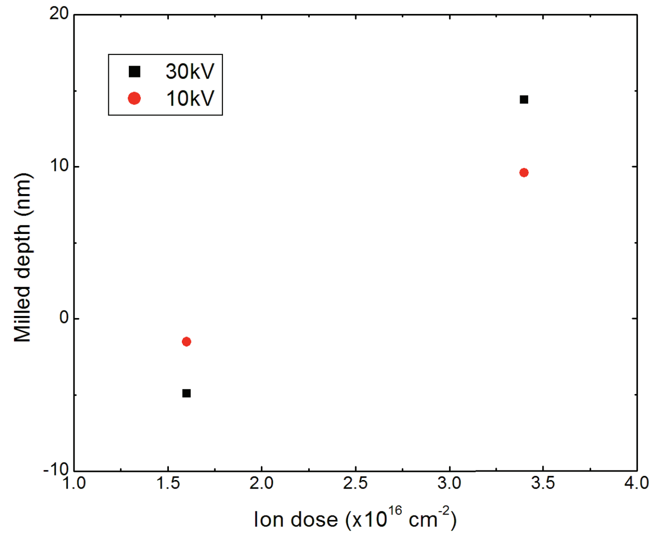

Figure 3.1 GaAs milled depth for both 10 and 30 kV Ga+ ions with doses are 1.6×10^{16} cm^{-2} and 3.4×10^{16} cm^{-2}. The "negative" milled depth for the ion dose of 1.6×10^{16} cm^{-2} is likely due to ion-induced swelling, similar to literature reports.[31]

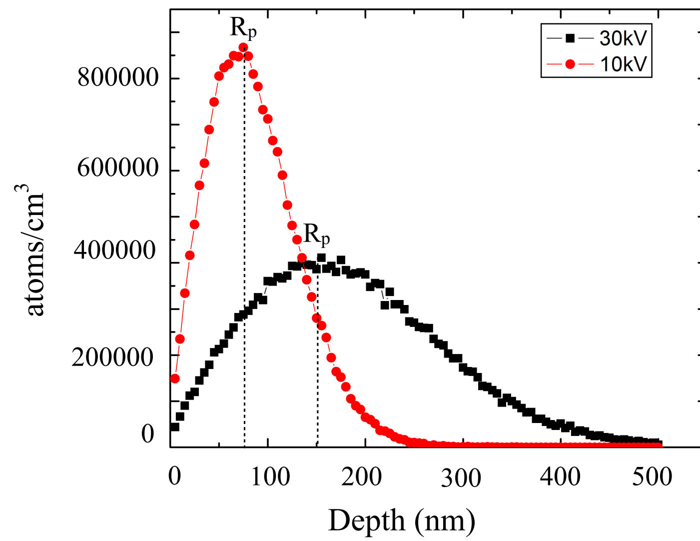

Figure 3.2 SRIM simulations of the implanted ion concentration vs. depth 30 and 10 kV Ga^+ in GaAs. The depth of maximum likelihood ion concentration, the projected ion range, R_p, of 30 kV (10kV) Ga^+ is ~15 nm (~8 nm).

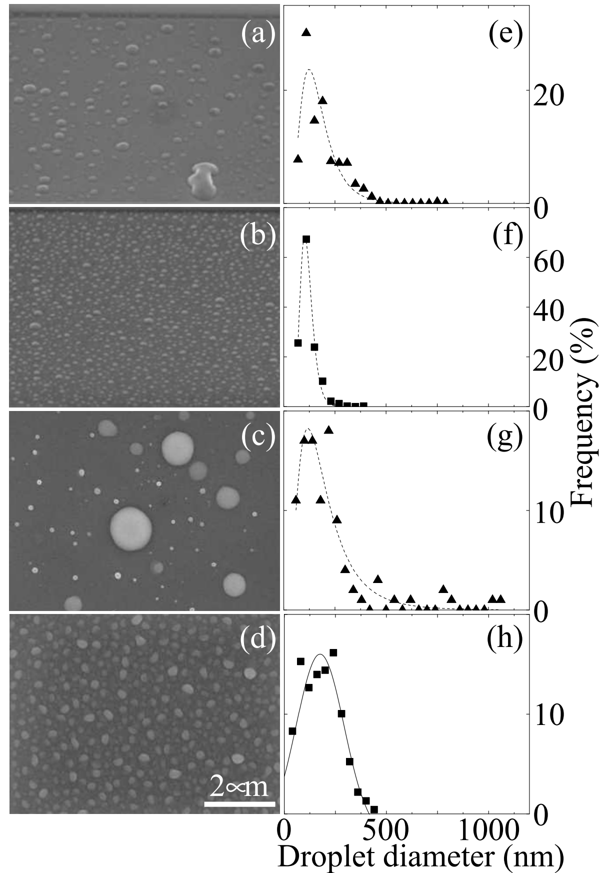

Figure 3.3 SEM images recorded immediately and ~5 min following the cessation of irradiation with energy and dose of (a), (c) 30 kV, 3.8×10^{16} cm^{-2} and (b), (d) 10 kV, 3.8×10^{16} cm^{-2}. Images (a)–(b) [(c) –(d)] were collected with 52° (normal) angle of incidence. The corresponding size distribution from images (a)–(d) are shown in (e)–(h). The frequency is the percentage of droplets with radii within a specified range. Fits to a lognormal distribution (Gaussian) are shown as dashed (solid) lines, with χ values (e) 0.82, (f) 0.99, (g) 0.90, and (h) 0.87. Reprinted figure with permission from J. H. Wu, W. Ye, B. L. Cardozo, D. Saltzman, K. Sun, H. Sun, J. F. Mansfield, and R. S. Goldman, Appl. Phys. Lett. 95, 153107 (2009). Copyright 2009 by American Institute of Physics.

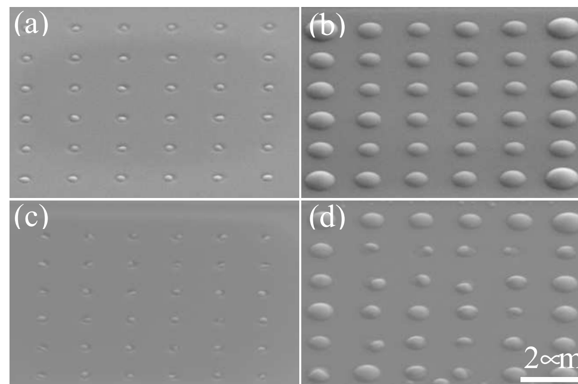

Figure 3.4 SEM images recorded immediately following [(a)–(b)] 30 kV, and [(c)–(d)] 10 kV FIB scanning of a GaAs substrate pre-patterned with an array of holes. The ion fluences are: (a), (c) 2.8×10^{16} cm^{-2} and (b), (d) 6.1×10^{16} cm^{-2}. Reprinted figure with permission from J. H. Wu, W. Ye, B. L. Cardozo, D. Saltzman, K. Sun, H. Sun, J. F. Mansfield, and R. S. Goldman, Appl. Phys. Lett. 95, 153107 (2009). Copyright 2009 by American Institute of Physics.

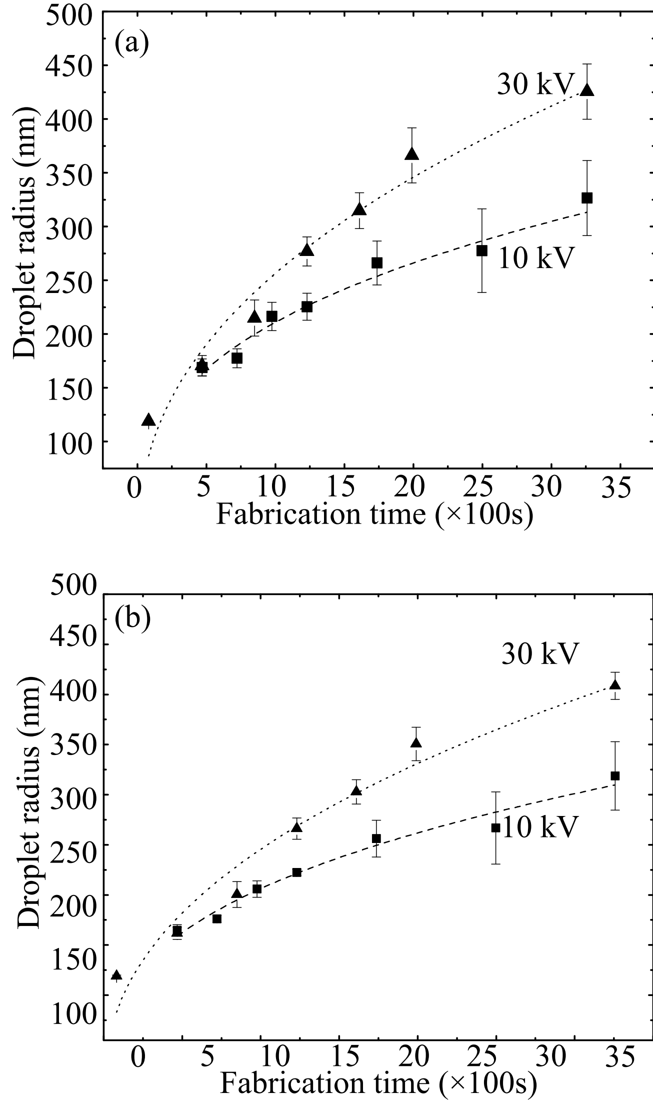

Figure 3.5 Plots of the average droplet radius as a function of fabrication time, which includes both the time of irradiation plus the time-delays between successive scans. (a) includes all droplets in the images. Fits of the 30 kV (10 kV) data to $t^{0.46}$ ($t^{0.3}$) are shown as dotted (dashed) lines, with χ values 0.95 (0.97). Reprinted figure with permission from J. H. Wu, W. Ye, B. L. Cardozo, D. Saltzman, K. Sun, H. Sun, J. F. Mansfield, and R. S. Goldman, Appl. Phys. Lett. 95, 153107 (2009). Copyright 2009 by American Institute of Physics. (b) includes only non-edge droplets in the images. Fits of the 30 kV (10 kV) data to $t^{0.47}$ ($t^{0.3}$) are shown as dotted (dashed) lines, with χ values 0.95 (0.97).

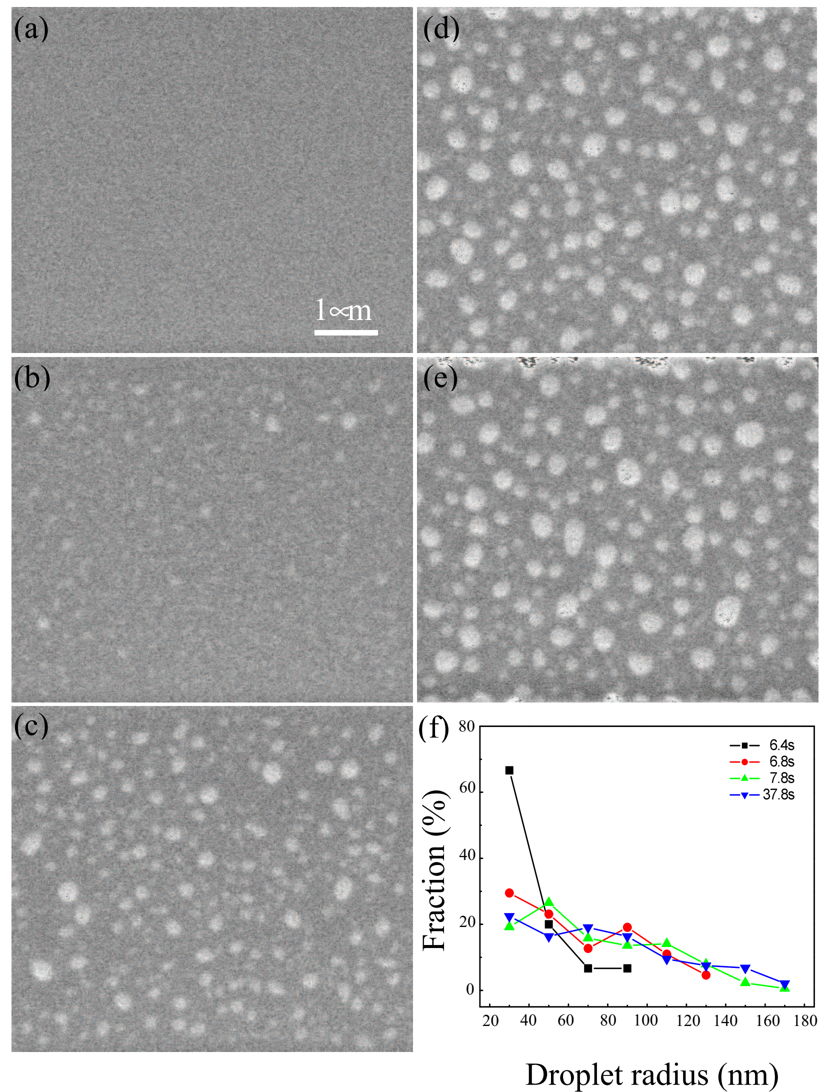

Figure 3.6 SEM images of the instantaneous 30 kV Ga^+ irradiated GaAs surfaces. The irradiation times are: (a) 5.8 s, (b) 6.2 s, (c) 6.6 s, (d) 12.4 s, and (e) 28.6 s. (f) shows the droplet size distribution as a function irradiation time. The irradiation times are: 6.4 seconds (black), 6.8 seconds (red), 7.8 seconds (green), and 37.8 seconds (blue).

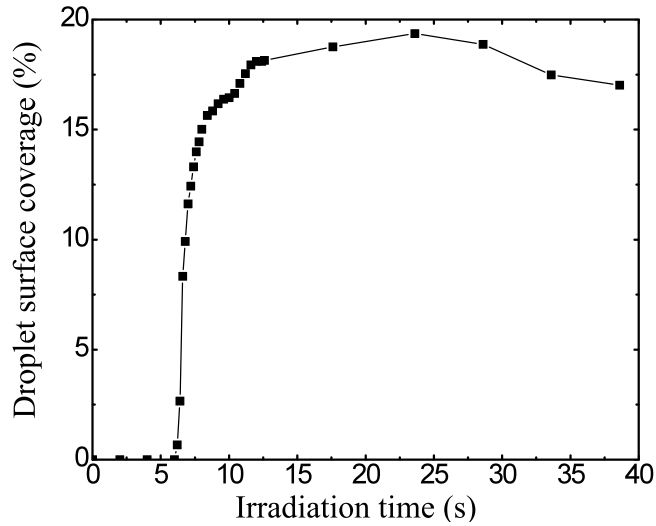

Figure 3.7 Droplet surface coverage as a function of irradiation time for 30 kV Ga^+ irradiated GaAs surfaces. The droplet surface coverage is determined as the ratio of total droplet surface areas to total irradiated area. We assumed that the shape of droplets is circular and used the radius of the droplet determined from the IDL code to calculate the total droplet surface. The details of the droplet radius analysis are included in Appendix D.

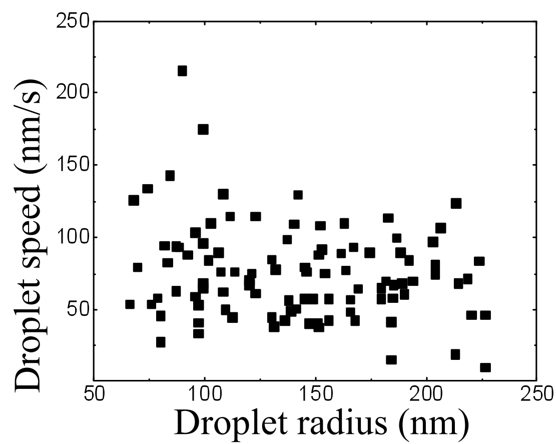

Figure 3.8 Droplet speed as a function of droplet radius for 30 kV Ga+ irradiated GaAs surfaces. The average droplet speed is 70±5 nm/s, essentially independent of droplet radius.

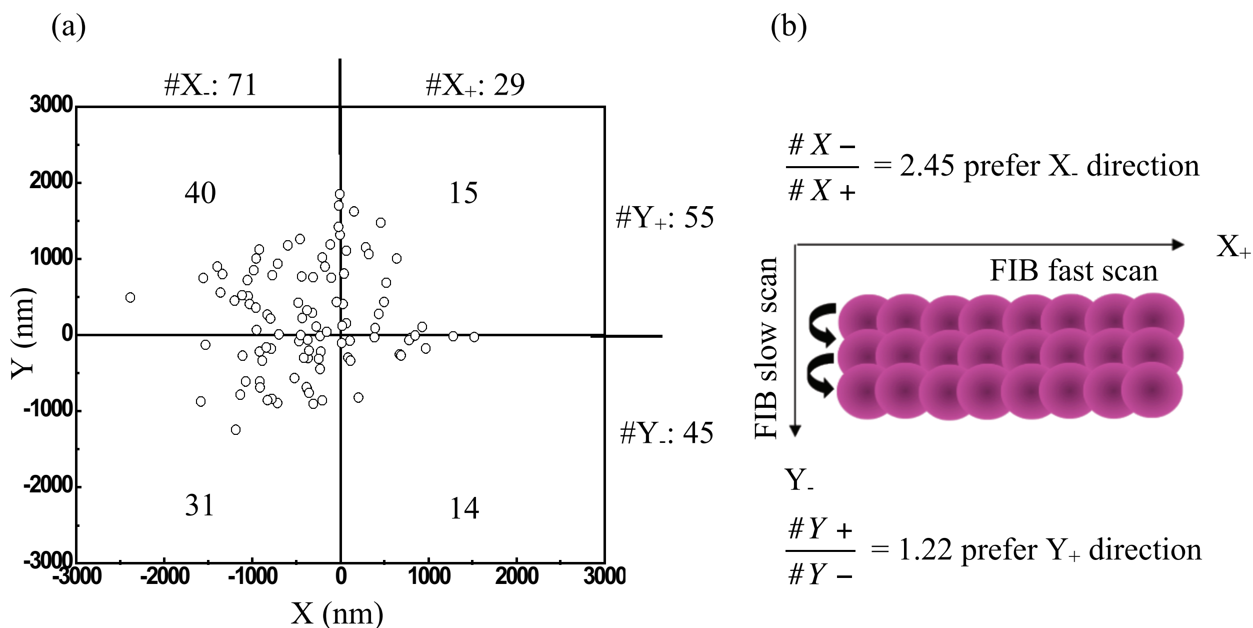

Figure 3.9 (a) 2D mapping of trajectories of all droplets with respect to their initial positions. The X+ (Y-) and X- (Y+) represent directions along and opposite to the FIB fast (slow) scan direction, as shown in (b). The total numbers of droplets with trajectories in each quadrant are indicated in the 2D map.

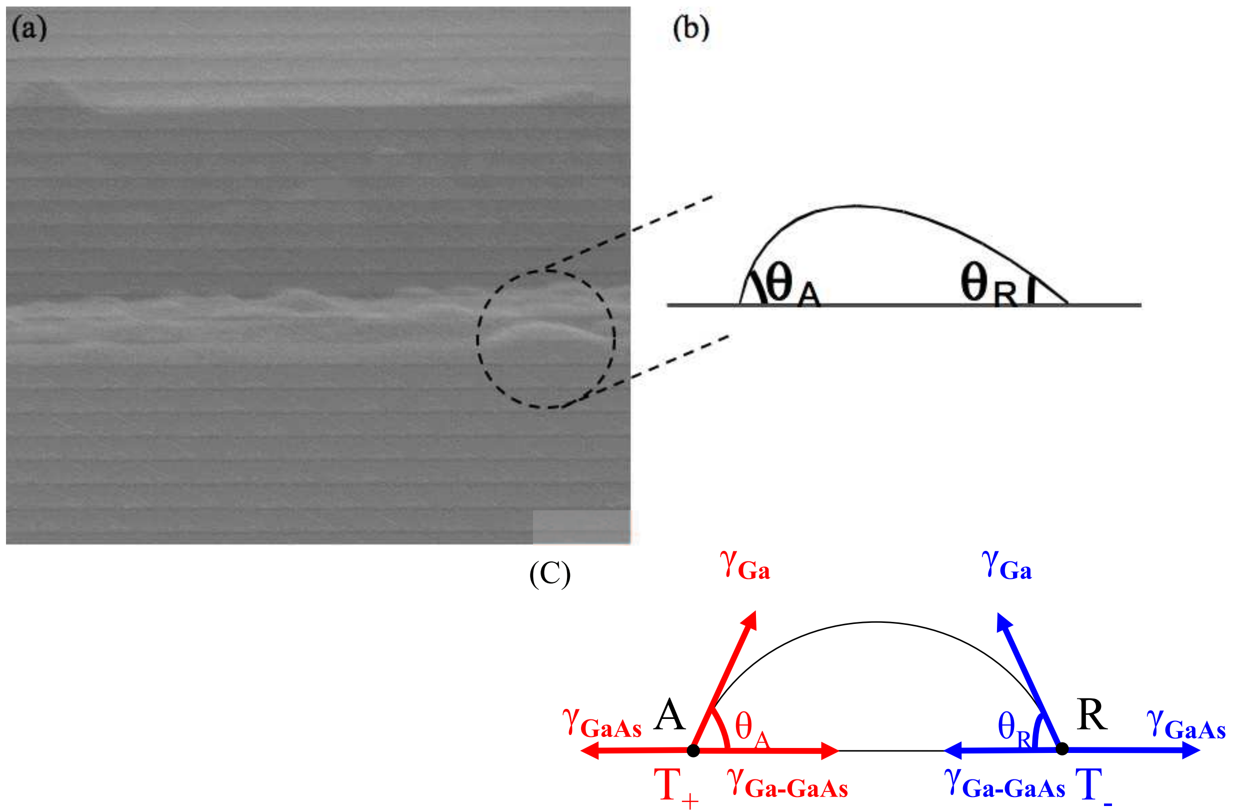

Figure 3.10 (a) SEM images of the side view of the instantaneous 30 kV Ga^+ irradiated GaAs surfaces. The imaging angle is 83º. (b) Schematic illustration of the contact angles of droplets in motion. θ_A and θ_R indicate the advancing and receding contact angles of a droplet. (c) Schematic illustration of the contact angles of droplets in motion.

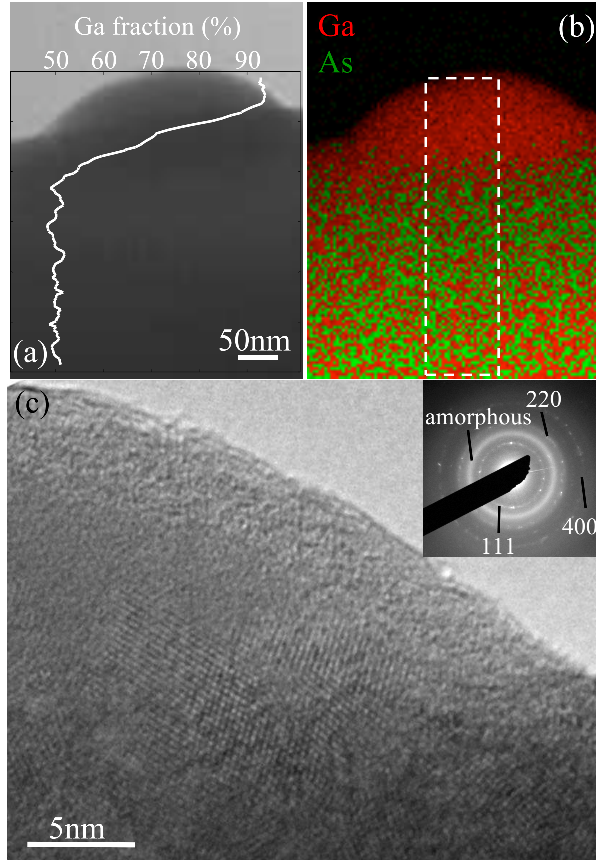

Figure 3.11 (a) Bright-field STEM image of a typical droplet (30 kV, 4.0 × 10^{16} cm^{-2}) and (b) corresponding XEDS map of Ga (red) and As (green). The plot of f_{Ga} as a function of position in (a) was collected from the area indicated in (b). (c) HRTEM image and corresponding SAD pattern, collected in the vicinity of a typical droplet. Reprinted figure with permission from J. H. Wu, W. Ye, B. L. Cardozo, D. Saltzman, K. Sun, H. Sun, J. F. Mansfield, and R. S. Goldman, Appl. Phys. Lett. 95, 153107 (2009). Copyright 2009 by American Institute of Physics.

[1]J. S. Kim and N. Koguchi, Appl. Phys. Lett. **85,** 5893 (2004).

[2]S. M. Scholz, C. Setzer, K. Jacobi, F. Schabert, and J. P. Rabe, J. Mater. Sci. Mater. Elec. **9,** 115 (1998).

[3]Z. Y. AbuWaar, Z. M. Wang, J. H. Lee, and G. J. Salamo, Nanotechnology **17,** 4037 (2006).

[4]D. Datta, S. R. Bhattacharyya, T. K. Chini, and M. K. Sanyal, Nucl. Instrum. Methods Phys. Res. B **193,** 596 (2002).

[5]W. Chen, P. Chen, R. Viswanathan, A. Madhukar, J. Chen, K. Kaviani, Q. Xie, and K. Hu, Mat. Res. Soc. Symp. Proc. **268,** 301 (1992).

[6]K. Furuya, T. Saito, I. Yamada, and T. Hata, J. Electron Microsc. **45,** 291 (1996).

[7]A. Lugstein, B. Basnar, and E. Bertagnolli, J. Vac. Sci. Technol. B **22,** 888 (2004).

[8]J. R. Ro and S. B. Kim, J. Cryst. Growth **188,** 377 (1998).

[9]L. Hong, Z. Liu, X. T. Zhang, and S. K. Hark, Appl. Phys. Lett. **89,** 193105 (2006).

[10]X. Y. Yang, G. M. Wang, P. Slattery, J. Z. Zhang, and Y. Li, Cryst. Growth Des. **10,** 2479 (2010).

[11]O. Hunderi and R. Ryberg, J. Phys. F Met. Phys. **4,** 2084 (1974).

[12]M. Nisoli, S. Stagira, S. De Silvestri, A. Stella, P. Tognini, P. Cheyssac, and R. Kofman, Phys. Rev. Lett. **78,** 3575 (1997).

[13]Q. Wei, J. Lian, W. Lu, and L. M. Wang, Phys. Rev. Lett. **100,** 076103 (2008).

[14]J. B. Malherbe, Crit. Rev. Solid State **19,** 129 (1994).

[15]Y. Homma, H. Okamoto, and Y. Ishii, Jpn. J. Appl. Phys. **24,** 934 (1985).

[16]S. W. MacLaren, J. E. Baker, N. L. Finnegan, and C. M. Loxton, J. Vac. Sci. Technol. A **10,** 468 (1992).

[17]A. Lugstein, B. Basnar, and E. Bertagnolli, Nucl. Instrum. Methods Phys. Res. B **217,** 402 (2004).

[18]J. Tersoff, D. E. Jesson, and W. X. Tang, Science **324,** 236 (2009).

[19]E. Hilner, A. A. Zakharov, K. Schulte, P. Kratzer, J. N. Andersen, E. Lundgren, and A. Mikkelsen, Nano Lett. **9,** 2710 (2009).

[20]J. Tersoff, D. E. Jesson, and W. X. Tang, Phys. Rev. Lett. **105,** 4 (2010).

[21]T. Ishitani and H. Kaga, J. Electron Microsc. **44,** 331 (1995).

[22]T. E. Everhart and R. F. M. Thornley, J. Sci. Instrum. **37,** 246 (1960).

[23]K. A. Grossklaus and J. M. Millunchick, J. Appl. Phys. **109,** 11 (2011).

[24]C. G. Granqvist and R. A. Buhrman, J. Appl. Phys. **47,** 2200 (1976).

[25]E. M. Wong, J. E. Bonevich, and P. C. Searson, J. Phys. Chem. B **102,** 7770 (1998).

[26]G. Rizza, Y. Ramjauny, T. Gacoin, and L. Vieille, Phys. Rev. B **76,** 245414 (2007).

[27]J. Z. Chen, S. M. Troian, A. A. Darhuber, and S. Wagner, J. Appl. Phys. **97,** 9 (2005).

[28]S. C. Hardy, J. Cryst. Growth **71,** 602 (1985).

[29]M. L. Ford and A. Nadim, Phys. Fluids **6,** 3183 (1994).

[30]G. Rizza, A. Dunlop, and A. Dezellus, Nucl. Instrum. Methods Phys. Res. B **256,** 219 (2007).

[31]A. Lugstein, B. Basnar, G. Hobler, and E. Bertagnolli, J. Appl. Phys. **92,** 4037 (2002).

CHAPTER 4

Formation and Evolution of Focused-Ion-Beam-Induced Ripples

4.1 Overview

This chapter opens with background information, including a review of irradiation-induced ripple formation on semiconductors. Next, the experimental details for the studies of ripple formation and evolution on InSb surfaces are described. We then discuss the influences of the ion fluence and the local ion beam angle of incidence on ripple formation. Finally, we consider the ion fluence dependence of the surface morphology beyond ripples. The chapter concludes with a summary.

4.2 Background

Ion-beam irradiation of semiconductor surfaces has emerged as a promising approach to generating a variety of self-organized nanostructures, including nanodots/islands and ripples.[1-22] The reported ripple wavelengths (λ) range from 10 to 1000 nm, with typical ratios of height to wavelength (aspect ratio) of 0.1 or less.[7,9,11,12,14,15,20,22,23] In addition, the ripple wavevector is either parallel or perpendicular to the projected ion beam direction, often termed "parallel-mode" or "perpendicular-mode" ripples, respectively. Figure 4.1 (a) and (b) show the illustrations of "parallel-mode" and "perpendicular-mode" ripples, respectively. For both broad-beam and focused ion beam (FIB) irradiation of semiconductors in the ion fluence ranging from 10^{15} to 10^{18} cm^{-2}, the ripple amplitude has been reported to grow exponentially with time; further irradiation of rippled surfaces leads to a saturation of the ripple amplitude.[7,11,14,15,24-26] For example, Fig. 4.2 shows RMS roughness as a function of ion fluence for GaAs surfaces irradiated with 60 keV Ar^+ ion at 60° angle of ion beam incidence and the corresponding AFM images of the GaAs surfaces irradiated with ion fluences of 5×10^{17} and 1×10^{18} cm^{-2}. The surface roughness increases exponentially with ion fluence, followed by a saturation of ripple amplitude beyond an ion fluence of 1×10^{18} cm^{-2}.

The exponential growth of the ripple amplitude has been explained in terms of a competition between sputtering-induced roughening and diffusion-induced smoothing. Sputtering-induced roughening is typically attributed to an amplification of surface perturbations induced by spatial variations in sputter yield. For example, broad-beam

irradiation is typically described in terms of the ion angle of incidence with respect to the substrate, θ_B, as shown in Fig. 4.3. For off-normal incidence (i.e. $\theta_B \neq 0$) irradiation, increased sputtering occurs at a trough in comparison with that at a crest, leading to the simplification of surface perturbations. An additional consideration is the effective angle of incidence, θ_{eff}, which is the angle between the incident ion beam and the local surface normal, as shown in Fig. 4.3(a). Frost et al showed that N_2^+ broad-beam irradiation of pre-roughened surfaces led to surface roughening, presumably due to a θ_{eff} -dependent sputtering yield. In terms of Ga+ FIB irradiation, Santamore et al. showed that the Si sputtering yield increases with θ_{eff}, as shown in Fig. 4.3(b). To date, ripples have been reported solely for $\theta_B \neq 0$, and nanorod formation on ripple crests has not been reported. Furthermore, the influence of θ_{eff} on irradiation-induced surface evolution has not yet been explored.

In this chapter, we describe the influence of θ_{eff} on irradiation-induced surface evolution of a low binding energy compound, InSb, for which the irradiation-induced variations in θ_{eff} are expected be maximized.[27] We tune θ_{eff} by varying the pitch and/or the dwell time. With increasing θ_{eff}, the surface morphology evolves from pits to ripples and finally to featureless surfaces. Further irradiation of the rippled surfaces leads to the nucleation of islands at the ripple crests, followed by the growth of nanorod arrays. This ripple-nanorod transition, triggered by preferential sputtering and island-induced-self-shielding, provides a new approach for achieving dense arrays of nanorods with controllable spacings. The details of nanorod formation and growth will be discussed in the Chapter 5.

4.3 Experimental Details

For these studies, (001) InSb undoped wafers were simultaneously irradiated and imaged using an FEI Nova 200 NanoLab dual-beam workstation. Ion-irradiation was carried out using normal-incidence 30 kV Ga ions in a raster scan mode using single (multiple) passes, with 19 nm (23 nm) beam spot sizes. The ion fluences ranged from 2.3 $\times 10^{15}$ cm^{-2} to 4.5 $\times 10^{16}$ cm^{-2}.[7] The single-pass FIB irradiations were carried out using a fixed dwell time of 20 ∝s with pitch, p, ranging from 4 to 17 nm, (80-10 % beam spot overlap) or using a fixed p = 8 nm, with dwell time ranging from 5 to 55 ∝s (60 % beam spot overlap). Multiple-pass FIB irradiations were carried out using p = 8 nm and 20 ∝s dwell time (65 % beam spot overlap). The corresponding p/d ratios are 0.21-0.89 (0.42) for 19 (23) nm beam spot sizes. Since negligible ion flux variations are predicted for p/d ≤ 0.64, we expect these conditions to lead to spatially uniform ion fluxes over the scanned areas.[28] The formation of islands, ripples, and nanorods was noted via in-situ SEM at θ_B =0 and 52□. The islands and ripple surface profiles were subsequently determined using ex-situ tapping mode atomic force microscopy. For this purpose, we define ripples with wavevectors parallel or perpendicular to the slow scan direction as "parallel-mode" or "perpendicular-mode" ripples, respectively. Prior to FIB-induced nanostructure formation, cross-sectional transmission electron microscopy (XTEM) samples were prepared by mechanical polishing, followed by argon ion milling at 77K. TEM imaging and electron diffraction were carried out in a JEOL 2010F operating at 200 kV and a JEOL 3011 operating at 300 kV. X-ray energy dispersive spectroscopy (XEDS)

data was collected using scanning transmission electron microscopy (STEM) mode in the JEOL 2010F.

4.4 Ripple formation: Ion fluence dependence

To examine the influence of ion fluence on the evolution of irradiated InSb surfaces, we irradiated InSb with single-pass FIB. Figures 4.4 (a) – 4.4 (g) show the AFM images of the irradiated InSb surfaces as a function of increasing ion fluence. In Fig. 4.4 (a), at an ion fluence of 2.3×10^{15} cm^{-2}, randomly distributed circular pits and islands are observed. Interestingly, as the ion fluence is increased from 3.5×10^{15} cm^{-2} to 3.6×10^{15} cm^{-2}, the surface features transition from circular pits and islands to circular pits and perpendicular-mode ripples, shown in Fig. 4.4 (b) and (c). As the ion fluence is increased to the range of 1×10^{16} and 2×10^{16} cm^{-2}, shown in Fig. 4.4 (d) and (e), parallel-mode ripples with islands at the ripple crests are apparent. As the ion fluence is further increased to 2.1×10^{16} cm^{-2}, shown in Fig. 4.4 (f), hillocks and islands are observed. Interestingly, for ion fluences of $3.7 \pm 0.3 \times 10^{16}$ cm^{-2}, perpendicular-mode ripples are observed, as shown in Fig. 4.4 (h). As the ion fluence is further increased to 4.5×10^{16} cm^{-2}, shown in Fig. 4.4 (i), featureless surfaces, without pits or ripples, are apparent.

Figure 4.5 (a) presents a compilation of the surface roughness vs. ion fluence for InSb surfaces irradiated with fixed dwell time or pitch. For both cases, the surface roughness increases exponentially to maximum values ~80 nm, presumably due to a sputtering-dominated roughening mechanism.[7] However, with further ion fluence

increases, a monotonically decreasing surface roughness is observed, presumably due to a diffusion-dominated smoothening mechanism. Similarly, Ar^+ irradiation of InSb has been reported to induce a surface roughness which increases exponentially with ion fluence.[29,30] Further irradiation with N_2^+ led to surface smoothening, which was explained by the increasing sputter yield with increasing θ_{eff}.[29] Thus, we consider the influence of θ_{eff} on ripple formation, as described next in section 4.5.

4.5 Ripple formation: θ_{eff} dependence

We determined the values of θ_{eff} for fixed pitch and dwell times using quantitative AFM measurements of FIB lines-scan induced trenches. At each trench edge, θ_{eff} was estimated as the height derivative with respect to the slow scan direction. For example, Fig. 4.6 (a) and (b) show the AFM image of a trench and the corresponding schematic illustration of FIB line scan, respectively. Figure 4.6 (c) shows the height profiles with respect to the FIB slow (solid lines) and fast (dashed lines) scan direction, with arrows indicating the edge at which surface profiles were used to estimate θ_{eff}. We expect this 1D approximation for θ_{eff} to be suitable for 2D iff the steady-state θ_{eff} , θ_{eff}^{SS} , has been reached:

$$\theta_{eff}^{SS} = \arctan\left[J \propto Y / v \propto N\right] \qquad (4.1)$$

where J is the ion flux of 6.3×10^{16} cm^{-2}, v is the scan speed (ranging from 0.2 to 2.3 ∝m/s), and N is the density of InSb (5.78 g/cm^3). The sputter yield, Y, is determined using a volume loss analysis of 2D AFM images of InSb surfaces, as described in Appendix A. Plots of the measured θ_{eff} and the calculated θ_{eff}^{SS} as a function of scan speed

are shown in Figs. 4.7. Since the measured θ_{eff} is 80 +/- 10% of the calculated θ_{eff}^{SS}, we consider our 1D approximation for θ_{eff} to be suitable for our 2D scans.

We describe ion-induced surface evolution as a function of θ_{eff}. AFM images of single-pass FIB irradiated InSb surfaces are shown in Fig. 4.8. For θ_{eff} ranging from $8.6\pm1.7^\circ$ to $51.8\pm6.7^\circ$, the surface morphology evolves from randomly distributed pits and islands to parallel-mode ripples and islands, and then to featureless surfaces, as shown in Figs. 4.8 (a)-(c). From θ_{eff} ranging from $3.5\pm0.4^\circ$ to $49.3\pm3.9^\circ$, the surface morphology evolves from pits, islands and perpendicular-mode ripples to islands and parallel-mode ripples or hillocks, and finally to islands and perpendicular-mode ripples, as shown in Figs. 4.8 (e)-(h). It is interesting to note that the θ_{eff} –dependent variation in surface morphology shown in Fig. 4.8 is reminiscent of the θ_B –dependent morphology variations often reported in the literature.[7,10,18,20]

In Fig. 4.9, we plot the RMS roughness vs. θ_{eff} for InSb surface irradiated with fixed dwell time (Fig. 4.3 (b) and (f)) or pitch (Fig. 4.3 (c) and (e)). For both cases, the surface roughness increases linearly with θ_{eff}, suggesting that θ_{eff} has increased the sputtering yield. In addition, as θ_{eff} increases from 4° to 54°, the surface morphology evolves from pits and islands (Fig. 4.3 (b)) to perpendicular-mode ripples (Fig. 4.3 (c)), and then to parallel-mode ripples (Fig. 4.3 (e) and (f)). The formation of ripples and their subsequent rotation is presumably due to the influence of θ_{eff} on the anisotropic amplification of surface perturbations, similar to that of θ_B. To our knowledge, the influence of θ_{eff} has not been explored. Therefore, further quantitative modeling of FIB

irradiation-induced surface evolution processes need to include the roles of the θ_{eff}. Thus, we can apply this new model to predict what will happen in other systems

4.6 Beyond ripples: Ion fluence dependence

To examine the ion fluence dependence of the surface evolution beyond ripples, we consider Figs. 4.10 (a)-(h), SEM images of FIB irradiated InSb surfaces, with corresponding FFTs as insets in Figs. 4.10 (e)-(h). For ion fluences of 8×10^{15} cm^{-2}, shown in Figs. 4.10 (a) and (e), parallel-mode ripples are apparent. For the rippled morphology in Fig. 4.10 (a), high-order spots are apparent in the FFT, indicating a long-range periodicity (λ = 290 nm), which corresponds to the observed ripple wavelength. As the ion fluence is increased to 1.6×10^{16} cm^{-2}, shown in Figs. 4.10 (b) and (f), it is apparent that islands have formed on the ripple crests; the FFT of the SEM image indicates a ripple periodicity similar to that in Fig. 4.10 (a). Since the islands appear only on the ripple crests, their formation is likely due to sputtering, followed by redeposition, as predicted by Kree.[31] As the ion fluence is further increased to 4×10^{16} cm^{-2}, shown in Figs. 4.10 (c) and (g), the rippled surfaces transform to nanorods capped with islands. In this case, the FFT has developed spots, suggesting a periodicity along the ripple wave vector direction (λ = 290 nm), and a ring, suggesting an isotropic periodicity (λ = 420 nm). With further irradiation, the height of the cone-shaped nanorods increases, with a substantial decrease in the size of the capped islands. Interestingly, at an ion fluence of 5.6×10^{16} cm^{-2}, shown in Figs. 4.10 (d) and (h), a ring is observed in the FFT, consistent with a random distribution of nanorods with a mean separation of 375 nm.

To study the formation mechanism of nanorods, we examine the structure and composition of nanorods. Figures 4.11 (a) and (b) show a dark field STEM image and a corresponding XEDS map, [where red (green) denotes In (Sb)] for a single nanorod. The XEDS map reveals a nearly pure In nanorod head, and a mixture of In and Sb in the nanorod body. The HRTEM images in Figs. 4 (c) and 3 (d) show that both the nanorod head and body contain nanocrystals without a preferred orientation. Using a 100 nm SAD aperture, we probed the nanorod head and body. The SAD pattern from the nanorod head, shown in Fig. 4 (c), reveals three spotty rings with interplanar spacings of 1.85±0.04 Å, 1.43±0.06 Å, and 0.94±0.03 Å, corresponding to the {200}, {022}, {040} of orthorhombic In. The SAD pattern from the nanorod body, shown in Fig. 4 (d), reveals three spotty rings with interplanar spacings of 3.74±0.05 Å, 3.23±0.05 Å, and 2.29 Å corresponding to the {111}, {022}, {113} of zincblende InSb. The formation of polycrystalline In heads and polycrystalline InSb bodies suggest that the nanorod formation is due to an In island-induced reduction in the local sputtering yield at the crests of the rippled InSb surfaces.[32] In addition, as shown in Figs. 4.10 (c)-(d), the island diameters are much smaller than the width of nanorod body, suggesting an island-induced self-shielding mechanism, possibly assisted by In and Sb redeposition.[33]

4.7 Summary and conclusions

In summary, we have examined the formation and evolution of ripples on ion-irradiated semiconductor surfaces, using normal incidence FIB irradiation of InSb. To consider the role of θ_{eff} on irradiation-induced surface evolution, we examine the

influence of θ_{eff} on surface evolution of InSb by varying the pitch and/or the dwell time. With increasing θ_{eff}, the surface morphology evolves from pits to ripples to featureless surfaces. Continued irradiation of the rippled surfaces leads to a transition from lateral ripples to arrays of nanorods. This ripple-nanorod transition, triggered by preferential sputtering and island-induced-self-shielding, provides a new approach for achieving dense arrays of nanorods, which will be discussed in Ch. 5.

4.8 Figures and References

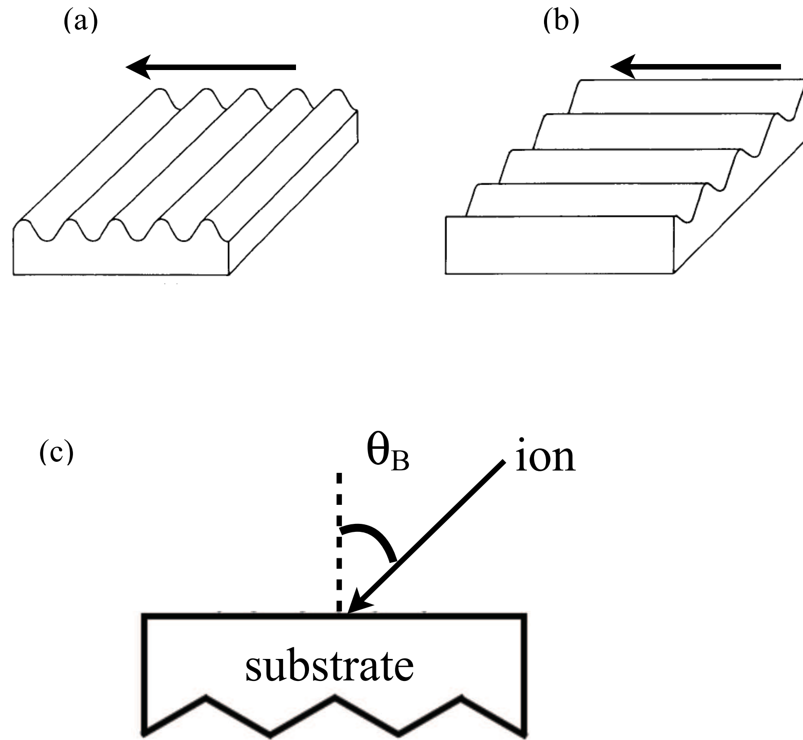

Figure 4.1 Illustration of parallel-mode ripples (a) and perpendicular-mode ripples (b). The arrow indicates the projected ion beam direction; (c) Illustration of the angle of ion beam incidence. Reprinted figure with permission from R. Mark Bradley, James M. E. Harper, J. Vac. Sci. Technol. A 6, 2390 (1988). Copyright 1988 by American Vacuum Society.

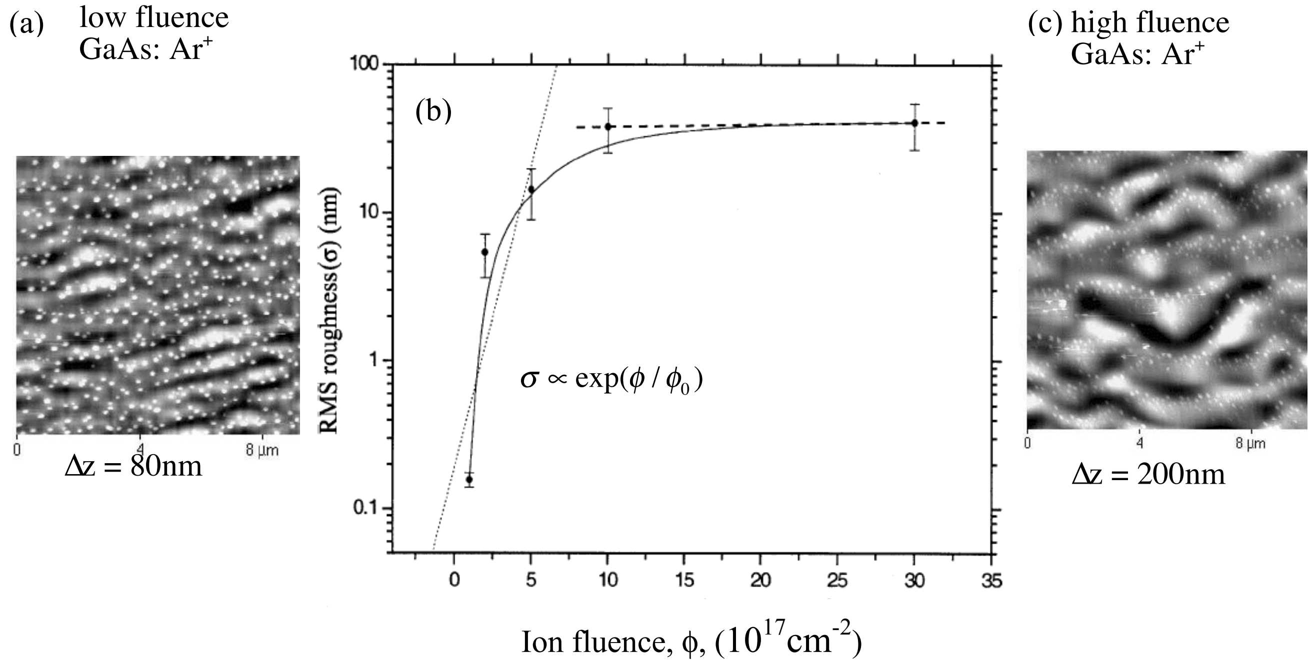

Figure 4.2 (a) ripple formed on GaAs surface irradiated with 5×10^{17} cm^{-2}; (b)RMS roughness as a function of ion fluence for GaAs surfaces irradiated with 60 keV Ar+ ion at 60 angle of ion beam incidence; (c) ripple formed on GaAs surface irradiated with 1×10^{18} cm^{-2}. Reprinted figure with permission from D Datta, S.R Bhattacharyya, T.K Chini, M.K Sanyal, Nucl. Instrum. Methods Phys. Res. Sect. B 193, 596 (2002). Copyright 2002 by Elsevier.

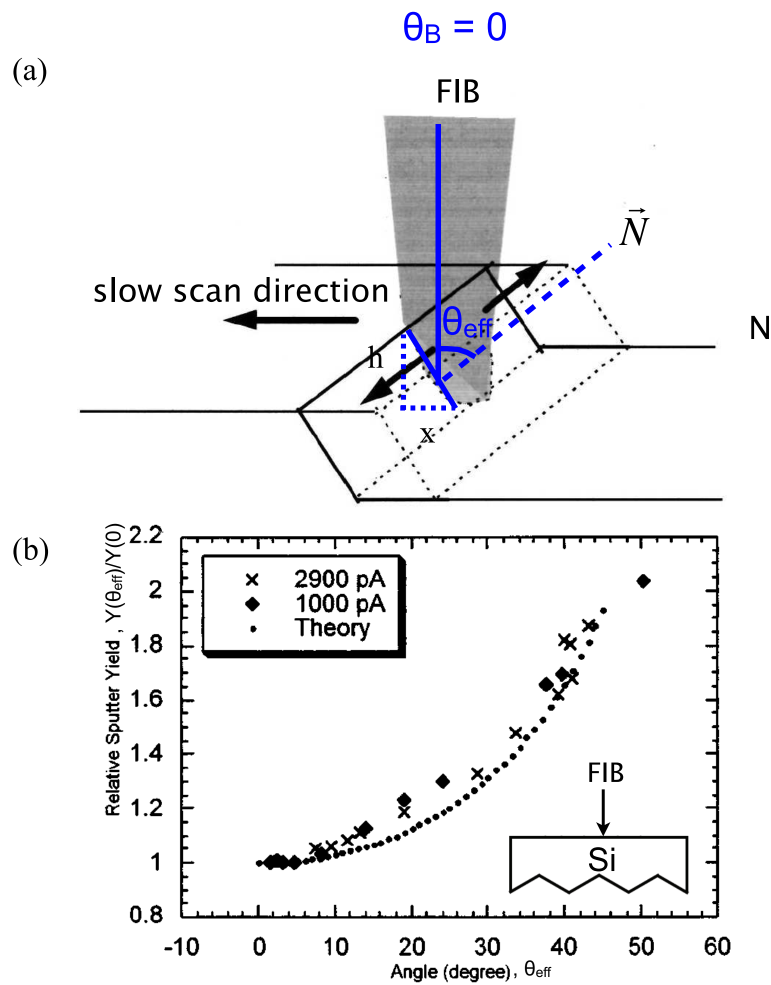

Figure 4.3 (a) schematic of the relative orientation of the ion beam and the local surface normal along a FIB-induced trench; (b) the relative sputtering yield of Si irradiated with Ga FIB as a function of θ_{eff}. Reprinted figure with permission from D. Santamore, K. Edinger, J. Orloff, and J. Melngailis, J. Vac. Sci. Technol. B 15, 2346 (1997). Copyright 1997 by American Vacuum Society.

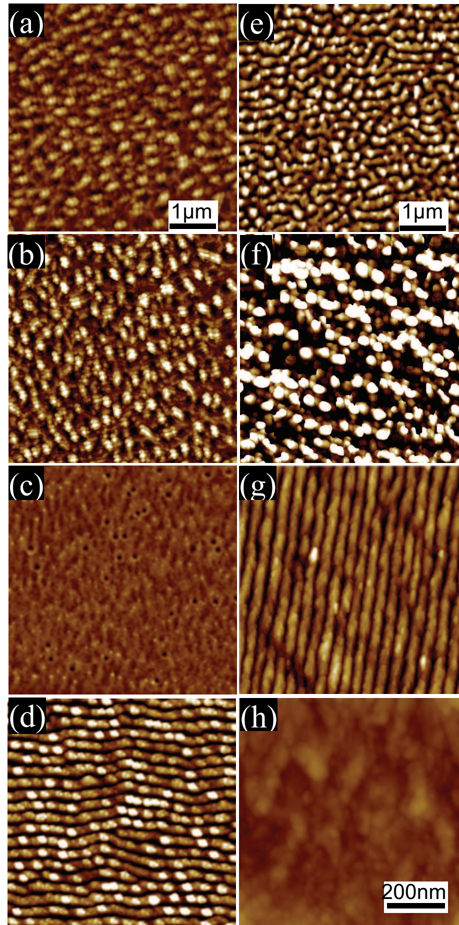

Figure 4.4 Influence of ion fluence and θ_{eff} on InSb surface morphology: (a) 2.3×10^{15} cm^{-2} and 11.6° (b) 3.5×10^{15} cm^{-2} and 19.7°, (c) 3.6×10^{15} cm^{-2} and 4.2°; (d) 1.0×10^{16} cm^{-2} and 45.4°; (e) 2×10^{16} cm^{-2} and 44.7°; (f) 2.1×10^{16} cm^{-2} and 54.3° (g) 4×10^{16} cm^{-2} and 58.8°, and (h) 4.5×10^{16} cm^{-2} and 72.6°; Pits and islands are observed in (a) and (b); ; perpendicular-mode ripples in (c) and (g); parallel-mode ripples in (d) and (e); hillocks in (f); and featureless surfaces for (h). For all images, the color-scale ranges displayed are 160 nm, and the slow scan direction runs from the top to the bottom of the page. FIB irradiations were carried out using a fixed dwell time of 20μs with pitches of (a) 17nm, (b) 13nm, (d) 8nm, (f) 6nm, and (h) 4nm; or with a fixed pitch of 8 nm and dwell times of (a) 5μs, (b) 25 μs, and (g) 55μs.

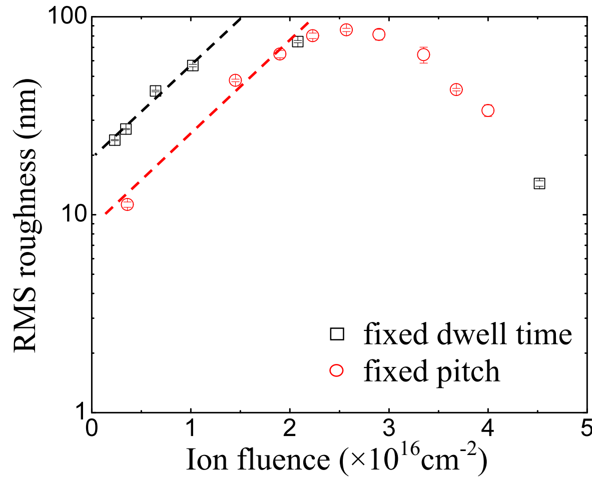

Figure 4.5 Logarithm of the RMS roughness as a function of ion fluence. The ion fluence was controlled by varying the pitch (square symbols) or the dwell time (circle symbols). The rms roughness increases linearly with θ_{eff}, presumably due to a corresponding increase in sputtering yield with θ_{eff} .

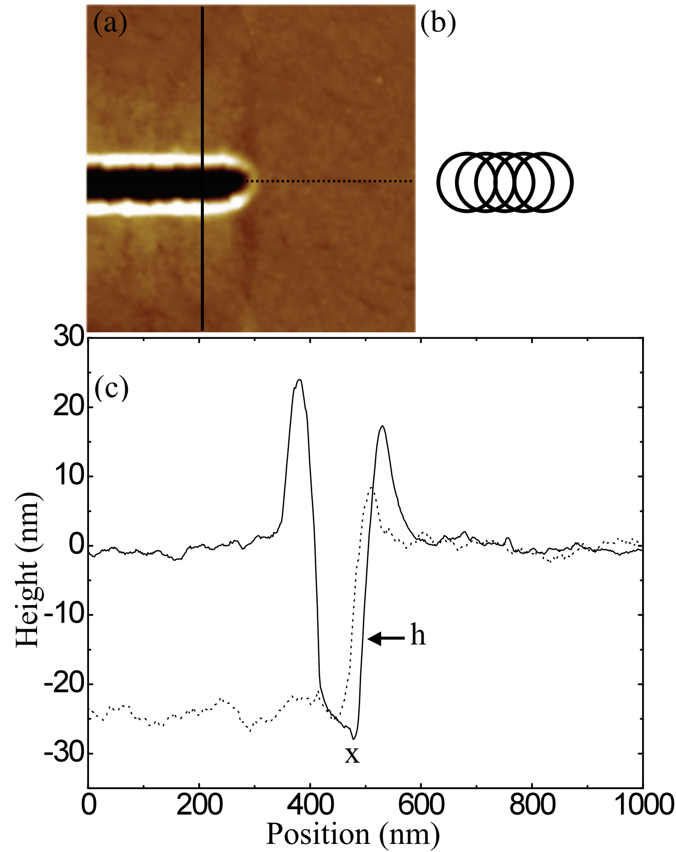

Figure 4.6 (a) AFM image of trench milled using the line-scan shown schematically in (b); (c) height profiles with respect to the slow (solid lines) and fast (dashed lines) scan directions, with arrows indicating the edges at which surface profiles were used to estimate θ_{eff}. The θ_{eff} is determined as the height derivative, $\tan^{-1}(\partial h/\partial x)$, at the edge of each trench. We expect this 1D approximation for θ_{eff} to be suitable for 2D if the steady-state θeff has been reached.

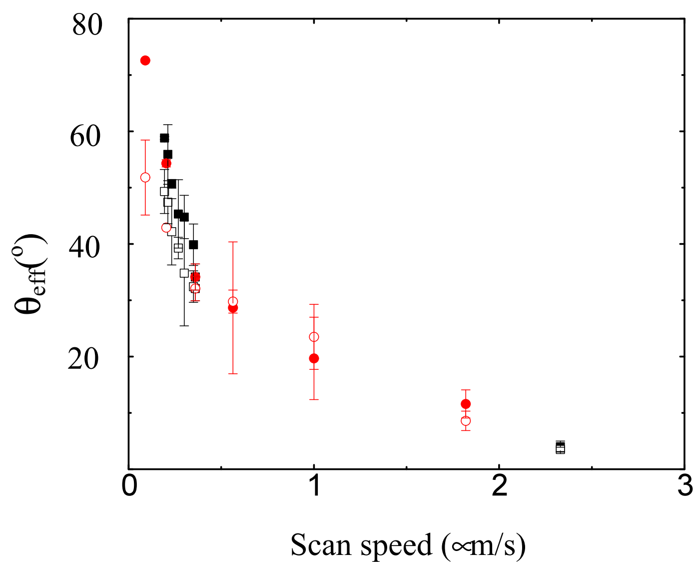

Figure 4.7 (a) Plots of the measured θ_{eff} and the calculated θ_{eff}^{ss} as a function of scan speed. The open symbols represent the measured θ_{eff} and the solid symbols represent the calculated θ_{eff}^{ss}. The FIB scan speed was tuned via controlling dwell time (square symbols) and pitch (circular symbols).

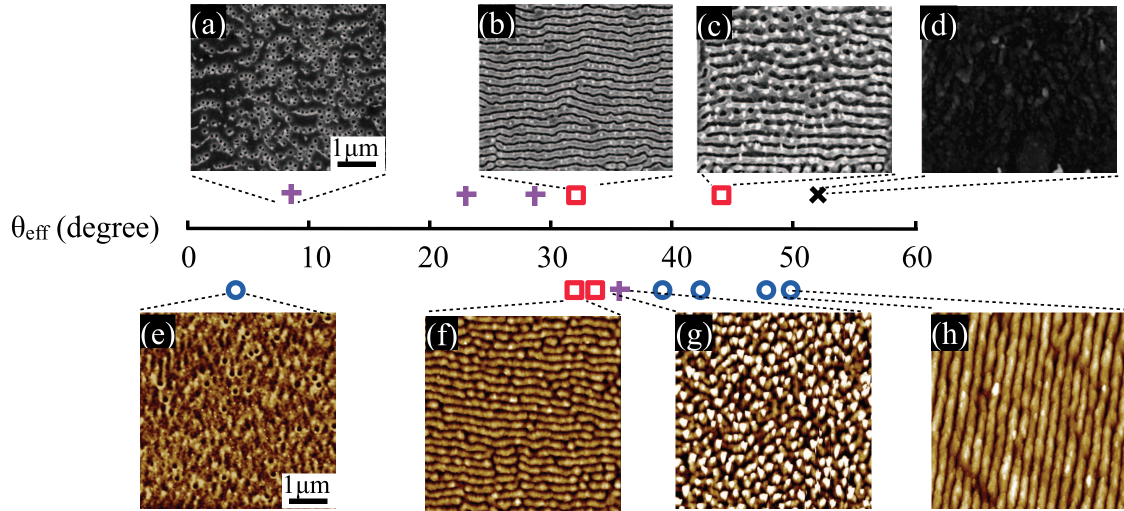

Figure 4.8 θ_{eff} dependence of ion-induced surface evolution. +: hillocks/pits; ×: featureless surfaces; □: parallel-mode ripples; ○: perpendicular-mode ripples. (a) pits and islands for θ_{eff} = 8.6±1.7°; (b) parallel-mode ripples for θ_{eff} = 32±2.1°; (c) featureless surfaces for θ_{eff} = 51.8±6.7°; (e) perpendicular-mode ripples for θ_{eff} = 3.5±0.4°; (f) parallel-mode ripples for θ_{eff} = 32.4±2.8°; (g) hillocks for θ_{eff} = 34.6±9.3° (h) perpendicular-mode ripples for θ_{eff} = 49.3±3.9°. For all images, the color-scale ranges displayed are 160 nm, and the slow scan direction runs from the top to the bottom of the page. FIB irradiations were carried out using a fixed dwell time of 20µs with pitches of (a) 17nm, (b) 13nm, (c) 8nm, (d) 6nm, and (h) 4nm; or with a fixed pitch of 8 nm and dwell times of (e) 5µs, (f) 25 µs, (h) 30 µs and (h) 55µs.

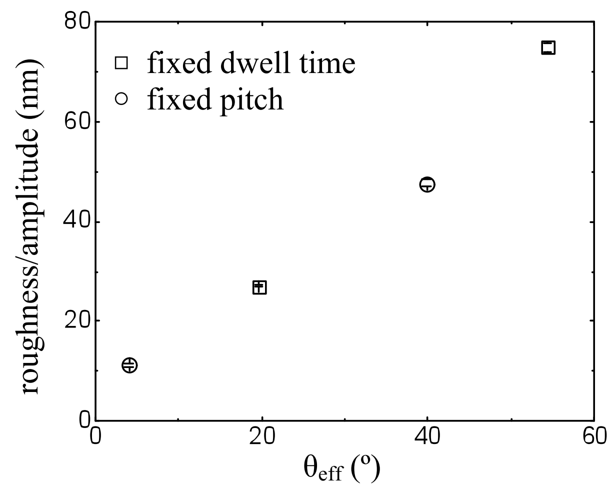

Figure 4.9 Surface roughness as a function of θ_{eff} for both fixed dwell times and pitches. The surface roughness increases linearly with θ_{eff}, presumably due to a corresponding increase in sputter yield with θ_{eff}.

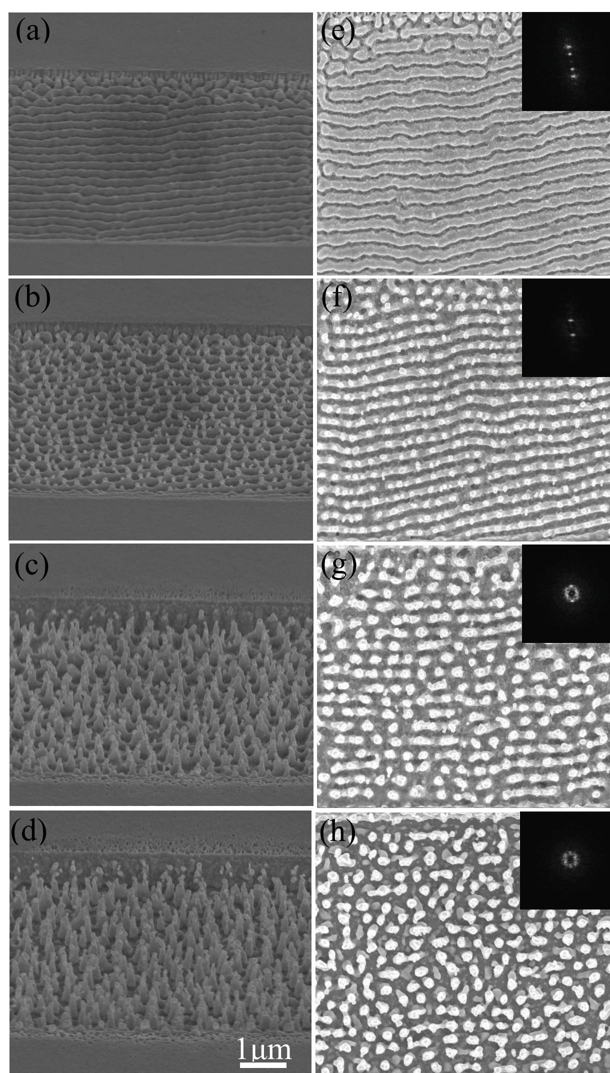

Figure 4.10 SEM images of fluence dependence of ripple evolution (for a pitch of 8 nm and dwell time = 10 ∝s), including (a), (e) (ion fluence of 8×10^{15} cm^{-2}) ripples; (b), (f) (ion fluence of 1.6×10^{16} cm^{-2}) ripples and islands on crests of ripples; (c), (g) (ion fluence of 4×10^{16} cm^{-2}) lateral ordering of nanorods capped with islands; and (d), (h) (ion fluence of 5.6×10^{16} cm^{-2}) randomly distributed nanorods. For all images, the slow scan direction runs from the top to the bottom of the page. Images (a)-(d) ((e)-(h)) were collected with 52° (normal) angle of incidence. The insets in Fig. 3 (e)-(h) are FFT spectra of the SEM images in (a)-(d).

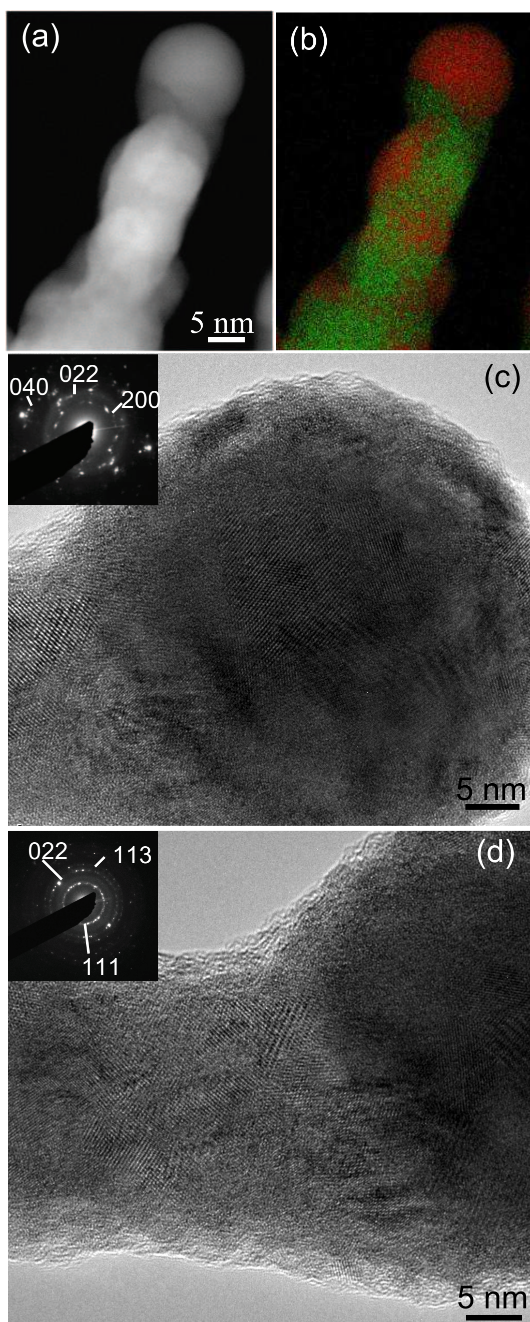

Figure 4.11 (a) Dark-field STEM image of a single nanorod and (b) corresponding XEDS map of In (red) and Sb (green); HRTEM images and corresponding SAD pattern, collected in the (c) head and (d) body regions of a nanorod.

[1]S. Facsko, T. Dekorsy, C. Koerdt, C. Trappe, H. Kurz, A. Vogt, and H. L. Hartnagel, Science **285,** 1551 (1999).

[2]W. L. Chan and E. Chason, J. Appl. Phys. **101,** 121301 (2007).

[3]B. Ziberi, M. Cornejo, F. Frost, and B. Rauschenbach, J. Phys-Condens Mat. **21,** 224003 (2009).

[4]C. S. Madi, B. Davidovitch, H. B. George, S. A. Norris, M. P. Brenner, and M. J. Aziz, Phys. Rev. Lett. **101,** 246102 (2008).

[5]F. Frost, B. Ziberi, T. Hoche, and B. Rauschenbach, Nucl. Instrum. Meth. B **216,** 9 (2004).

[6]C. S. Madi, E. Anzenberg, K. F. Ludwig, and M. J. Aziz, Phys. Rev. Lett. **106,** 4 (2011).

[7]D. Datta, Bhattacharyya, Sr., T. K. Chini, and M. K. Sanyal, Nucl. Instrum. Meth. Phys. Res. B **193,** 596 (2002).

[8]S. Macko, F. Frost, B. Ziberi, D. F. Forster, and T. Michely, Nanotechnology **21,** 9 (2010).

[9]S. W. Maclaren, J. E. Baker, N. L. Finnegan, and C. M. Loxton, J. Vac. Sci. Technol. A **10,** 468 (1992).

[10]F. Rose, H. Fujita, and H. Kawakatsu, Nanotechnology **19,** 7 (2008).

[11]A. D. Brown, J. Erlebacher, W. L. Chan, and E. Chason, Phys. Rev. Lett. **95,** 4 (2005).

[12]G. Carter and V. Vishnyakov, Phys. Rev. B **54,** 17647 (1996).

[13]M. Castro, R. Cuerno, L. Vazquez, and R. Gago, Phys. Rev. Lett. **94,** 4 (2005).

[14]W. L. Chan and E. Chason, J. Appl. Phys. **101,** 46 (2007).

[15]J. Erlebacher, M. J. Aziz, E. Chason, M. B. Sinclair, and J. A. Floro, Phys. Rev. Lett. **82,** 2330 (1999).

[16]S. Facsko, H. Kurz, and T. Dekorsy, Phys. Rev. B **63,** 5 (2001).

[17]F. Frost, A. Schindler, and F. Bigl, Phys. Rev. Lett. **85,** 4116 (2000).

[18]F. Frost, B. Ziberi, T. Hoche, and B. Rauschenbach, Nucl. Instrum. Methods Phys. Res. B **216,** 9 (2004).

[19]F. Frost, B. Ziberi, A. Schindler, and B. Rauschenbach, Appl. Phys. A-Mater., **91,** 551 (2008).

[20]S. W. MacLaren, J. E. Baker, N. L. Finnegan, and C. M. Loxton, J. Vac. Sci. Technol. A **10,** 468 (1992).

[21]B. Ziberi, M. Cornejo, F. Frost, and B. Rauschenbach, J. Phys.-Conden. Matt. **21,** 224003 (2009).

[22]B. Ziberi, F. Frost, T. Hoche, and B. Rauschenbach, Phys. Rev. B **72,** 7 (2005).

[23]S. R. Saeed, O. P. Sinha, F. Krok, T. Zembok, R. Pedrys, and M. Szymonski, Nucl. Instrum. Methods Phys. Res. B **267,** 2752 (2009).

[24]A. D. Brown and J. Erlebacher, Phys. Rev. B **72,** 10 (2005).

[25]C. S. Madi, B. Davidovitch, H. B. George, S. A. Norris, M. P. Brenner, and M. J. Aziz, Phys. Rev. Lett. **101,** 4 (2008).

[26]M. A. Makeev, R. Cuerno, and A. L. Barabasi, Nucl. Instrum. Methods Phys. B **197,** 185 (2002).

[27]M. Yano, H. Yokose, Y. Iwai, and M. Inoue, J. Cryst. Growth **111,** 609 (1991).

[28]A. A. Tseng, J. Micromech. Microeng. **14,** R15 (2004).

[29]F. Frost, R. Fechner, B. Ziberi, J. Vollner, D. Flamm, and A. Schindler, J. Phys.-Conden. Matt., **21,** 20 (2009).

[30]F. Krok, Vacuum **83,** 745 (2008).

[31]R. Kree, T. Yasseri, and A. K. Hartmann, Nucl. Instrum. Meth. B **267,** 1403 (2009).

[32]S. Le Roy, E. Barthel, N. Brun, A. Lelarge, and E. Sondergard, J. Appl. Phys. **106,** 094308 (2009).

[33]J. H. Wu and R. S. Goldman, Appl. Phys. Lett. **100,** 053103 (2012).

CHAPTER 5

Formation Mechanism of Focused-Ion-Beam-Induced Nanorods

5.1 Overview

This chapter opens with background information, including a review of irradiation-induced semiconductor nanorod (NR) formation. Next, experimental details for the studies of NRs in this chapter are described. We then discuss the influences of ion fluence, ion energy, and InSb source on NR formation. Finally, we discuss the mechanisms for NR growth, considering the formation and re-supply of the NR caps. This chapter concludes with a summary.

5.2 Background

5.2.1 Semiconductor Nanorods

Recently, the growth of semiconductor nanorods (NRs) has attracted significant attention due to the potential applications of NRs in electronics, photonics, and thermoelectrics.[1-8] Generally, semiconductor NRs are grown via the vapor-liquid-solid (VLS)[6,9] and/or vapor-solid-solid (VSS) modes.[3] Recently, ion irradiation has been used to fabricate NRs with a metal-capped cone-shaped body, and a ratio of base-to-top widths typically greater than 4.[2,10-15] In the case of ion irradiation of Si, unintentional metal impurities resulting from sputtering of metal clamp used to fix Si substrates, provide local sputter masks, resulting in the formation of NRs.[2] For binary III-V compounds, preferential sputtering of group V elements leads to the formation of group III element surface clusters, which in turn serve as local sputter masks.[10,11,14,16,17] For many III-V compounds, cone-shaped NRs capped with group III surface clusters have been observed and explained by a self-sustained etch masking model.[11,18] In this thesis work, a competing model, which includes an alternative mechanism for the resupply of metal dots, is considered.

5.2.2 Models for ion-induced nanorod formation

The self-sustained etch masking model has been hypothesized to describe NR formation and growth in three steps, as shown in Fig. 5.1. During the first step, shown in Fig. 5.1 (a), preferential Group V sputtering induces the formation of a Group III -rich

surface. Next, Group III elements precipitate out to form droplets/islands that serve as local sputter masks, as shown in Fig. 5.1(b). It has been proposed that the Group III droplets/islands are resupplied by ion-enhanced diffusion of group III elements precipitated from the NR body and the substrate.[11,19] We note that both NR body and substrate can release group III elements supplying the group III droplets/islands. In this step, the growth rate is determined by the ion beam flux multiplied by the difference in sputtering yields of the Group III element and the substrate (a III-V compound). As the NRs grow longer, the path length from the substrate to the NR cap increases. Thus, the NR caps shrink, as shown in Fig. 5.1 (c), and the NR growth decelerates. Although this model has been apparently successfully applied to irradiation-induced nanopillar and nanospike growth on III-V surfaces, several open questions remain.[19] Since the sputtering yield of Group III elements typically greater than that of a III-V compound, a mechanism for re-supply of the Group III caps is needed.[20] In many cases, the diameters of the NR bodies are typically much larger than those of the NR caps.Thus, an alternative explanation for the NR shape evolution has been proposed in the context of ion-irradiation-induced nanocone (NC) formation on GaAs surfaces. Specifically, redeposition of sputtered atoms has been proposed as the mechanism for re-supply of Group III caps.[13,21-23] Prior to this thesis research, the relative roles of ion-enhanced diffusion and redeposition on ion-irradiation-induced NR growth was unknown.

In this chapter, we have examined the formation and evolution of irradiation-induced NR growth through a comparison of focused-ion-beam (FIB) irradiation of InSb wafers and InSb/GaAs heterostructures. On both irradiated InSb surfaces, hillocks and In islands evolve to cone-shaped NRs capped with In islands. For InSb wafers, the NR base

diameter increases with ion energy. In the case of InSb/GaAs heterostructures, as the milled depth approaches the InSb/GaAs interface, the cone-shaped NRs transition to capless NRs with a truncated cone shape. In addition, the growth (shrinkage) rate for NRs on InSb (GaAs) surface calculated by considering the competition between sputtering and redeposition of sputtered atoms from the substrate surfaces is similar to the measured values. These results suggest a growth mechanism in which both the NR cap and body are supplied by the redeposition of atoms sputtered from the InSb substrate.

5.3 Experimental Details

For these studies, (001) InSb undoped substrates and 0.55 ∝m InSb undoped films grown on semi-insulating GaAs (001) substrates[24] were simultaneously irradiated and imaged using an FEI Nova 200 NanoLab FIB dual-beam workstation. Room temperature ion irradiation was carried out using normal incidence 10 or 30 kV Ga^+ ions with beam spot sizes of 41 or 19 nm. Ion fluences were varied from 1×10^{16} cm^{-2} to 7×10^{17} cm^{-2}, corresponding to milled depths ranging from 64±6 to 6500±400 nm (56±10 to 1580±40 nm) for InSb (InSb/GaAs). Following irradiation, real-time SEM images were collected at electron beam angles of incidence, θ_B, of 0 and 75. Radial power spectral density (RPSD) analysis of the θ_B = 0 SEM images was then used to determine the in-plane periodicity of the nanostructure arrays.[25] Using θ_B = 75 SEM images, the NR height (including the NR cap) h, and the ratio of the top diameter, d, to the base diameter, d_0, of each NR was determined and used to quantify the cone/truncated cone shape.

5.4 Influence of ion fluence on NR formation

Figures 5.2 (a)-(d) ((e)-(h)) present θ_B = 0 (75°) SEM images of the InSb substrate surfaces as a function of ion fluence. In Fig. 5.2 (a) and (e), for an ion fluence of 1×10^{16} cm^{-2}, hillocks with randomly distributed islands are observed. As the ion fluence is increased to 3.1×10^{16} cm^{-2}, island coarsening occurs, as shown in Fig. 5.2 (b) and (f). Continued irradiation leads to the formation of cone-shaped NRs capped with island caps, as shown in Fig. 5.2 (c) and (g). With further irradiation, the NRs maintain their cone shape and grow vertically at a rate of 3.7±0.1 nm/s, with a substantial decrease in the island cap diameter, as shown in Figs. 5.2 (d) and (h).

5.5 Influence of ion energy on NR formation

We have also examined the ion energy dependence of NR formation on InSb wafers, as shown in Fig. 5.3. As the ion energy is increased from 10 to 30 kV, the NR cone shape and the presence of the island cap are maintained (Figs. 5.3 (b), 5.3 (d)), while the average NR separation increases from 240 to 364 nm (Figs. 5.3 (a), 5.3 (c)). Interestingly, as the ion energy increases from 10 to 30kV, the NRs coarsen, with d_0 increasing from 220±32 nm to 390±60 nm. As will be discussed in Appendix A, the sputtering yield increases with ion energy. Thus, the increase of d_0 with increasing ion energy is likely due to the increased supply of sputtered atoms available for redeposition in that case.[26]

5.6 Influence of InSb source on NR formation

Finally, we examined the influence of the InSb source on FIB-induced InSb NR formation through a comparison of FIB-induced InSb NR formation on InSb/GaAs heterostructures and InSb substrates, as shown schematically in Figs. 5.4 (a) and (b), respectively. For InSb, as discussed in Section 4.6, Ga+ irradiation leads to the formation of cone-shaped NRs capped with In islands, as shown in Fig. 5.4(c). Continued irradiation leads to further NR growth, with a decrease in NR cap diameter, shown in Fig. 5.5(e), consistent with the predictions of the self-sustained etch masking model. Similar effects are observed for Ga+ irradiation of InSb/GaAs heterostructure. For example, Figures 5.5 (a)-(d) [(e)-(h)] show θ_B = 0 (75) SEM images of the InSb/GaAs heterostructures as a function of ion fluence. As the ion fluence is increased from 1×10^{16} to 1×10^{17} cm^{-2}, the irradiated InSb/GaAs surfaces evolve from hillocks and randomly distributed islands to coarsened islands, and finally to cone-shaped NRs capped with islands, similar to the InSb substrate case shown in Figs. 5.2. In addition, the growth rate of NRs is 3.9±0.4 nm/s, similar to that of NRs on InSb wafers. Interestingly, as the ion fluence is increased beyond 1.5×10^{17} cm^{-2}, the NRs shrink on GaAs surfaces at a rate of 2.9 ±0.2 nm/s, and NRs transform to capless truncated-cones, as shown in Figs. 5.5 (d) and (h). With further irradiation, the capless truncated-cone NRs disappear, followed by the formation of droplets, similar to earlier reports of Ga droplet formation on GaAs surfaces.[27] Thus, it appears likely that the NR caps are supplied by the InSb substrate.

To quantify the influence of the InSb supply on NR nucleation and evolution, we plot d/d_0 as a function of irradiation time for both InSb substrates and InSb/GaAs

heterostructures. For irradiation of InSb substrates, d/d_0 decreases from 0.75±0.04 to 0.18±0.06. On the other hand, for irradiation of InSb/GaAs heterostructures, d/d_0 initially decreases, similar to NR behavior on InSb substrates; however, as the the InSb is milled away, d/d_0 starts to increase, coincident with the onset of NR shrinkage. This increasing d/d_0 is due to the suppressed In and Sb mass transport from GaAs surfaces, and suggests that the substrate is the primary source of In and Sb for the NRs.

5.7 Mechanisms for NR growth

Ion-induced NR formation is often explained in the context of the self-sustained etch masking model, which considers NR caps serving as etch masks which are re-supplied by ion-enhanced diffusion.. However, this model cannot explain the formation of NR on III-V compound surfaces in which the sputtering yield of Group III elements typically greater than that of a III-V compound. Furthermore, this model cannot explain the NR shape which typically consists of NR bodies with diameters much larger than those of the NR caps. Here, we consider possible mass transport mechanisms supplying the NR caps, including ion-enhanced diffusion and redeposition. First, we consider ion-enhanced diffusion via a comparison of the NR height with ion-enhanced diffusion lengths. To determine the ion-enhanced diffusion lengths, we consider the RPSDs of SEM images of irradiated InSb and InSb/GaAs surfaces, shown in Fig. 5.7. For surfaces with coarsened In islands and/or NRs, RPSDs of InSb and InSb/GaAs surfaces show a maximum at a spatial frequency of 4×10^{-4} nm^{-1}. Thus, we estimate inter-island spacings, L ~ 364 nm, and ion-enhanced diffusion lengths of L/2 ~180 nm.[28] On the other hand,

the NR heights range from 270 to 2800 nm, which is one order of magnitude larger than the ion-enhanced diffusion length; thus, ion-enhanced diffusion is likely insufficient to resupply the NR caps.

Since the source of In and Sb for the cap affects the NR growth rate, we discuss the role of redeposition on cap resupply in term of the NR growth rate. Assuming that all sputtered substrate atoms are redeposited, the growth rate (shrinkage rate) of NRs on InSb (GaAs) surfaces is approximated as

$$M_{substrate} - M_{NR} + A_{redeposition} \quad (5.1)$$

where $M_{substrate}$ and M_{NR} are the milling rate of the substrate and NRs, respectively, and $A_{redeposition}$ is the accumulation rate of the redeposited atoms. Since the NRs on InSb (GaAs) surfaces consist of InSb bodies with (without) In caps, we use milling rates of InSb (GaAs) for $M_{substrate}$, the milling rate of In (InSb) for M_{NR}, and the accumulation rate of redeposited atoms from InSb (GaAs). The milling rate (accumulation rate) is equal to $f \cdot Y/\rho$ (R/ρ) where f is ion flux, Y is the sputtering yield, ρ is the atomic density and R is the redeposition flux.[29,30] Y_{In} was determined using SRIM simulations; Y_{GaAs} and Y_{InSb} were determined experimentally using a volume loss analysis of AFM images of irradiated GaAs and InSb surfaces.[17,31] The calculated growth (shrinkage) rates for NRs on InSb (GaAs) surface are 1.9±0.2 nm/s (1.3±0.1 nm/s), similar to the measured values of 3.9±0.4 nm/s (2.9±0.2 nm/s). Therefore, re-deposition is considered to be the dominant mechanism of NR growth. We note here that our calculated growth and shrinkage rates are about 50% lower than that of our measured values. This difference is likely due to the fact that we consider redeposition of the atoms sputtered from the substrate surface, but not those sputtered from the NR body.

5.8 Summary and conclusions

In summary, we have examined the formation and evolution of ion-irradiation-induced nanorods (NR) through a comparison of FIB irradiation of InSb substrates and InSb/GaAs heterostructures. On both irradiated InSb surfaces, hillocks and In islands evolve to cone-shaped NRs capped with In islands. For InSb surfaces, NR base diameter increases with ion energy. In the case of InSb/GaAs structures, as the milled depth approaches the InSb/GaAs interface, the cone-shaped NRs transition to capless NRs with a truncated cone shape. In addition, the calculated growth (shrinkage) rates for NRs on InSb (GaAs) surface, including the contribution from redeposition, are similar to the measured values. Therefore, re-deposition is considered to be the dominant mechanism of NR growth. These results suggest a growth mechanism in which both the NR cap and body are primarily supplied by redeposition of atoms sputtered from the InSb substrate. However, to more accurately quantify the NR growth process, redeposition of the atoms sputtered from the NR body also need to be considered. Therefore, ion irradiation of semiconductors provides a promising approach to the fabrication of vertically aligned InSb NR arrays with tunable cone shapes, which are needed for the development of applications such as field-emission devices.[32] Although InSb has the highest intrinsic electron mobility among III-V semiconductors, further work is needed to improve the crystallinity of these ion-induced cone-shaped NRs.

5.9 Figures and References

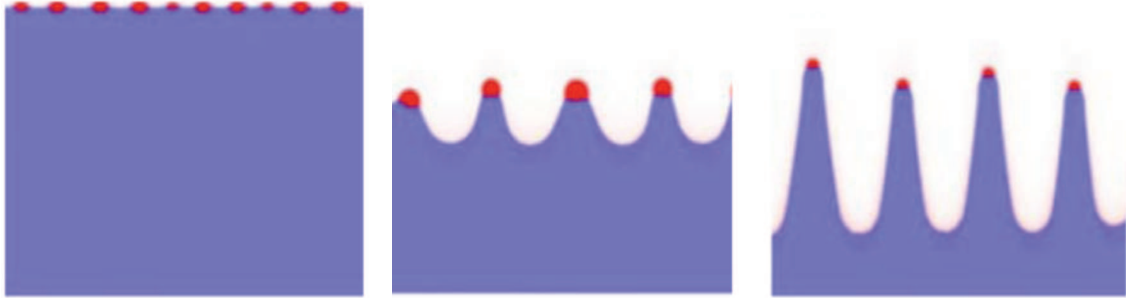

Figure 5.1 Illustration of the surface evolution for increasing irradiation time, Ga is represented in red/dark gray and GaSb is light blue/light gray. Reprinted figure with permission from J S. Le Roy and E. Søndergård, I. S. Nerbø and M. Kildemo, and M. Plapp, Phys. Rev. B 81, 161401 (2001). Copyright 2012 by American Physical Society.

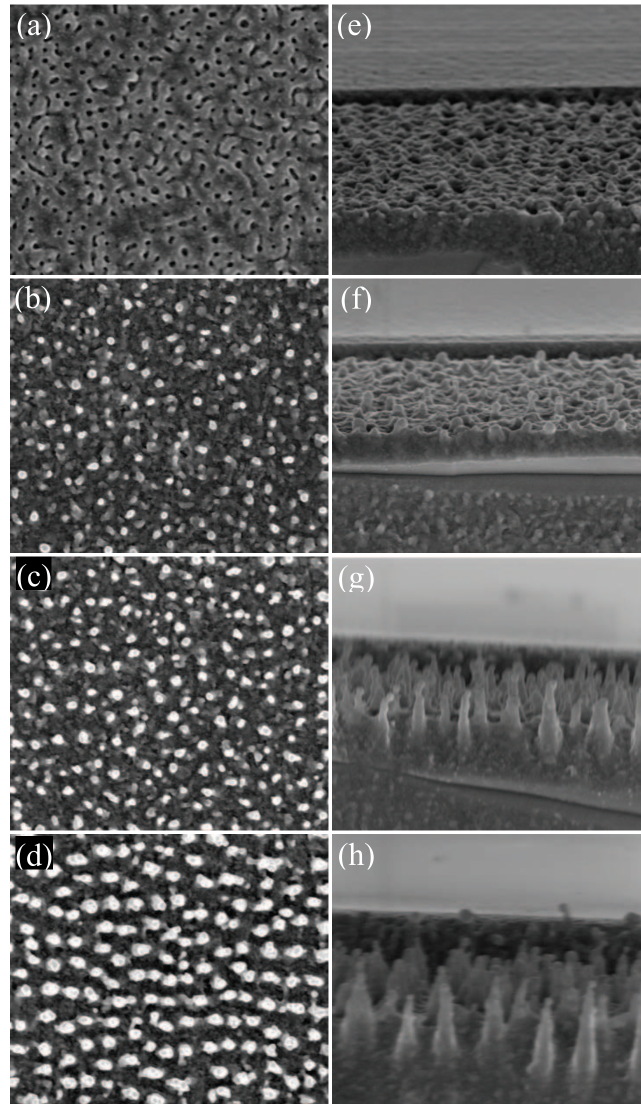

Figure 5.2 SEM images of dose dependence of surface evolution, including hillocks/pits and nanodots at (a), (e) for dose of 1 $\times 10^{16}$ cm^{-2}; coarse nanodots shown at (b), (f) for dose of 3.1 $\times 10^{16}$ cm^{-2}; nanorods capped with nanodots at (c), (g) for dose of 6.9 $\times 10^{16}$ cm^{-2}, and at (d), (h) for dose of 1.4 $\times 10^{16}$ cm^{-2}. Images (a)-(d) ((e)-(h)) were collected with 52° (normal) angle of incidence. Reprinted figure with permission from J. H. Wu, and R. S. Goldman, Appl. Phys. Lett. 100, 053103 (2012). Copyright 2012 by American Institute of Physics.

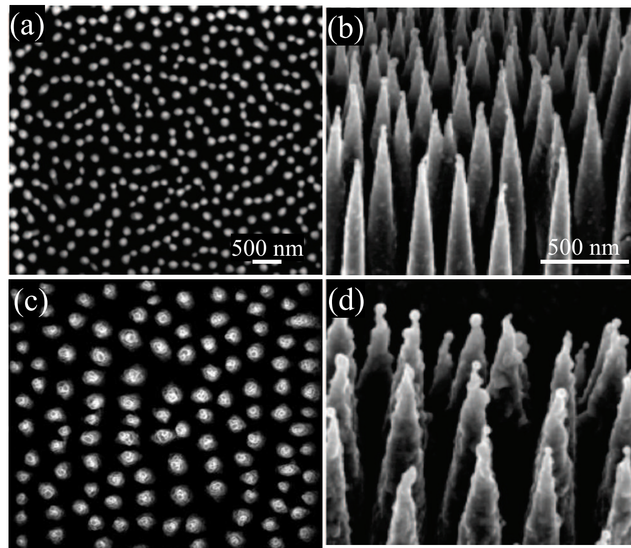

Figure 5.3 (a) and (b) ((c) and (d)) show SEM images of NRs formed on the InSb wafer irradiated with 10 kV (30 kV) ions, respectively. Images (a) and (c) ((b) and (d)) were collected with 0° (75°) angle of incidence. Reprinted figure with permission from J. H. Wu, and R. S. Goldman, Appl. Phys. Lett. 100, 053103 (2012). Copyright 2012 by American Institute of Physics.

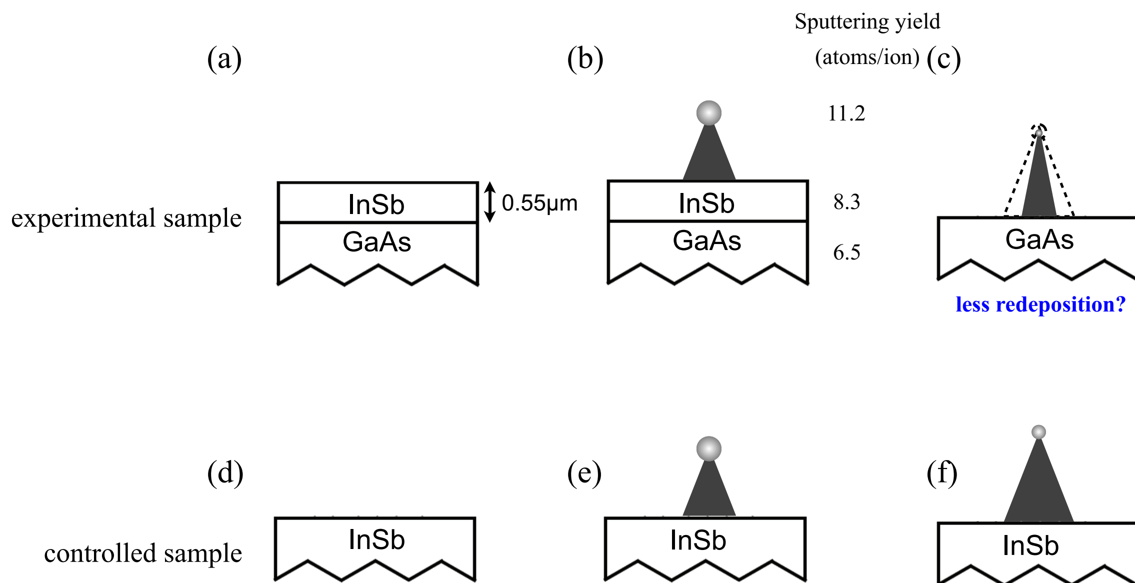

Figure 5.4 Illustrations of nanorod formation on (a)-(c) InSb/GaAs heterostructure and (d)-(f) InSb wafer samples.

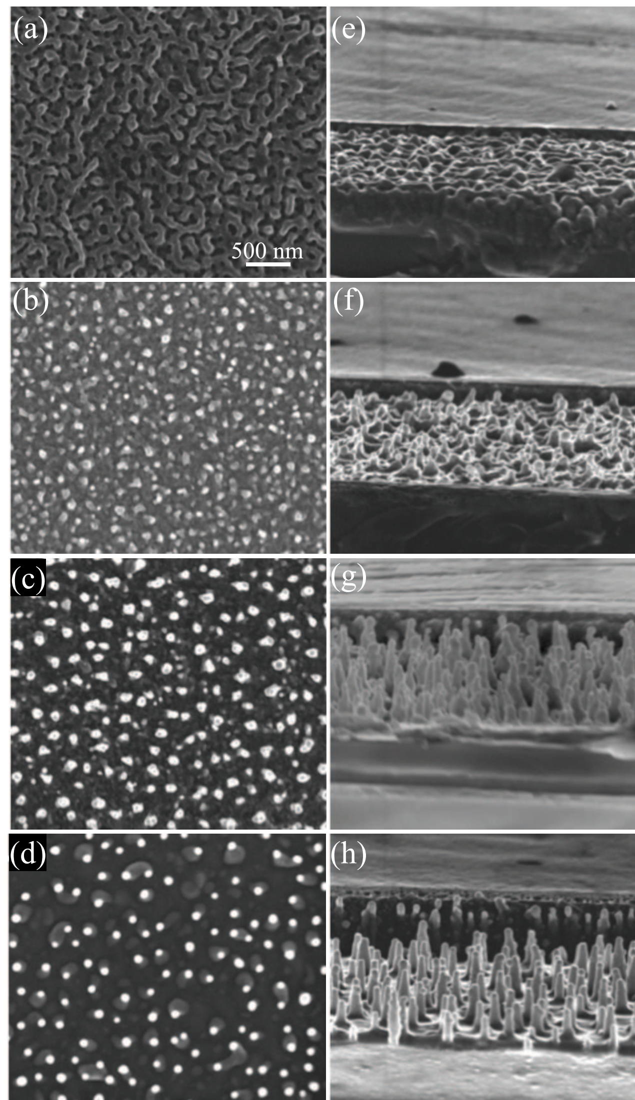

Figure 5.5 SEM images of dose dependence of the InSb/GaAs heterostructure surface evolution, including hillocks and nanoclusters at (a), (e) for dose of 1 $\times 10^{16}$ cm^{-2}; coarse nanoclusters shown at (b), (f) for dose of 3.1 $\times 10^{16}$ cm^{-2}; NRs capped with nanoclusters at (c), (g) for dose of 6.9 $\times 10^{16}$ cm^{-2}; capless truncated-cone NRs at (d), (h) for dose of 1.4 $\times 10^{16}$ cm^{-2}. Images (a)-(d) ((e)-(h)) were collected with 0° (75°) angle of incidence. Reprinted figure with permission from J. H. Wu, and R. S. Goldman, Appl. Phys. Lett. 100, 053103 (2012). Copyright 2012 by American Institute of Physics.

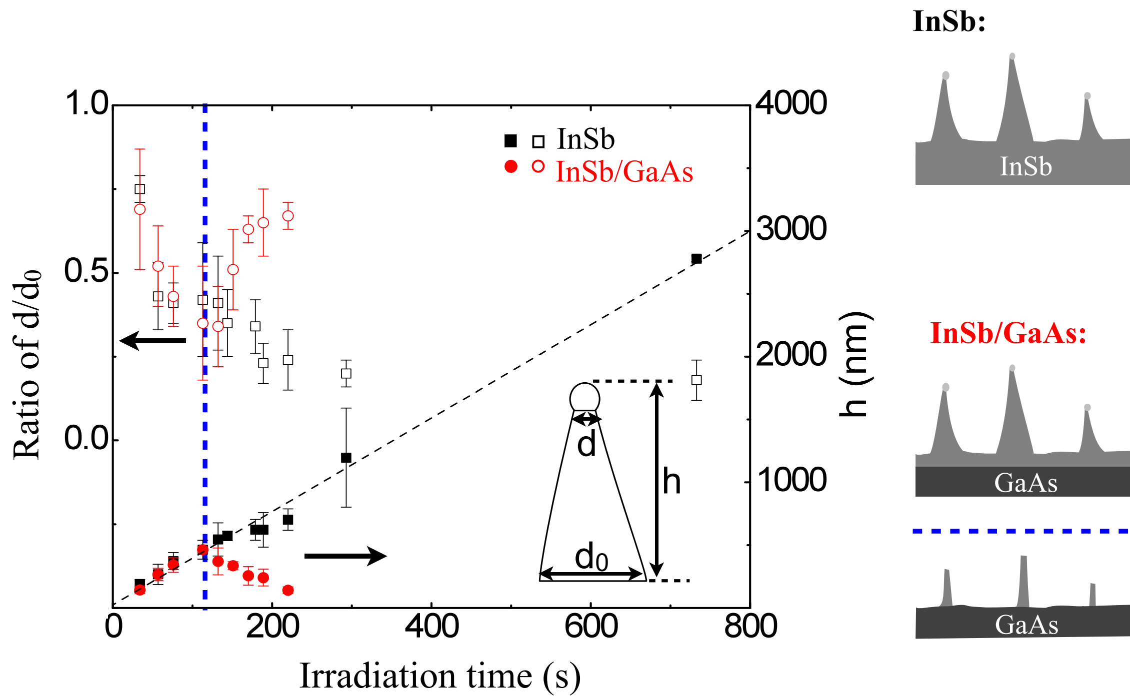

Figure 5.6 The height h, and the ratio of top diameter (d) to base diameter (d_0) of NRs on InSb wafer (InSb/GaAs heterostructures) for ion fluence of 3.1×10^{16} cm^{-2} and 7×10^{17} cm^{-2} (3.1×10^{16} cm^{-2} and 2.1×10^{17} cm^{-2}), and the corresponding illustrations of NR evolution on both samples. Linear least-square fits to the t-dependence of h of NRs are shown. Reprinted figure with permission from J. H. Wu and R. S. Goldman, Appl. Phys. Lett. 100, 053103 (2012). Copyright 2012 by American Institute of Physics.

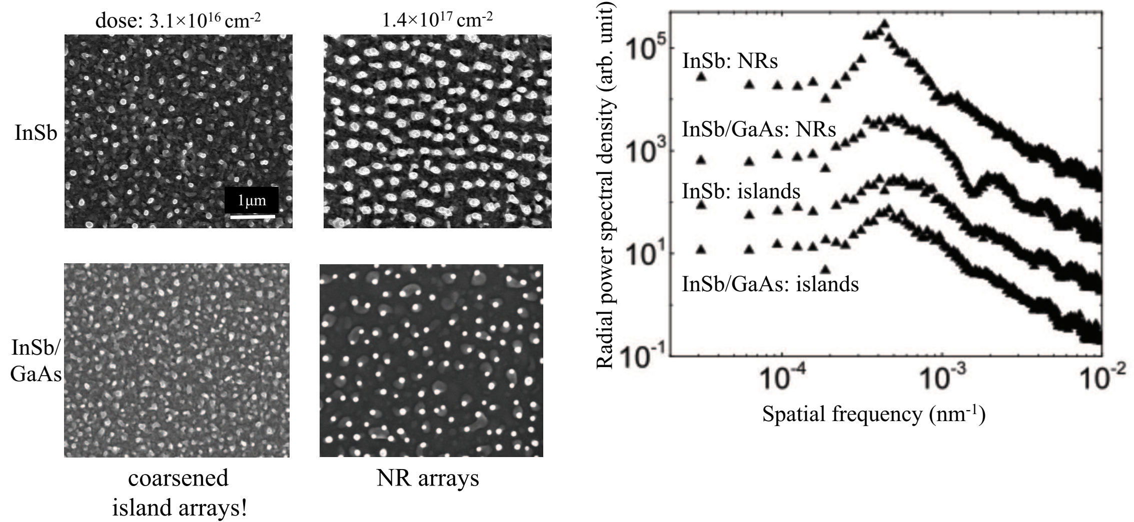

Figure 5.7 Radially-averaged power spectral density (RPSD) vs. frequency obtained from SEM images of irradiated InSb wafer and InSb/GaAs with ion fluence from 3.1×10^{16} cm^{-2} and 1.7×10^{17} cm^{-2}, and the corresponding SEM images of irradiated surfaces of InSb wafer and InSb/GaAs . Reprinted figure with permission from J. H. Wu and R. S. Goldman, Appl. Phys. Lett. 100, 053103 (2012). Copyright 2012 by American Institute of Physics.

[1]N. Mingo, Appl. Phys. Lett. **84,** 2652 (2004).

[2]N. G. Shang, F. Y. Meng, F. C. K. Au, Q. Li, C. S. Lee, I. Bello, and S. T. Lee, Adv. Mater. **14,** 1308 (2002).

[3]A. I. Persson, M. W. Larsson, S. Stenstrom, B. J. Ohlsson, L. Samuelson, and L. R. Wallenberg, Nature Materials **3,** 677 (2004).

[4]A. I. Hochbaum and P. D. Yang, Chem. Rev. **110,** 527 (2010).

[5]L. Hong, Z. Liu, X. T. Zhang, and S. K. Hark, Appl. Phys. Lett. **89,** 193105 (2006).

[6]S. D. Luo, W. Y. Zhou, W. G. Chu, J. Shen, Z. X. Zhang, L. F. Liu, D. F. Liu, Y. J. Xiang, W. J. Ma, and S. S. Xie, Small **3,** 444 (2007).

[7]X. Y. Yang, G. M. Wang, P. Slattery, J. Z. Zhang, and Y. Li, Crystal Growth & Design **10,** 2479 (2010).

[8]J. H. Seol, A. L. Moore, S. K. Saha, F. Zhou, L. Shi, Q. L. Ye, R. Scheffler, N. Mingo, and T. Yamada, J. Appl. Phys. **101** (2007).

[9]R. S. Wagner and W. C. Ellis, Appl. Phys. Lett. **4,** 89 (1964).

[10]J. Kato, M. Nozu, Y. Fujimoto, M. Tanemura, and F. Okuyama, J. Vac. Sci. Technol. A **13,** 207 (1995).

[11]S. Le Roy, E. Barthel, N. Brun, A. Lelarge, and E. Sondergard, J. Appl. Phys. **106,** 5 (2009).

[12]A. D. G. Stewart and M. W. Thompson, J. Mater. Sci. 4, 56 (1969).

[13]M. Tanemura, S. Aoyama, Y. Fujimoto, and F. Okuyama, Nucl. Instrum. Methods Phys. B **61,** 451 (1991).

[14]Y. Yuba, S. Hazama, and K. Gamo, Nucl. Instrum. Methods Phys. B **206,** 648 (2003).

[15]A. G. Perez-Bergquist, K. Li, Y. W. Zhang, and L. M. Wang, Nanotechnology **21,** 6 (2010).

[16]M. Kang, J. H. Wu, W. Ye, M. V. Warren, S. Huang, Y. Jiang, E. A. Robb, and R. S. Goldman**,** Appl. Phys. Lett., 101, 082101 (2012).

[17]J. G. Pellerin, D. P. Griffis, and P. E. Russell, J. Vac. Sci. Technol. B **8,** 1945 (1990).

[18]S. Le Roy, E. Sondergard, I. S. Nerbo, M. Kildemo, and M. Plapp, Phys. Rev. B **81,** 4 (2010).

[19]K. A. Grossklaus and J. M. Millunchick, Nanotechnology **22,** 7 (2011).

[20]K. A. Grossklaus and J. M. Millunchick, J. Appl. Phys. **109,** 11 (2011).

[21]S. Morishita, Y. Fujimoto, and F. Okuyama, Surf. Sci. **202,** L587 (1988).

[22]S. Morishita and F. Okuyama, J. Vac. Sci. Technol. A **8,** 3295 (1990).

[23]S. Morishita and F. Okuyama, J. Vac. Sci. Technol. A **9,** 331 (1991).

[24]X. Weng, N. G. Rudawski, P. T. Wang, R. S. Goldman, D. L. Partin, and J. Heremans, J. Appl. Phys. **97,** 7 (2005).

[25]B. Ziberi, F. Frost, T. Hoche, and B. Rauschenbach, Phys. Rev. B **72,** 7 (2005).

[26]Please see Chapter1 for the details of ion energy dependend of the sputtering yield.

[27]J. H. Wu, W. Ye, B. L. Cardozo, D. Saltzman, K. Sun, H. Sun, J. F. Mansfield, and R. S. Goldman, Appl. Phys. Lett. **95,** 3 (2009).

[28]H. R. Kaufman and R. S. Robinson, J. Vac. Sci. Technol. **16,** 175 (1979).

[29]T. Ishitani and T. Ohnishi, J. Vac. Sci. Technol. A **9,** 3084 (1991).

[30]To calculate the accumulation rate of redeposited atoms from InSb (GaAs), we assume that the III/V ratio of sputtered atoms is 1, and $\rho = 0.5\rho_{III} + 0.5\rho_{V}$ where ρ_{III} and ρ_{V} are the atomic density of III and V elements, respectively.

[31]J. F. Ziegler, J. P. Biersack, and U. Littmark, *The Stopping and Range of Ions in Matter* (Pergamon, New York, 1985).

[32]G. Fursey, *Field Emission in Vacuum Microelectronic* (Kluwer Academic / Plenum Publishers, New York, 2005).

CHAPTER 6

Summary and Suggestions for Future Work

6.1 Summary

Ion beam sputtering-induced surface pattern formation has the potential to become a cost-effective method for rapid fabrication of large-area nanostructure arrays with dimensions below the limits of conventional photolithography. However, ion-sputtering induces nanostructure formation on elemental surfaces only in the presence of impurities. Alternatively, ion sputtering on III-V surface is intrinsically anisotropic, providing an opportunity for ion-sputtering induced nanostructure array fabrication. In this thesis, the formation and coarsening mechanisms of Ga droplets on Ga^+ focused ion beam (FIB) irradiated GaAs surfaces, and the possible driving forces of the Ga droplet motion were investigated and discussed. In addition, we have examined the formation mechanisms of the nanorods (NRs) and ripples on the FIB irradiated InSb surfaces.

In Chapter 3, we investigated the formation, growth and motion of Ga droplets on FIB irradiated GaAs surfaces. We propose a droplet formation and coarsening mechanism consisting of diffusive growth, followed by coalescence via droplet motion (dynamic coalescence) or ripening. Ultimately, the mechanism of droplet formation

implies that altering the binding energy of the substrate by using different materials can alter the type of nanostructure grown.[1] In addition, we identified the steady state regime for droplet motion and examined the relative roles of FIB scanning and thermal gradients on droplet motion. The anisotropic net droplet motion during irradiation, and asymmetric shape of droplets in motion suggest that droplet motion may be driven by FIB-induced composition gradients.

In Chapter 4, we examined the formation and evolution of ripples on FIB irradiated InSb surfaces. Using normal-incidence Ga^+ FIB irradiation of InSb, the local beam incidence angle (θ_{eff}) was tuned by varying the distance between beam spots (pitch) and/or the dwell time. With increasing θ_{eff}, the surface morphology evolves from pits to ripples to featureless surfaces. Continued irradiation of the rippled surfaces leads to island formation on the ripple crests, followed by nanorod growth. This ripple-nanorod transition, triggered by preferential sputtering and island-induced-self-shielding, provides a new approach for achieving dense arrays of nanorods.

In Chapter 5, we examined the influence of ion fluence, ion energy, and InSb source on the NR formation. We consider ion-enhanced diffusion as the dominant mass transport mechanism by comparing the ion-enhanced diffusion length with the NR height. Since the NR height is an order of magnitude larger than the estimated ion-enhanced diffusion length, ion-enhanced diffusion is likely insufficient to resupply the NR caps. We then consider the influence of redeposition on NR growth rate, assuming that the NR cap and body are primarily re-supplied by redeposition of atoms sputtered from the substrate. The calculated growth (shrinkage) rates for NRs on InSb (GaAs) surface are similar to the measured values, suggesting that redeposition plays a key role in ion-

induced NR growth. The ~50% variation between the observed and calculated values might be due to the additional contribution of redeposition of atoms sputtered from the NR body.

6.2 Suggestions for future work

In this thesis, we investigated the formation mechanisms of FIB-induced Ga droplets and NRs, revealing new insights into ion sputtering-induced surface modification. Here, we suggest several avenues for using this knowledge towards practical applications. First, we propose an embedded Ga droplet structure, which can enhance energy transfer between free carriers in GaAs and the Ga surface plasmons. In the following, we present preliminary results toward this goal. We then discuss the possible role of ion-induced NRs in high efficiency thermoelectrics, including preliminary studies of their electrical properties.

6.2.1 Embedded Ga droplets for plasmonics

Metallic nanoparticles (NPs), such as Au, Ag, Al, and Ga, which have potential applications in surface-enhanced spectroscopies,[2] biological and chemical sensing,[3] lithographic fabrication,[4,5] and plasmon-enhanced photovoltaics.[6-9] For plasmonics, Ga NPs have shown several advantages over Au and Ag NPs, including wide spectral tunability, and phase stability across a wide temperature range.[5,9-12] To date, the main approach used to fabricate Ga nanoparticles have been fabricated via exposure of GaN and GaAs surfaces to a Ga molecular beam.[13] Although surface plasmon resonances

from Ga NPs have been demonstrated using GaN:Ga fabricated with molecular beams, limited control over Ga droplet sizes, and size distribution, and arrangements was observed.[10,12,14] As discussed in Chapter 3, we have demonstrated control of Ga droplet sizes and arrangements of Ga droplets using FIB-irradiation of GaAs surfaces.[15] In the following, we discuss progress towards fabricating embedded GaAs:Ga droplet arrays with enhanced PL efficiency of GaAs.

6.2.1.1 GaAs overgrowth on Ga droplet arrays

To date, we have demonstrated the overgrowth of a GaAs cap atop Ga droplet arrays. To preserve the Ga droplets during the GaAs capping layer growth, we used a low substrate temperature (300°C) and high As flux (1.9×10^{-5} torr), similar to an earlier report.[16] In Ref. 15, it was shown that low substrate temperature and high As flux growth conditions resulted in an embedded GaAs structure containing liquid Ga, presumably due to Ga droplet crystallization initiated at the edge of the droplets, followed by GaAs growth along the droplet periphery until the droplets are completely covered with GaAs.[16-18]

Schematics of droplet arrays before and after GaAs growth, with corresponding AFM images of the GaAs surfaces for post-FIB irradiation (post-GaAs overgrowth) are shown in Figs. 6.1 (a) and (b) ((c) and (d)). As shown in Fig. 6.1 (b), hexagonal arrays of Ga droplets were prepared, using the process described in Ch. 2.2, resulting in diameters of 40 ± 10 nm, heights of 8 ± 0.6 nm and inter-droplet spacings of 72 nm. Following GaAs overgrowth, the diameter and height of the features slightly increase to 45 ± 10 nm

and 8 ± 0.6 nm, respectively, as shown in Fig. 6 (d). Interestingly, the arrangement of droplets and the inter-droplet spacing remain constant, suggesting that the droplets have been preserved. To fabricate multilayers of embedded Ga droplets, the first GaAs cap layer must be sufficiently smooth/flat to enable the fabrication of the next GaAs droplet layer. Thus, study of the influence of the GaAs cap layer thickness on the surface roughness is recommended.[19]

6.2.1.2 Photoluminescence of the embedded Ga droplet arrays

To examine the influence of embedded Ga droplet arrays on GaAs photoluminescence, we compared a structure with and without an embedded droplet array, as shown in Figs. 6.2(a) and (b). In Fig. 6.2(c) the PL spectra of the GaAs/Ga/GaAs structure (solid line) and a GaAs/GaAs structure (dotted line) are compared. The PL spectrum from the GaAs/GaAs structure shows peaks at 1.49 eV and 1.51 eV, which correspond to the donor-acceptor pair emission and band to band emission of GaAs, respectively.[20-22] Interestingly, for the GaAs/Ga/GaAs structure, the PL spectrum shows emissions with the same energy but higher intensities, suggesting an enhancement of PL efficiency induced by the Ga droplet arrays. To quantify the PL enhancement, we define a "PL enhancement ratio" as the ratio of the integrated PL intensity from the droplet-covered GaAs to that of the droplet-free GaAs. We determined PL enhancement ratios of 1.3 for the donor-acceptor pair emission at 1.49 eV (829 nm) and 2 for the band to band emission at 1.51 eV (819 nm).

As discussed in Section 3.5, a polycrystalline Ga-rich layer, which may contribute

to non-radiative recombination, is typically observed between the Ga droplets and GaAs substrate, as shown in Fig. 3.11. Therefore, further increases to the PL enhancement ratio may be possible via annealing of the GaAs/Ga/GaAs structure. Therefore, investigations of the influence of the annealing on the PL efficiency of this structure are recommended. In addition, although the RMS roughness of the GaAs/GaAs sample is typically 2.3 nm, that of the GaAs/Ga/GaAs is 4.2 nm. Thus, measurements of the reflected PL power from both samples are needed for quantitative normalization of the PL intensity.

6.2.2 Ion-induced nanorods targeting high efficiency thermoelectrics

The performance of thermoelectrics (TE) is quantified by the figure of merit, ZT, defined as $S^2\sigma T/\kappa$ where σ is the electrical conductivity, κ is thermal conductivity, and S is the Seebeck coefficient.[23,24] Indeed, the highest figure of merit of commercial TEM materials is ~1. Dimensionally-confined materials, such as semiconductor NRs, are predicted to exhibit greatly enhanced thermoelectric (TE) performance due to changes in their electronic band structure which would allow both energy filtering and enhanced phonon scattering.[23-28] For example, since σ depends on the electronic density of states (DOS) and S depends on the energy derivative of the DOS near the Fermi energy, sharp increases in the DOS due to the electronic confinement may significantly improve ZT.[25]

Among III-V compound semiconductors, InSb is the most promising candidate for thermoelectric (TE) applications due to its high electron mobility and low electron effective mass. In addition, for a NR diameter of 15 nm, InSb NWs are predicted to result in ZT > 3.[26] To date, InSb NRs have not yet demonstrated the expected enhanced

TE performance, presumably due to the challenges in controlling the composition and dopant distribution, using standard NR growth techniques. For example, InSb NRs synthesized via a vapor-liquid-solid method show low S and high σ compared to those of bulk InSb crystal, presumably due to unintentional doping from the In and Sb source materials in CVD environment.[29]

In Chapter 5, we demonstrated a promising new approach to fabricate InSb NRs for thermoelectrics. Our method is based upon Ga^+ focused-ion-beam-irradiation of InSb surfaces. To date, we have tuned the diameter, aspect ratio, and density of NRs using various ion energies. For example, Figure 6.3 shows a SEM image of InSb NR arrays, with average NR length ~ 7.2 ± 1.4 ∝m. Figure 6.4 shows HRTEM images and corresponding selected area diffraction (SAD) patterns of a 1.2 ∝m-long NR from a dense arrays of NRs, such as those shown in the SEM images in Ch. 5. The SAD of the NR head and body show spotty patterns, shown in Figs. 6.4 (b) and (c), respectively. In addition, Fig. 6.4 (c) indicates that NR body consists of two phases, including single crystal ZB InSb and single crystal orthorhombic In. Thus, to evaluate the potential use of the NRs for thermoelectrics, thermal conductivity and Seebeck coefficient measurements of individual NR is also suggested. For these measurements, individual NRs need to be transferred to a suspended contact pad structure,[28] presumably using a FIB lift-out approach.

To examine the electrical transport properties of the FIB-induced NRs, we used an STM-based I-V measurement carried out in the JEOL 2010F, as described in Section 2.9. Figures 6.3 (a)-(d) and (e)-(h) show I-V characteristic plus post I-V TEM images of the same NR, respectively. Figure 6.3 (a) and (e) show an initial I-V measurement and the

corresponding post I-V TEM image, respectively. The rectifying nature of the I-V characteristic Fig. 6.3 (e) might suggest the formation of a p-n junction; however, since I is symmetric about V = 0, issues with ohmic vs. Schottky contact formation need to be considered.[30] We also considered the influence of the I-V measurement on the NR structure. Figure 6.4 presents a series of sequentially I-V characteristics and corresponding bright-field TEM images collected immediately following the I-V measurement. Following the initial I-V measurement shown in Fig. 6.3 (a), the NR structure shown in Fig. 6.3 (e), is similar to that observed in Fig. 6.4 (a), suggesting that the initial I-V measurement has not modified the NR. Although the second I-V measurement, shown in Fig 6.3 (b), also displays rectification, there appears to be telegraph noise in the I-V characteristic.[31] Interestingly, following the second I-V measurement, the NR has developed circular features in the neck region as circled in Fig. 5.7 (f). By the third I-V measurement, a current of ~100nA, modulated by the telegraph noise, is observed. In this case, the head and neck of the NR have mostly disappeared, with filamentary regions, labeled by arrows in Fig. 6.3 (g). Finally, we moved the STM tip to the NR base; the resulting I-V characteristic, shown in Fig 6.3 (d), has become less rectifying with 10 times higher current injection at both positive and negative biases. To clarify the relationship between the nanoscale structural changes, Joule heating, electromigration, and/or telegraph noise, further studies are suggested. For example, collection of NR diffraction patterns during I-V measurements is suggested.

6.3 Figures and References

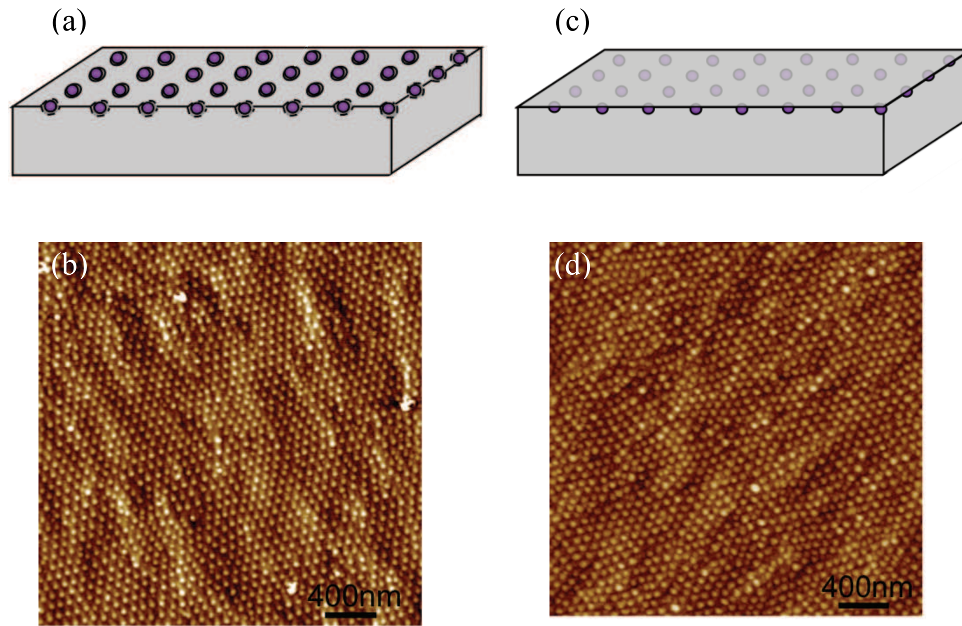

Figure 6.1 Schematic illustrations and the corresponding AFM images of the GaAs surfaces for post-FIB irradiation ((a), (b)) and for post-GaAs overgrowth ((c), (d)).

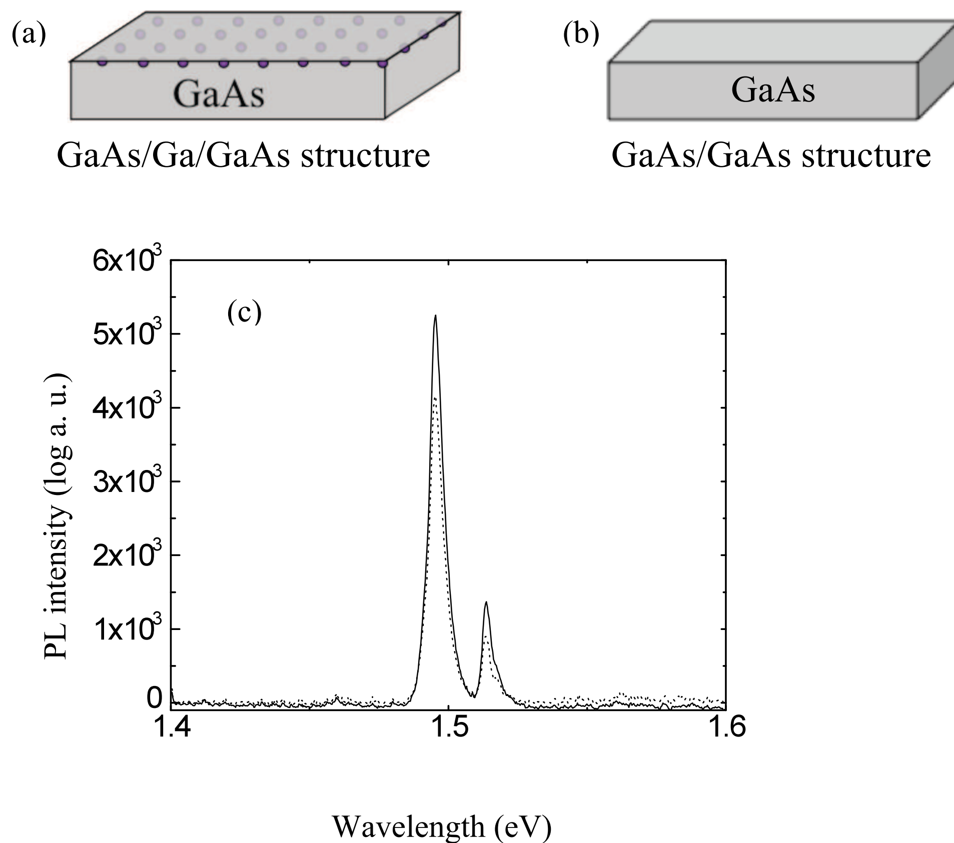

Figure 6.2 (a) Illustration of GaAs/Ga/GaAs structure, (b) illustration of GaAs/GaAs structure (c) the PL spectra of the GaAs/Ga/GaAs structure (solid line) and the GaAs/GaAs structure (dashed line).

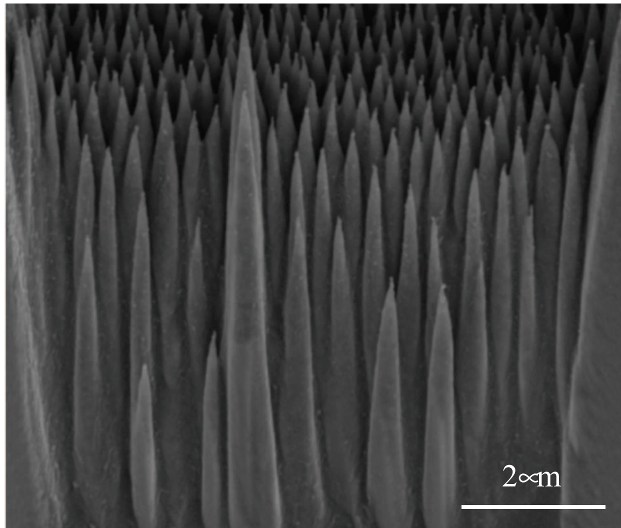

Figure 6.3 SEM image of InSb NR arrays. The average NR height is 7.2 ∝m. This image is a zoom-in view of the NR array shown in Fig. 5.3 (b).

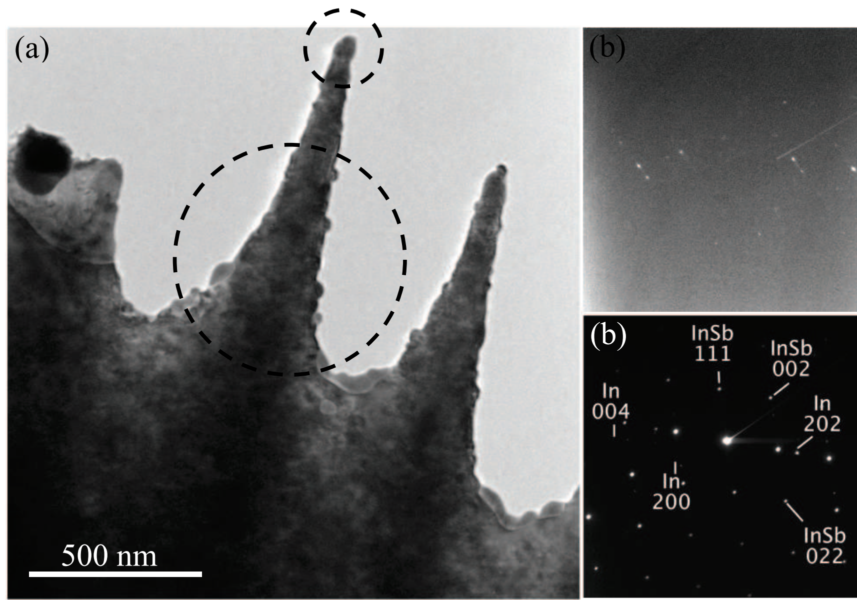

Figure 6.4 (a) TEM images of a 1.4∝m InSb NR; (b) SAD of the head and (c) the body as labeled by the circles in (a).

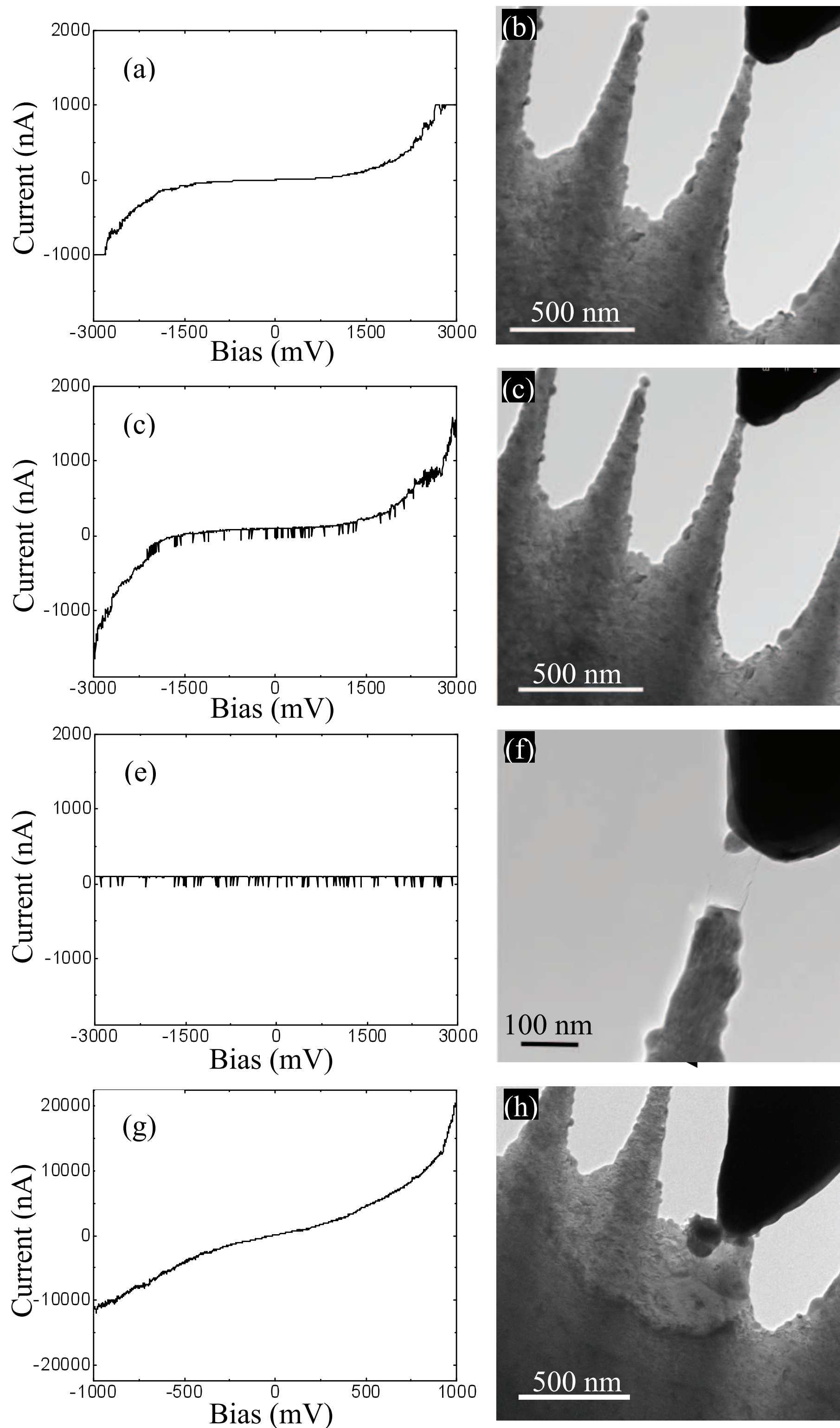

Figure 6.5 IV characteristics of an individual cone-shaped InSb NR and the corresponding post I-V measurement TEM images. (a) and (b) for the first I-V measurement; (c) and (d) for the second I-V measurement; (e) and (f) for the third I-V measurement; (g) and (h) for the fourth I-V measurement.

[1]M. Kang, J. Wu, S. Huang, M. Warren, Y. Jiang, E. Robb, and R. Goldman, Appl. Phys. Lett. **101,** 082101 (2012).

[2]S. M. Nie and S. R. Emery, Science **275,** 1102 (1997).

[3]G. Raschke, S. Kowarik, T. Franzl, C. Sonnichsen, T. A. Klar, J. Feldmann, A. Nichtl, and K. Kurzinger, Nano Lett. **3,** 935 (2003).

[4]W. Srituravanich, N. Fang, C. Sun, Q. Luo, and X. Zhang, Nano Lett. **4,** 1085 (2004).

[5]K. A. Willets and R. P. Van Duyne, in *Annu. Rev. Phys. Chem.*; *Vol. 58* (Annual Reviews, Palo Alto, 2007), p. 267.

[6]H. A. Atwater and A. Polman, Nat. Mater. **9,** 205 (2010).

[7]H. A. Atwater and A. Polman, Nat. Mater. **9,** 865 (2010).

[8]S. Pillai and M. A. Green, Sol. Energy Mater. Sol. Cells **94,** 1481 (2010).

[9]I. M. Pryce, D. D. Koleske, A. J. Fischer, and H. A. Atwater, Appl. Phys. Lett. **96,** 3 (2010).

[10]P. C. Wu, C. G. Khoury, T. H. Kim, Y. Yang, M. Losurdo, G. V. Bianco, T. Vo-Dinh, A. S. Brown, and H. O. Everitt, J. Am. Chem. Soc. **131,** 12032 (2009).

[11]P. C. Wu, M. Losurdo, T. H. Kim, B. Garcia-Cueto, F. Moreno, G. Bruno, and A. S. Brown, J. Phys. Chem. C **115,** 13571 (2011).

[12]P. C. Wu, M. Losurdo, T. H. Kim, M. Giangregorio, G. Bruno, H. O. Everitt, and A. S. Brown, Langmuir **25,** 924 (2009).

[13]Z. Y. AbuWaar, Z. M. Wang, J. H. Lee, and G. J. Salamo, Nanotechnology **17,** 4037 (2006).

[14] M. Kang, T. W. Saucer, M. V. Warren, J. H. Wu, H. Sun, V. Sih, and R. S. Goldman, Appl. Phys. Lett. 101 (2012).

[15]J. H. Wu, W. Ye, B. L. Cardozo, D. Saltzman, K. Sun, H. Sun, J. F. Mansfield, and R. S. Goldman, Appl. Phys. Lett. **95,** 3 (2009).

[16]T. Mano, K. Mitsuishi, Y. Nakayama, T. Noda, and K. Sakoda, Appl. Surf. Sci. **254,** 7770 (2008).

[17]N. Koguchi and K. Ishige, Jpn. J. Appl. Phys. 1 **32,** 2052 (1993).

[18]T. Mano, T. Kuroda, S. Sanguinetti, T. Ochiai, T. Tateno, J. Kim, T. Noda, M. Kawabe, K. Sakoda, G. Kido, and N. Koguchi, Nano Lett. **5,** 425 (2005).

[19]S. Jeon, M. Kang, J. H. Wu, J. Lee, V. Sih, and R. S. Goldman**,** to be submitted.

[20]P. Lautenschlager, M. Garriga, S. Logothetidis, and M. Cardona, Phys. Rev. B **35,** 9174 (1987).

[21]P. W. Yu, D. C. Reynolds, and C. E. Stutz, Appl. Phys. Lett. **61,** 1432 (1992).

[22]T. Obata, S. Fukushima, T. Araya, and N. Otsuka, J. Cryst. Growth **227,** 112 (2001).

[23]G. Chen, M. S. Dresselhaus, G. Dresselhaus, J. P. Fleurial, and T. Caillat, Int. Mater. Rev. **48,** 45 (2003).

[24]M. S. Dresselhaus, G. Chen, M. Y. Tang, R. G. Yang, H. Lee, D. Z. Wang, Z. F. Ren, J. P. Fleurial, and P. Gogna, Adv. Mater. **19,** 1043 (2007).

[25]M. S. Dresselhaus, G. Dresselhaus, X. Sun, Z. Zhang, S. B. Cronin, and T. Koga, Phys. Solid State **41,** 679 (1999).

[26]N. Mingo, Appl. Phys. Lett. **84,** 2652 (2004).

[27]X. Y. Yang, G. M. Wang, P. Slattery, J. Z. Zhang, and Y. Li, Crys. Growth Des. **10,** 2479 (2010).

[28]A. I. Boukai, Y. Bunimovich, J. Tahir-Kheli, J. K. Yu, W. A. Goddard, and J. R. Heath, Nature **451,** 168 (2008).

[29]J. H. Seol, A. L. Moore, S. K. Saha, F. Zhou, L. Shi, Q. L. Ye, R. Scheffler, N. Mingo, and T. Yamada, J. Appl. Phys. **101** (2007).

[30]Thanks for the useful discussion from Yen-Hsiang Lin.

[31]C. L. Kane, Phys. Rev. Lett. **90,** 4 (2003).

APPENDIX A

Ion-Solid Interaction: Calculations

A.1 Overview

In this Appendix, calculations of several parameters describing ion-solid interactions, including ion fluence, sputtering yield, ion flux uniformity, and ion-induced substrate heating, are described. The ion fluence and sputtering yield calculations were used to quantify and compare our experiments with those in the literature. Calculations of ion flux uniformity and ion-induced substrate heating were used to consider the influences of FIB raster scanning and FIB-induced substrate heating on our experiments and conclusions.

A.2 Ion fluence

Ion fluence is defined as the number of ions traversing a unit area,[1,2] as follows:

$$t \cdot i_{Ga} \cdot \left(\frac{6.24 \times 10^{18}}{A}\right) \qquad \text{(A.1)}$$

where i_{Ga} is the current measured in a Faraday cup immediately prior to irradiation, t is the total time for irradiation, and A is the irradiated area measured from either SEM or AFM images following irradiation. The irradiated regions show dramatic morphological changes compared to the un-irradiated changes. This change can be observed from the morphology and color by SEM, and height change from AFM.

A.3 Sputtering yield

The sputter yield, Y, is defined as the number of sputtered atoms per incident ion,[1,2] as follows:

$$Y = \frac{dV}{dQ} \tag{A.2}$$

where V is the volume removed by FIB milling and Q is the ion charge. The milled volume is determined from the AFM following milling, and the ion charge is determined as follows:[3,4]

$$\frac{i_{Ga} \cdot t}{1.6 \times 10^{-19}} \tag{A.3}$$

A.4 Ion flux uniformity

To consider the adequacy of flux uniformity during our FIB irradiation experiments, we calculated the regimes of ion flux uniformity for the beam spot (i.e. pixel) sizes and beam spot overlaps (i.e. pitch) used. Since our FIB system is computer controlled, irradiation is performed by precise pixel-by-pixel movement. To achieve an adequately uniform ion flux over the scanned area, the center-to-center beam spot separation, termed pitch, p, along and across the scan direction must be small enough to allow 50% overlap between adjacent pixels with diameter, d.[5] We note that uniform ion flux means that the ion flux with respect to the scanning direction has to be uniform. Assuming a Gaussian ion distribution within a given pixel,[6] uniform fluxes are predicted for $p/d < 0.64$ in which a proper overlap between adjacent pixels is achieved and a smooth uniform profile can be milled.[5]

For each ion energy and current setting of our experiments, Table A.1 shows the

values of p, d, and the corresponding value of p/d. For droplet and NR formation, 5, 10 and 30 10 kV ions with 50, and 70 pA current, 9, 12.5, and 13 nm P, 19, 41,and 78.8 nm d were used, leading to predicted p/d values ranging from 0.01 to 0.35, thus, the ion fluxes are considered uniform. For the ripple studies, 30kV ions with 50 pA current, 17-4 nm P, and 19 nm d were used, leading to predicted p/d values ranging from 0.21 to 0.89, with periodic features observed for p/d from 0.21 to 0.42. Thus, we concluded that the influence of artifacts from FIB raster scan is negligible in this thesis work.

Table A.1 Table of ion energies, ion currents, pitches, and beam diameters used for fabrication of droplets, nanorods, and ripples. For ratios of p/d < 0.64, uniform fluxes are expected.

Energy (keV)	Current (pA)	p (nm)	d (nm)	p/d	Nanostructures		
					DR	NR	RIP
30	50	17-4	19	0.21-0.89	X	X	X
30	100	8	23	0.35	X		
10	50	12.5	41	0.3	X		X
5	70	13	78.8	0.01	X		

A.5 FIB-induced substrate heating

To estimate the FIB-induced substrate heating, we calculated the maximum temperature rise ($\Delta T_{\max}^{FIB}$) obtained in the center of the beam spot. We assumed a circular beam spot with a Gaussian energy distribution. We also assume a temperature-independent substrate thermal conductivity.[7] Thus, $\Delta T_{\max}^{FIB}$ is estimated as [7,8]

$$\Delta T_{\max}^{FIB} = \frac{\sqrt{\pi} VdJ}{4\kappa} \qquad \text{(A.4)}$$

where eV is the ion energy, d is the beam diameter, J is the beam current density, and κ is the thermal conductivity, listed in Table A.2 for the materials used in this thesis. Using the parameters from Table A.2 and the values of eV and J tabulated in Table A.3, we calculated the $\Delta T_{\max}^{FIB}$ for all irradiation conditions used in this thesis. It is interesting to note that $\Delta T_{\max}^{FIB}$ is predicted to range from 0.01 to 1.32 K, suggesting negligible FIB-induced substrate heating.

Table A. 2 Thermal properties of GaAs, InAs, InSb and Si.[9]

	GaAs	InAs	InSb	Si
Density (g/cm^3)	5.32	5.68	5.775	2.329
Specific heat capacity (J/kg K)	330	250	144	702
Thermal conductivity (W/mK)	55	27	16	124

Table A. 3 FIB-induced temperature rise on irradiated GaAs, InAs, InSb and Si.

Target material	Voltage (V)	Current (nA)	Beam diameter (nm)	Irradiation time (s)	ΔT_{max}^{FIB} (K)
GaAs	5	0.07	78.8	300	0.01
	10	0.05	41	276	0.03
	30	0.05	19	7920	0.2
	30	0.1	23	276	0.33
InAs	30	0.05	19	120	1.32
	30	0.1	23	120	0.68
InSb	10	0.05	41	764	0.11
	30	0.05	19	764	0.7
	30	0.1	23	66	1.15
Si	30	0.05	19	276	0.09

APPENDIX B

Non-equilibrium Clustering Models

This appendix reviews surface clustering models and summarizes the predicted growth rates of clusters in different regimes. Cluster formation is often described by three regimes: nucleation, early stage growth, and late stage growth.[10-15] This treatment is applicable to a non-equilibrium process, for which $C(t) > C_{eq}$, including Ga^+ irradiation of GaAs.[10,11,16] Figure B.1 shows the schematic overview of clustering phenomena on irradiated GaAs surfaces. During the initial irradiation, the surface remains featureless. Above a critical ion dose, droplets are nucleated, and with continued irradiation, droplets start to move, grow and coalesce. The droplet formation process can be described in the context of nucleation and growth governed by the surface supersaturation S(t), defined as $S(t) = [(C(t) - C_{eq})/C_{eq}]$, where C(t) is the total [Ga] concentration and C_{eq} is the bulk Ga solubility in GaAs. During the initial stages of Ga+ ion irradiation of GaAs, the so-called "supersaturation" regime, S(t) increases up to a critical value, Sc, at a time, t_c, after which spontaneous nucleation occurs. During the nucleation process, particles with radius R > Rc grow, while those with R < Rc dissolve. As nucleation is occurring, S(t) decreases, eventually dropping below Sc at a time t_{early}. The region between t_c and t_{early} is usually referred to as the nucleation regime. For t > t_early, S(t) < Sc, and nucleation of new nuclei is inhibited; existing nuclei grow by the incorporation of incoming adatoms. Hence, the number of the nuclei/clusters reaches a steady-state value: N(t)~const.[17]

Meanwhile, adatoms diffuse to the cluster, and contribute to their growth. In this regime, often termed "early stage growth", cluster growth is described in terms of a kinetic rate equation [13,18-20]

$$\frac{dR}{dt} = K_i \frac{(C(t) - C_{eq}(R))}{1 + \varepsilon R} \qquad \text{(B.1)}$$

where K_i is the rate constant for the surface integration of the adatoms, R is droplet radius, and $C_{eq}(R)$ is the equilibrium concentration at the cluster surface, and $\varepsilon = K_i/(D_m \upsilon)$, where υ is the molecular volume of the particles, and D_m is the diffusion coefficient. $C_{eq}(R) = Cs\,(1+\alpha/R)$ where Cs represents the bulk solubility and α is the capillary force. We consider two limits, $\varepsilon R \ll 1$ and $\varepsilon R \gg 1$, both of which lead to a steady-state cluster concentration, N. For $\varepsilon R \ll 1$, growth is limited by monomer incorporation at particle surface, termed the "reaction limited" regime, with $R \propto t$.[10,19,21]

For $\varepsilon R \gg 1$, growth is limited by the diffusion of monomer to the particle surfaces, termed the "diffusion limited" regime, with the particle size, R, proportional to the square root of t. [22,23]

For t > t_late, S(t) < 0; we enter the so-called "late stage growth" regime which is dominated by particle coarsening, such as Ostwald Ripening (OR). During irradiation, mass is not conserved and therefore cluster dissolution may be suppressed, resulting in so-called "second independent growth". Once irradiation is arrested, the Ga adatom supply is suppressed, and the resulting mass is conserved. Similar to the "early stage growth", late stage growth may be either reaction or diffusion limited. In the case of reaction limited growth, both N and R are expected to be proportional to the square root of t. For diffusion-limited growth, N is in the steady-state and R is proportional to the

cubed root of t.

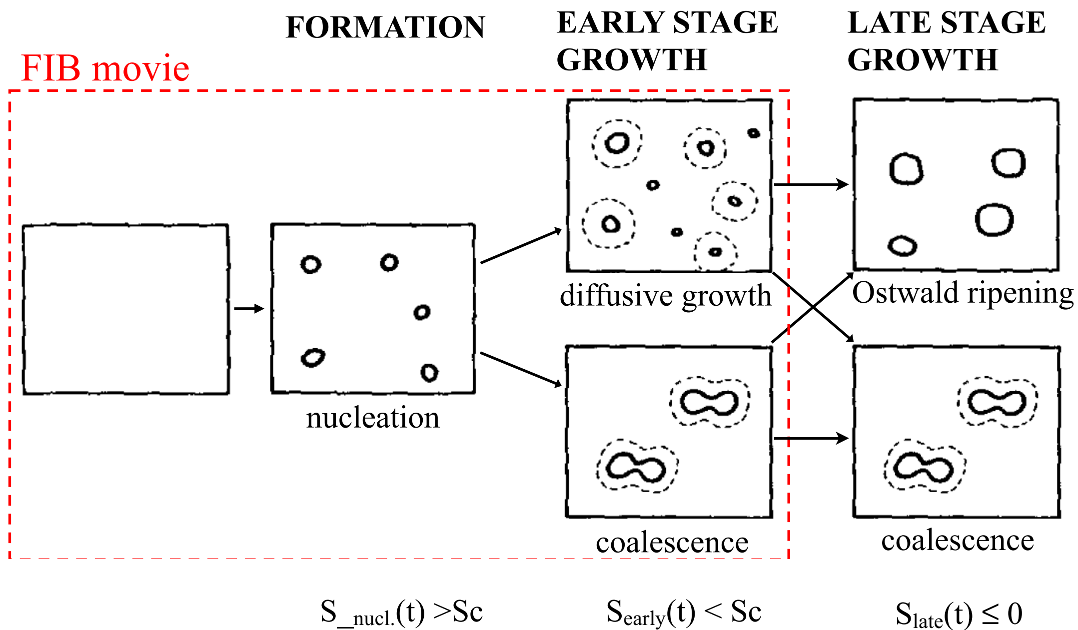

Figure B.1 Application of non-equilibrium clustering process to Ga-irradiation induced Ga droplet formation GaAs surfaces. Three stages are distinguished: formation, early stage growth, and late stage growth. Modifications were made into a reprinted figure with permission from M. Zinke-Allmang, L. C. Feldman, and M. M. Grabow, Surf. Sci. Rep. 16, 377 (1992). Copyright 1992 by Elsevier.

APPENDIX C

Calculations of FIB Irradiation-Induced Surface Ga concentration, C(t)

This appendix describes calculations of FIB irradiation-induced surface Ga concentration, C(t). The total [Ga], C(t), consists of the sum of the implanted [Ga], $C_{impl.}(t)$, plus the so-called "left behind" [Ga] due to preferential sputtering of arsenic, $C_{LB}(t)$. The profile code and SRIM simulations were used to determine $C_{impl.}(t)$ and $C_{LB}(t)$, respectively.

The calculated depth-dependence of the implanted [Ga] in GaAs for both 10 and 30 kV irradiation and an ion fluence of 3.9×10^{16} cm^{-2} is shown in Figure D.1. $C_{impl}(t)$ was determined by the area under the curves in Fig. C.1, resulting in 0.63×10^{16} cm^{-2} (1.11×10^{16} cm^{-2}) for 10 (30) kV irradiation. The $C_{LB.}(t)$ was determined by SRIM simulations. Table D.2 shows the sputtering yield, determined from SRIM simulation, of Ga and As for 10 and 30 kV ion irradiation. The preferential sputtering leads to the generation of 3.66 and 3.24 Ga atoms/ion, hence, the $C_{LB.}(t)$ is 1.26×10^{17} cm^{-2} (1.43×10^{17}cm^{-2}) for 10 (30) kV irradiation. Therefore, for an ion fluence of 3.9×10^{16} cm^{-2}, C(t) is about 16.7% higher for the 30 kV in comparison to the 10 kV case.

Table C.1 Sputtering yields of Ga, and As, and $C_{LB.}(t)$ determined from SRIM simulations. The ion fluence used for calculation is 3.9×10^{16} cm^{-2}.

	30kV	10kV
Y_{Ga} (atoms/ion)	3.09	2.62
Y_{As} (atoms/ion)	6.75	5.86
Y_{Ga}-Y_{As}(atoms/ion)	3.66	3.24
$C_{LB}(t)$ (atoms/cm^{-2})	1.43×10^{17}	1.26×10^{17}

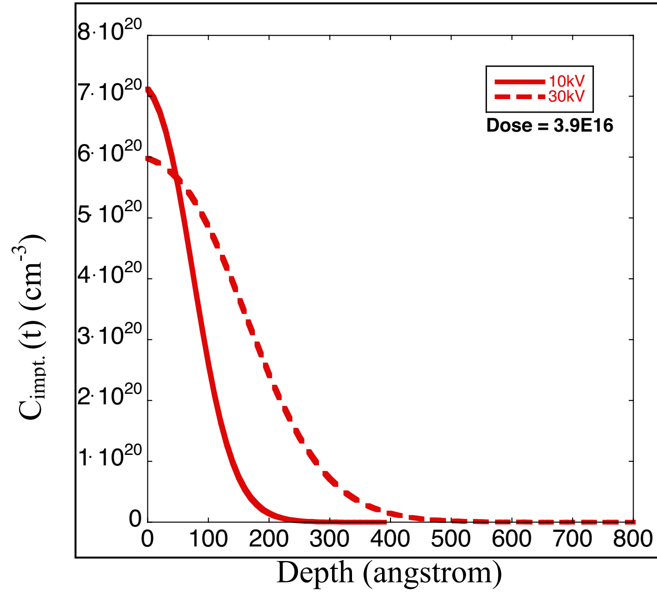

Figure C.1 Ion energy dependent-depth distribution of implanted Ga in GaAs for ion fluence of 3.9×10^{16} cm^{-2}. The solid (dashed) lines are for 10 (30) kV irradiation. The parameters used in the profile code include 10 kV and 30 kV Ga, and 5.315 g/cm^3 of GaAs density and 7.4 atoms/ion of GaAs sputtering yield.

APPENDIX D

Procedure for Determining Ga droplet size

D.1 Overview

This appendix describes the procedures used for determining the size of Ga droplets based on SEM images. For these procedures, the Scanning Probe Image Processor (SPIP) is used to extract line-cuts across possible droplets. The height information is then input into a MATLAB code for analysis.

D.2 Procedure for determining the size of Ga droplets on GaAs

The sizes of Ga droplets on GaAs surfaces were quantified using SEM images collected with 52° angle of electron incidence. First, SEM images consisting of 1024 · 884 pixels were opened in SPIP. The area of interest is selected using the "Rectangular/Zoom" function. Figure D.1 (a) shows an image of Ga droplet arrays on GaAs opened in SPIP, with area of interest, selected with a white box. To determine the height profile of the selected droplet, we perform the "single line profiling" across the center of the selected droplet, which leads to the appearance of a new window named "profiling_file name.prf". Figure D.1 shows (b) a zoomed-in view of the selected droplet including a line-cut across its center, and (c) the corresponding droplet height profile. The height profile data is saved as a .asc file and input into a MATLAB code to determine the first derivative of the height profile. The details of the MATLAB code are

in appendix D.3. For the droplet selected in Fig. D.1, Fig. D.2 shows (a) the height profile as a function of distance and (b) the first derivative of the height profile with respect to distance. The diameter of the droplet is determined by the separation between the outer inflection points in the derivative of the height profile, indicated by the vertical dashed lines in Fig. D.2, using the MATLAB code in Appendix D.3.

D.3 MATLAB code for droplet diameter analysis

Droplet diameter analysis

```
% [size,dz]=dropletsize(x,z)
% x = position along sample surface in nm
% z = surface height based on linecut data in nm
function [size,dz]=dropletsize(x,z)
    %take derivative of height data
    dz=deriv(x,z);
    %find the max and min of the derivative
    dz_max_loc=find(max(dz)==dz);
    dz_min_loc=find(min(dz)==dz);
    %locate left edge
    l_edge=leftedge(x,dz,dz_max_loc);
    %locate right edge
    r_edge=rightedge(x,dz,dz_min_loc);
    size=r_edge-l_edge;
end
```

%Take derivative using a more accurate differential difference. The different difference is the difference between slopes of droplet profiles.

```
function dz=deriv(x,z)

    h=x(2)-x(1);
    dz(1)=NaN;
    for i=2:length(z)-1
        dz(i)=(z(i+1)-z(i-1))/(2*h);
    end
    dz(length(z))=NaN;
end
```

%Find the left edge of the droplet

```
function l_edge=leftedge(x,dz,dz_max_loc)
    %find where dz crosses the x-axis
    i=dz_max_loc;
    while dz(i)>0
        i=i-1;
    end
    pt1=i;
    m=(dz(pt1+1)-dz(pt1))/(x(pt1+1)-x(pt1));
```

```
    l_edge=x(pt1)-dz(pt1)/m;
end
%Find the right edge of the droplet
function r_edge=rightedge(x,dz,dz_min_loc)


    %find where dz cross the x-axis
    i=dz_min_loc;
    while dz(i)<0
        i=i+1;
    end
    pt1=i;
    m=(dz(pt1+1)-dz(pt1))/(x(pt1+1)-x(pt1));
    r_edge=x(pt1)-dz(pt1)/m;
end
```

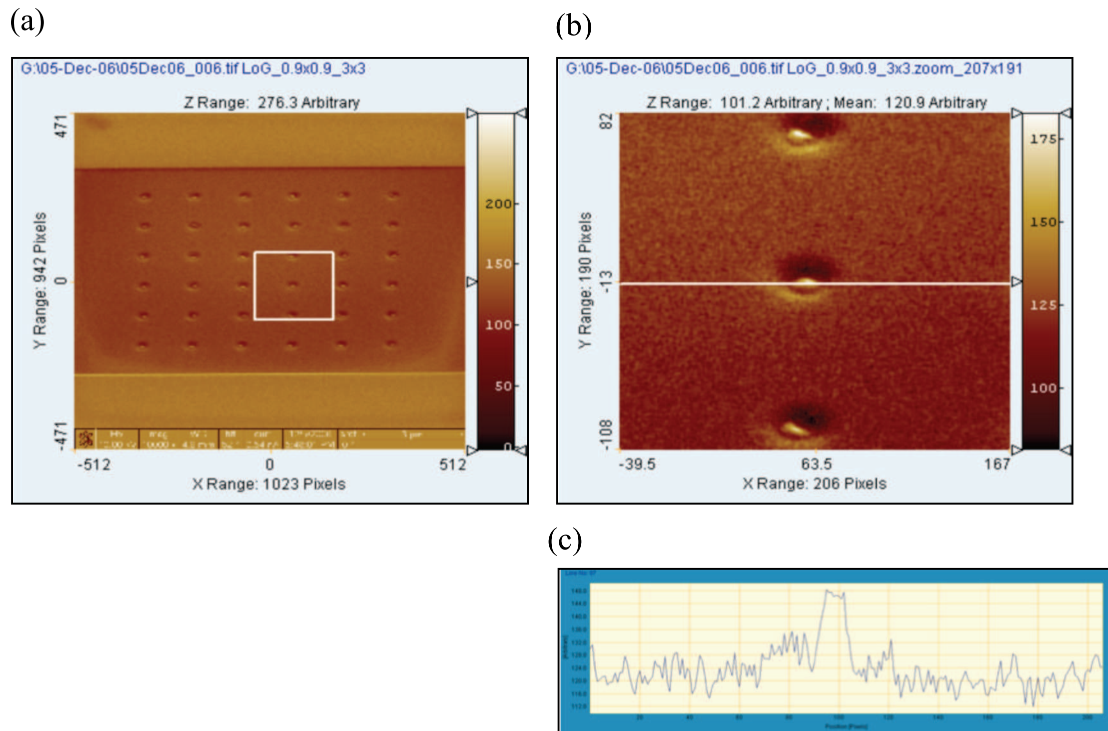

Figure D.1 (a) an SEM image of Ga droplet arrays on GaAs opened in SPIP with the area of interest, selected with a white box; (b) the zoomed in view of the selected droplet with a line-cut across the droplet center; (c) the corresponding height profile for the line-cut through the droplet in (a).

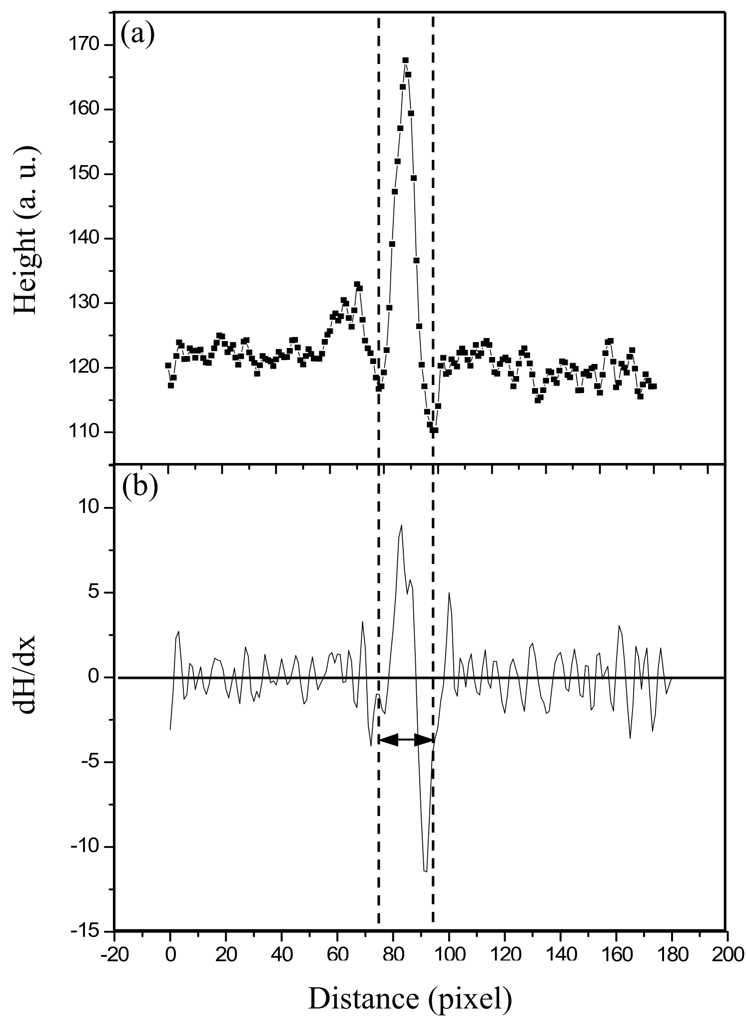

Figure D.2 (a) Height profile of the droplet selected from the image in Fig. D.2; (b) the first derivative of the height profile of the selected droplet. The diameter of the droplets, determined by the distance between the inflection points indicated by vertical dashed lines, in this case, 20.5 pixels.

APPENDIX E

Ga Droplet Motion Tracking

E.1 Overview

This Appendix describes the codes developed in the Interactive Data Language (IDL), utilized to track Ga droplet motion during the real-time movies, described in Sections 2.2 and 3.5. The codes are named "PRO readimage" and "PRO tracking". Both codes were written to input .tif file. We note that both.tif and .jpg mage formats can be produced in the NOVA FIB, but .tif images provide higher image resolution.

E.2 Procedure for droplet identification

First, "PRO readimage" is used to identify the droplets in each image frame via the following steps: (1) displays gray-scale image, (2) smoothes the image, (3) thresholds the image, (4) labels every particle in this image, (5) calculates the index and radius of each particle, and (6) saves the results as a new array, as shown in Fig. E.1. Subsequently, "PRO tracking" is used to track droplets in consecutive image frames, as shown in Fig. E.2. In the PRO readimage code, each droplet is identified in terms of its position (x,y) and radius, assuming that it is circular. Since the droplets are not typically exactly circular, all the pixels within a spot are counted, the center of mass for those pixels is identified, and an equivalent circular region surrounding that center of mass is

then built. In addition, only droplets with lifetime longer than 10 seconds and diameters larger than 24 nm (two pixels) are used for the analysis of droplet size and motion.

E.3 Procedure for droplet tracking

A real-time droplet motion movie with an imaging area of $6.3\times5.4\ \propto m^2$, consisting of 512×440 pixels, was recorded by collecting secondary electrons generated by the Ga ion beam. Figure E.1 shows a flow chart of the processes in “PRO readimage”. Image frames are extracted from the movies every 0.2 s, saved as .tif files, and read by the code, “PRO readimage”, which extracts the data into arrays of gray-scale values. To decrease the noise level, “PRO readimage” smooths the images by subtracting the local background, namely the average of 6x6 pixel arrays. An intensity histogram of the images is then manually (i.e. by the user) used to determine the gray-scale threshold for identification of droplets and background surfaces. The user then compares the droplet sizes and shapes in the processed images. If the processed droplet sizes or shapes deviates from the originals, the smoothing step is re-done with a different pixel array size, such as 8x8 pixel arrays. This process may involve several iterations. Next, the PRO readimage labels each droplet with (#, x, y, r) where # is the frame number, x and y are the positions of the droplet center of mass, and r is the equivalent circular radius of the droplet. Since the droplets are not typically exactly circular, the code first counts up all the pixels in a droplet, identifies the center of mass for those pixels, and then builds an equivalent circular region surrounding that center of mass. Every droplet in each image frame was labeled using this process.

After PRO readimage labels all droplets in each image frame, the indices are used to track the droplet sizes and positions in consecutive frames. Figure B.2 provides an overview of the tasks performed by “PRO readimage”. First, the values of $(|\Delta x|+|\Delta y|+|\Delta r|)$ are calculated between one droplet in the t image frame and all droplets in the t+0.2 image frame. The droplet in the t+0.2 image frame with min value of $(|\Delta x|+|\Delta y|+|\Delta r|)$ is identified as the same droplet, as shown in Fig. E.2 (b). Next, the average speeds of all tracked droplets in all the image frames for a given movie, <v>, is calculated. If the speed of a particular droplet is > 1.5<v> for two consecutive image frames, it is considered “disappeared”, and PRO readimage ceases tracking it, as shown in Fig E.2 (c). Finally, if the fractional change of a droplet size, $\Delta r/r > 2$ for two consecutive frames, the droplet is identified as being merged with a large droplet. At that point, the droplet is considered to be lost, and Pro readimage ceases tracking it.

E.3 IDL codes: These codes, PRO readimage and PRO tracking, are used to identify the droplets in each image frame and to track droplets in consecutive image frames, respectively.

PRO readimage

```
window,xsize=512,ysize=440
Finalarr = make_array(335, 5, 200,/float,value = 0)
for J = 0L, 334L, 1L do begin
filename = STRCOMPRESS('/Applications/IDL/test(.1nA)_154/'+STRING(j)+'.jpg',
/REMOVE_ALL)
```

```
read_jpeg, filename, gray_image

; Smooth and threshold gray scale image

sgi=smooth(gray_image,6,/edge_truncate)

if (j ge 0 and j le 50) then threshImg = smooth(sgi,2,/edge_truncate) GE 193

        sgi=smooth(gray_image,7,/edge_truncate)

        threshImg = smooth(sgi,3,/edge_truncate) GE 195

endif

; Label the particle and display it in window 0

regions = LABEL_REGION(threshImg)

hist = HISTOGRAM(regions)

; define the criterion for particle area and get rid of the small particles, which are likely be
noise

;Plot particle Area Size Distribution histogram

index = where (hist lt 100000 AND hist gt 0)

areas = hist(index)

bin_size=1

ASD=histogram(areas,binsize=bin_size, locations=xbin)

xbin=xbin + bin_size/2.

;Calculate the particle radius and plot a particle radius histogram

radii = (areas/3.14)^0.5

bin_size=1.5

PSD = HISTOGRAM (radii, locations=xbin,max=15, min=0,nbin=10)

xbin=xbin+bin_size/2
```

```
xbin=[min(xbin)-bin_size,xbin]

PSD=[0,PSD]

;To count the particle number of each snapshot

PN = n_elements(index)

; To calculate index of all selected particles in every snapshot

  for i = 1L, PN, 1L do begin

    PI = where (regions eq i, count)

      y =floor (PI/512)

        finalarr[j,2,i] =total(y)/n_elements(y)

          x = (PI-512*y)

        finalarr[j,1,i]=total(x)/n_elements(x)

      finalarr[j,3,i] = (count/3.14)^0.5

     finalarr[j,4,i] = count

    finalarr =i

  endfor

endfor

; to save the finalarr in a new file

save, finalarr, filename = '/Applications/IDL/test(.1nA)_154/finalarr.sav'

stop

END
```

PRO tracking

```
;track the particles in consecutive frames

; 1 pixel = 12.269939 nm

restore, '/Applications/IDL/test(.1nA)_154/finalarr.sav'

;create a trackingarr and strat to track

frames=335

dropletsInst=200

Compared_arr1 = make_array(frames, 2, 4202,/float)

Compared_arr2 = make_array(frames, 2, 4202,/float)

Result_arr = make_array(frames, 1, 4202,/float)

correspondarr=make_array(frames,4202,/float,value=-1)

transferarr=make_array(frames,5,dropletsInst,/float)

;if the particle area is less than 25 pixels, it is defined as being noise, so zeroed and erased
from finalarray

for A=0,(frames - 1) do begin

for P=0,(dropletsInst - 1) do begin

        if finalarr[A,4,P] lt 25 then begin

                finalarr[A,1,P]=0

        endif

endfor

endfor

y=0

for r=0,(dropletsInst - 1) do begin

  existence=where(finalarr[*,1,R] gt 0)
```

```
  if existence[0] ge 0 then begin
    transferarr[*,*,y]=finalarr[*,*,r]
    transferarr[*,0,y]=y
    y++
  endif
endfor
finalarr=0
finalarr=transferarr
save,finalarr,filename='/applications/idl/test(.1nA)_154/finalarr2.sav
Trackingarr = make_array(frames, 5, 4202,/float)
for N=0,(dropletsInst - 1) do begin
  Trackingarr[0,*,N] = finalarr[0,*,N]
  correspondarr[0,N]=N
endfor
numberTracked = n_elements(where(trackingarr[0,1,*] gt 0))
for G=0,(frames - 2),1 do begin
print,G
for M = G, G do begin
 for K = 0L, 4201L, 1L do begin
  Oldmin = 4200
   for L = 0, (dropletsInst - 1) do begin
Newmin = abs(Finalarr[M+1,1,L]-trackingarr[M,1,K]) + abs(Finalarr[M+1,2,L]-
trackingarr[M,2,K]) + abs(Finalarr[M+1,3,L]-trackingarr[M,3,K])
```

```
; if the corresponding newmin smaller then previous one, the particle is identified as the same one
    if Newmin lt Oldmin then begin
     trackingarr[M+1,1,k] = finalarr[M+1,1,L]
      trackingarr[M+1,2,k] = finalarr[M+1,2,L]
     trackingarr[M+1,3,k] = finalarr[M+1,3,L]
    trackingarr[M+1,4,k] = finalarr[M+1,4,L]
    Oldmin = Newmin
    Lfinal=L
   endif
     trackingarr[M+1,0,k] = k
  endfor
    correspondarr[M+1,k]=Lfinal
 endfor
endfor
;if the particle radius increase more than twice, the particle is defined as being merged
   for o = 0L, 4201L, 1L do begin
     deltaR1 = (trackingarr[G+1,3,o]-trackingarr[G,3,o])/trackingarr[G,3,o]
      if trackingarr[G,1,o] NE 0 and trackingarr[G,2,o] NE 0 then begin
       if abs(deltaR1) gt 1 then begin
         trackingarr[G+1,1,o]=0
         trackingarr[G+1,2,o]=0
       endif
```

```
    endif
  endfor
;save the tracking result and compare it with the result after velocity limit criterion
;Compared_arr1 = make_array(frames, 2, dropletsInst,/float)
   for D = 0L, 4201L, 1L do begin
     Compared_arr1(G,0,D) = trackingarr(G,1,D)
      Compared_arr1(G,1,D) = trackingarr(G,2,D)
    endfor
;if the particle velocity is larger than its radius between two consecutive frames and larger
than 228nm/s
  ;this particle is defined as disappeared and its trackingarr[N,3,O] are set as 0
 for B = 0L, 4201L, 1L do begin
   P_velocity = 61.35*((trackingarr[G+1,1,B]-
trackingarr[G,1,B])^2+(trackingarr[G+1,2,B]-trackingarr[G,2,B])^2)^0.5
   if (P_velocity gt (61.35 * trackingarr[G,3,B]) and P_velocity gt 228) then begin
     trackingarr[G,1,B]=0
     trackingarr[G,2,B]=0
   endif
 endfor
;save the tracking result and compare it with the result after particle merged criterion
;Compared_arr2 = make_array(frames, 2, dropletsInst,/float)
;Result_arr = make_array(frames, 1, dropletsInst,/float)
   for F = 0L, 4201L, 1L do begin
```

```
    Compared_arr2(G,0,F) = trackingarr(G,1,F)
     Compared_arr2(G,1,F) = trackingarr(G,2,F)
     Result_arr(G,0,F) = compared_arr1(G,0,F) - compared_arr2(G,0,F)
    endfor
;The particle indices in the frame which is after the frame with xy indices = [0,0] are set
as [0,0,0,0]
  for s=0,4201 do begin
        I=where(trackingarr[*,1,S] ne 0)
        I2=where(trackingarr[*,1,S] ne 0)
        if I[0] eq -1 and I2[0] eq -1 then continue
    if trackingarr[G,1,S] eq 0 or trackingarr[G,2,S] eq 0 then begin
      for H = G, (frames - 2) do begin
       trackingarr[H,1,S]  = 0
       trackingarr[H,2,S]  = 0
       trackingarr[H,3,S]  = 0
       trackingarr[H,4,S]  = 0
          correspondarr[H,S]=-1
      endfor
    endif
  endfor
;add new particles from finalarr
for C=0, (n_elements(where(finalarr[G+1,1,*] gt 0)) - 1) do begin
counted=0
```

```
  for E=0,4201 do begin
   if correspondarr[G+1,E] eq C then counted = 1
  endfor
  if counted ne 1 then begin
         trackingarr[G+1,1,numberTracked]=finalarr[G+1,1,C]
         trackingarr[G+1,2,numberTracked]=finalarr[G+1,2,C]
         trackingarr[G+1,3,numberTracked]=finalarr[G+1,3,C]
         trackingarr[G+1,4,numberTracked]=finalarr[G+1,4,C]
         trackingarr[G+1,0,numberTracked]=numberTracked
         numberTracked++
  endif
endfor
endfor
;if the particle only lasted under 10 seconds it is defined as being noise
for Q=0,4201 do begin
  duration=where(trackingarr[*,1,Q] gt 0)
  duration2=where(trackingarr[*,2,Q] gt 0)
  if duration[0] eq -1 and duration[0] eq -1 then continue
  if n_elements(duration) lt 50 then begin
      trackingarr[*,1,Q]  = 0
      trackingarr[*,2,Q]  = 0
      trackingarr[*,3,Q]  = 0
      trackingarr[*,4,Q]  = 0
```

```
  endif
endfor
;check the particle path
window,3,title='particle path 0'
plot,trackingarr[*,1,0],trackingarr[*,2,0],psym=-6
Window, 2, TITLE='particle path 20'
plot, trackingarr[*,1,20], trackingarr[*,2,20], psym=-6
Window, 3, TITLE='particle path 42'
plot, trackingarr[*,1,42], trackingarr[*,2,42], psym=-6
for zz=0,650 do begin
        print,string(zz) + string(n_elements(where(trackingarr[*,1,zz] gt 0)))
endfor
save,trackingarr,filename='/applications/idl/test(.1nA)_154/trackingarr.sav
stop
END
```

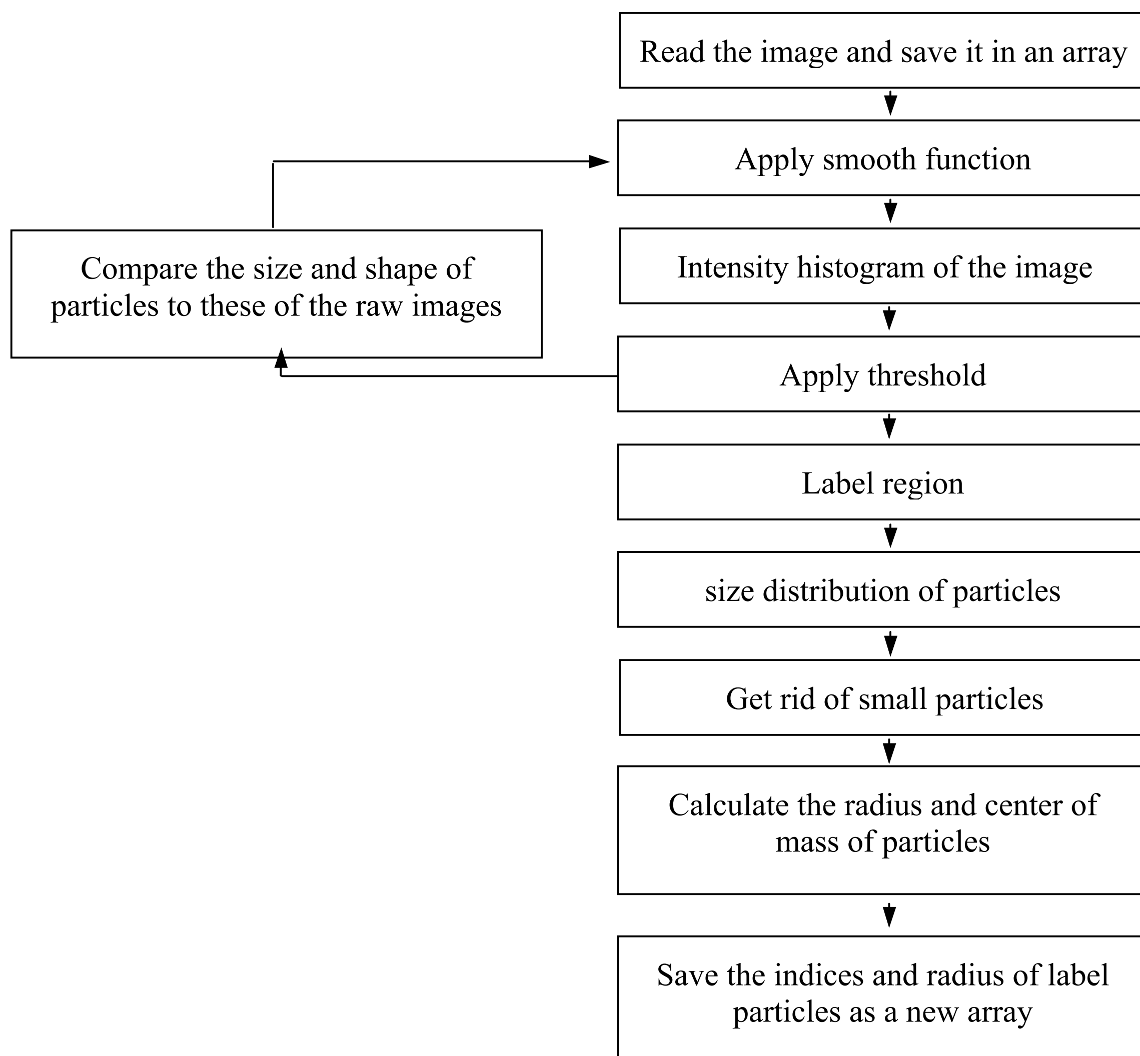

Figure E.1 Flow Chart for "PRO readimage", an IDL code to identify droplets in each image frame.

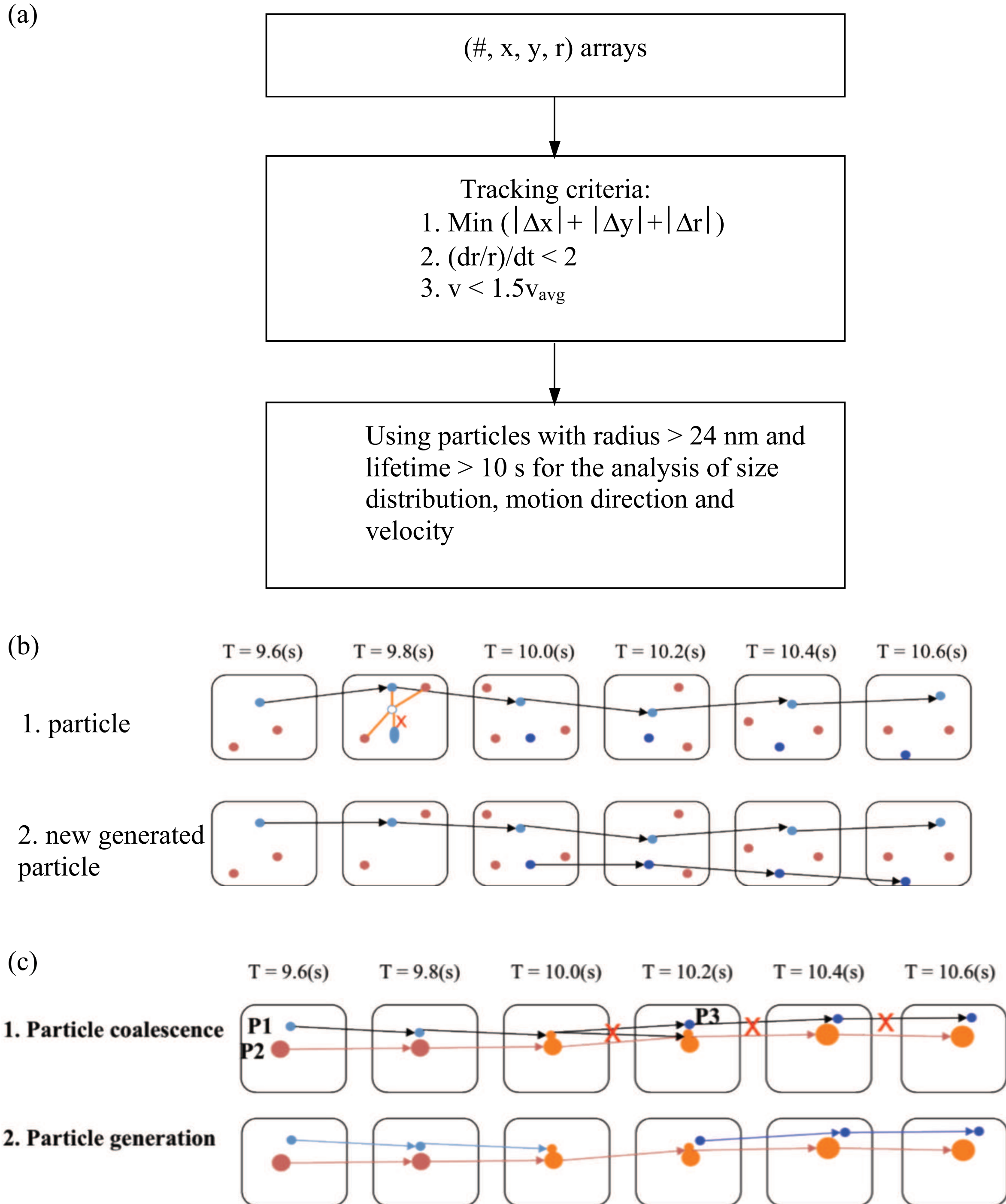

Figure E.2 (a) Flow Chart for "PRO tracking", an IDL code to identify and track droplets between image frames. (b) Illustrations show case of droplet motion and generation. (c) Illustrations show particle coalescence and generation.

APPENDIX F

Droplet Motion: Thermal Gradients

To consider the possible driving force for droplet motion, we measured the contact angles of droplets in motion, and calculate the thermal gradient that would drive droplet motion at a specific velocity, ΔTv. For this purpose, we considered both viscous and mechanical forces. We also calculated the local temperature rise after a one-spot FIB scan, ΔT_{FIB}, and compared it with ΔTv. We suggest that FIB-induced thermal gradient is not sufficient to drive droplet motion.

We consider the influences of FIB-heating induced mechanical forces and the frictional force preventing liquid Ga from sliding past the GaAs surface (the viscous force) to estimate the thermal gradient, ΔT_v, that would be needed to produce droplet motion at the measured speed.[27] We assume that GaAs is crystalline and that γ_{GaAs} and $\gamma_{GaAs\text{-}Ga}$ are temperature-independent, while $\gamma_{Ga}(T)$ is temperature-dependent. Thus, in this calculation, we assume there is ΔTv in between advancing point (A) and receding point (R) of a droplet, leading to the difference of $\gamma_{Ga,}(T = T_R)$ and $\gamma_{Ga,}\ (T = T_A)$. Figure F.1 shows the schematic illustration of a droplet in motion, in which its advancing contact angle, θ_A, is larger than its receding contact angle, θ_R . The viscous force is defined as

$$\int_{-R}^{R} 3\eta \frac{V}{\zeta} dx - \frac{1}{2}(\gamma_{Ga,T_R} - \gamma_{Ga,T_A}) \tag{F.1}$$

The mechanical force is defined as

$$\gamma_{Ga} \cos\theta_R - \gamma_{Ga} \cos\theta_A \tag{F.2}$$

Hence, ΔT is approximated as[28]

$$\Delta T_v = \frac{6R\square JU + \gamma_{Ga}(\cos\theta_R - \cos\theta_A)}{\left|\frac{d\gamma}{dT}\right|(\frac{1}{2} + \cos\theta_R)}, \tag{F.3}$$

The details of equation symbols were listed in the Ch3.5.3.

Using the measured contact angles, θ_A and θ_R, droplet diameters, 2R, and velocities, V, along with literature values for γ_{Ga} and $d\gamma/dT$,[26] ΔT_v was calculated for various Ga droplets formed using 30 kV FIB irradiation at 0.3 nA, as shown in Table F. 1. The calculated ΔT_v ranges from 0.39 to 1.7 °C. These calculated values are slightly larger than ΔT_{FIB}.

Table F. 1 shows the values of θ_A, θ_R, R, V, γ_{Ga}, $d\gamma/dT$, and the calculated thermal gradient, ΔTv. θ_A, θ_R, R, V are from experimental measurement, and γ_{Ga} and $d\gamma/dT$ are from literature.[26]

V (Velocity) (m/s)	$6.19\times10^{-9} - 5.26\times10^{-8}$
∝ viscosity (kg/sm)	2.13×10^{-3}
θ_A (degree)	26.66 – 43.1
θ_R (degree)	32.5 – 52.3
$d\gamma/dT$ ($Kg/s^2\,^oC$)	-0.066
γ_A (Kg/s^2)	0.708
R (m)	$1.25\times10^{-7} - 1.73\times10^{-7}$
J (m^{-1})	1.47×10^{5}
ΔTv (^oC)	0.39–1.7
Thermal gradient ($^oC/m$)	$1.56\times10^{6}–3.81\times10^{6}$

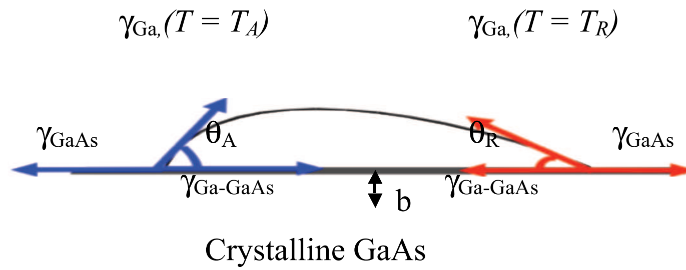

Figure F.1 Geometry corresponding to the steady motion of a Ga droplet on irradiated GaAs surfaces. θ is the contact angle and γ is the surface interface energy. The subscripts A and R denote the advancing and receding edges of the droplet, respectively, and b is the Navier slip length

References

[1]R. Behrisch, P. Sigmund, M. T. Robinson, H. H. Andersen, H. L. Bay, and H. E. Roosendaal, *Sputtering by Particle Bombardment I*, Vol. 47 (Springer-Verlag, New York, 1981).

[2]R. Behrisch, W. Heiland, W. Poschenrieder, P. Staib, and H. Verbeek, *Ion Surface Interaction, Sputtering and Related Phenomena* (Gordon and Breach Science New York, 1973).

[3]Y. Stark, R. Fromter, D. Stickler, and H. P. Oepen, J. Appl. Phys. **105,** 5 (2009).

[4]A. A. Tseng, Small **1,** 594 (2005).

[5]A. A. Tseng, J. Micromech. Microeng. **14,** R15 (2004).

[6]L. R. Harriott, J. Vac. Sci. Technol. A **8,** 899 (1990).

[7]T. Ishitani and H. Kaga, J. Electron Microsc. **44,** 331 (1995).

[8]Y. I. Nissim, A. Lietoila, R. B. Gold, and J. F. Gibbons, J. Appl. Phys. **51,** 274 (1980).

[9]Constantinos Christofides and G. Ghibaudo, *Effect of Disorder and Defects in Ion-Implanted Semiconductros: Optical and Photothermal Characterization*, Vol. 46 (Academic Press, San Diego, 1997).

[10]K. Nozawa, M. H. Delville, H. Ushiki, P. Panizza, and J. P. Delville, Phys. Rev. E **72** (2005).

[11]M. Zinkeallmang, L. C. Feldman, and M. H. Grabow, Surf. Sci. Rep. **16,** 377 (1992).

[12]M. Zinkeallmang, L. C. Feldman, and S. Nakahara, Appl. Phys. Lett. **51,** 975 (1987).

[13]G. Rizza, Y. Ramjauny, T. Gacoin, and L. Vieille, Phys. Rev. B **76,** 245414 (2007).

[14]D. A. Porter and K. E. Easterling, *Phase Transformations in Metals and Alloys*, 2nd ed. (Nelson Thornes, Cheltenham, UK, 2001).

[15]L. Ratke and P. W. Voorhees, *Growth and Coarsening* (Springer, New York, 2002).
[16]J. A. Marqusee and J. Ross, J. Chem. Phys. **79,** 373 (1983).

[17]S. B. Heinig KH, Markwitz A, Grotzschel R, Strobel M, Oswald S, Nucl. Instrum. Methods Phys. Res. B **147,** 343 (1999).

[18]I. Leubner, R. Jagannathan, and J. Wey, Photogr. Sci. Eng. **24,** 268 (1980).

[19]G. Rizza, H. Cheverry, T. Gacoin, A. Lamasson, and S. Henry, J. Appl. Phys. **101** (2007).

[20]G. Rizza, A. Dunlop, and A. Dezellus, Nucl. Instrum. Methods Phys. Res. B **256,** 219 (2007).

[21]G. Rizza, Y. Ramjauny, T. Gacoin, and S. Henry, Nucl. Instrum. Meth. Phys. Res. B **257,** 15 (2007).

[22]J. F. Ziegler, J. P. Biersack, and U. Littmark, *The Stopping and Range of Ions in Matter.* (Pergamon Press, New York, 1985).

[23]CORE, Profile Code.

[24]F. P. Ludwig and J. Schmelzer, J. Res. Phys. Chem. Chem. Phys. **192,** 155 (1995).

[25]E. Brosh and A. Kiv, J. Nucl. Mater. **306,** 173 (2002).

[26]M. L. Ford and A. Nadim, Phys. Fluids **6,** 3183 (1994).